COUPLED RADIATION-GASDYNAMIC SOLUTION METHOD FOR HYPERSONIC SHOCK LAYERS IN THERMOCHEMICAL NONEQUILIBRIUM

DISSERTATION

Christopher L. Martin, Jr., Captain, USAF

AFIT/DS/ENY/11-16

DEPARTMENT OF THE AIR FORCE
AIR UNIVERSITY

AIR FORCE INSTITUTE OF TECHNOLOGY

Wright-Patterson Air Force Base, Ohio

AFIT/DS/ENY/11-16

COUPLED RADIATION-GASDYNAMIC SOLUTION METHOD FOR HYPERSONIC SHOCK LAYERS IN THERMOCHEMICAL NONEQUILIBRIUM

DISSERTATION

Presented to the Faculty

Department of Aeronautics and Astronautics

Graduate School of Engineering and Management

Air Force Institute of Technology

Air University

Air Education and Training Command

In Partial Fulfillment of the Requirements for the

Degree of Doctor of Philosophy

Christopher L. Martin, Jr., BSE, MSME

Captain, USAF

December 2011

AFIT/DS/ENY/11-16

COUPLED RADIATION-GASDYNAMIC SOLUTION METHOD FOR HYPERSONIC SHOCK LAYERS IN THERMOCHEMICAL NONEQUILIBRIUM

Christopher L. Martin, Jr., BSE, MSME
Captain, USAF

Approved:

Robert B. Greendyke, PhD (Chairman)	Date
William F. Bailey, PhD (Member)	Date
Mark F. Reeder, PhD (Member)	Date
Maj. Andrew J. Lofthouse, PhD (Member)	Date

Accepted:

M. U. THOMAS Dean, Graduate School of Engineering and Management	Date

Abstract

The purpose of this research was to develop a highly accurate computational method for calculating the nonequilibrium radiative heat transfer within reentry shock layers. The nonequilibrium state of the flowfield was obtained by using the multispecies multitemperature nonequilibrium flow solver NH7AIR which is capable of separately tracking the vibrational energy of each diatomic species and the energy of the free and bound electrons. The calculation of radiative heat transfer was performed by utilizing the detailed line-by-line spectral radiation solver SPRADIAN. Two radiative transport schemes were implemented in this coupled code. The first scheme was based on a straightforward application of the standard tangent slab solution method. The second scheme was based on the conservation of radiative energy and resulted in a finite volume method for radiative heat transfer (FVMR). Data from the FIRE II flight experiment were used to validate the coupled radiation-gasdynamic solver. Coupled results exhibited a high degree of agreement with experimental data. The utility of the FVMR scheme was also examined in an uncoupled implementation and shows promise for future implementation in a coupled setting. Together, the enhancement of the nonequilibrium thermal modeling, the use of a highly accurate spectral radiation solver and the development of a conservative scheme for radiative transport constitute a significant improvement in current capabilities available for modeling the radiating nonequilibrium shock layers which accompany reentry flight.

Dedication

To those who have laid down their lives for our nation:
May their sacrifice constrain us to a reverent humility and an unbroken diligence in this our duty—to well and faithfully defend our cherished homeland, her ideals and her free people.

Acknowledgments

This work was supported by the Air Force Office of Scientific Research. The student would like to thank Dr. John Schmisseur (AFOSR/RSA), for this financial support and for the opportunity to work under the Hypersonics and Transition portfolio. Additionally, the student wishes to express his sincere thanks to Dr. Takumi Abe for enabling this work by providing the student with his excellent SPRADIAN computer code. Many thanks are also given to Dr. Michael White (AFRL/RBAC) for his assistance in familiarizing the student with the nonequilibrium flow solver and for fielding his sundry inquiries regarding the same. The student also extends a hearty _thank you' to Mr. David Doak (AFIT/SCOO) for his excellent hardware and network support. Finally, the student would be greatly remiss in failing to acknowledge his deep debt of gratitude to his research advisor, Dr. Robert Greendyke, and committee members, Dr. Bill Bailey, Dr. Mark Reeder and Maj. Andrew Lofthouse, for their guidance and encouragement through the long, difficult and humbling task of producing this dissertation.

Table of Contents

Page

List of Figures

Page

List of Tables

Page

Nomenclature

Variables

a	local speed of sound
A_{ul}	Einstein A coefficient, emission
$\mathbf{A}$	constant Jacobian matrix
a_i	acceleration component
A_k	area of k-th face
B_{lu}	Einstein B coefficient, absorption
c	speed of light
c_i , c_j	random velocity component
$C_{v,s}$	constant volume specific heat, species s
D_a	ambipolar diffusion coefficient
D_s	diffusion coefficient
D_+	difference operator
D_e	quantum well depth for given electronic state
D_s	dissociation energy, species s
e	elementary charge
E^*	equilibrium energy
E_e	total energy of free electrons
$e_{el,s}$	electronic energy, species s

E^i	electric field component
$\tilde{\mathbf{e}}_k$	eigenvector of local linearization problem
E_v	vibrational energy
$e_{v,s}$	vibrational energy, species s
$e^{**}_{v,s}$	vibrational energy at electron temperature.
e_s	internal energy of species s
e^0_s	heat of formation, species s
$\mathbf{F}$	flux vector of conserved quantities
F	velocity distribution function
f_a	line oscillator strength
$\hat{F}$	x-direction flux vector
$F^i_{m,s}$	momentum equation force term component
$\hat{F}_v$	x-direction viscous flux vector
$g_{n,s}$	degeneracy of n-th energy level, species *s*
g	relative velocity of collision
$\hat{G}$	y-direction flux vector
$G(v)$	vibrational energy for the given electronic state
G_p	incident radiation at point p
$\hat{G}_v$	y-direction viscous flux vector
h	Plank‘s constant

h	enthalpy
h_s^0	heat of formation, species s
I	ionization potential
I	radiative intensity
J	Jacobian of transformation
J	rotational quantum number
k	Boltzmann‘s constant
$K_{c,r}$	equilibrium constant
$k_{f,r}, k_{b,r}$	forward and backward rate constants
$K(i,j)$	transition rate coefficient
L	characteristic length
$\mathcal{M}_s$	molecular mass
m	mass; molecular mass
$\hat{N}$	Avogadro‘s number
n	principle quantum number
$\dot{N}_{s_{s,r}}$	production of species *s* by reaction *r*
N_s	number density of species s
$\hat{n}_k$	unit normal vector of k-th face
n_x, n_y	normal vector components
p	total pressure
p_s	partial pressure due to species s

$P_{ele,s}$	Joule heating source term
q_s^j	heat flux component due to species s
Q	vector of conserved variables
$Q_{m,s}$	energy equation source terms
Q_{m-V}	vibrational energy equation source terms
$\dot{Q}_{rad}$	radiative source term
$q_{v'v''}$	Franck-Condon factor
R	gas constant
r_e	equilibrium bond distance
$R_e(r)$	electron dipole moment
$\left\|R_{v'v''}\right\|^2$	electronic transition strength
S	shock speed
$\vec{s}_i$	solid angle vector of i-th direction
$\hat{s}$	unit normal vector of ray
$S_{J'J''}$	Honl-London factor
T	heavy particle temperature
T_a	effective temperature
T_e	electron temperature
T_v	vibrational temperature
u^j	total velocity component

u_i, u_j	average bulk velocity component
$U_{\nu p}$	Planck radiation density distribution
u_s^j	species velocity component
$U(r)$	potential energy function
v	vibrational quantum number
V_s^j	diffusion velocity component
$\mathbf{w}$	vector of conserved variables
W	vector of source terms
W	general molecular quantity
$\mathbf{w}$	acceleration vector
W	source terms vector
z	wall normal direction
Z_s	charge of species s

Greek Symbols

α_k	strength of k-th wave
$[\mathrm{X}_s]$	molar concentration of species s
χ	deflection angle
χ	nondimensional number density
$\tilde{\Delta}$	slope of linear interpolants
δ	entropy fix parameter
$\Delta\lambda_w$	full width at half maximum

ε	emission coefficient
ε	impact azimuth
η	generalized body-normal coordinate direction
γ	ratio speed of sound
Γ_s	flux quantity in diffusion processes
κ'	absorption coefficient
κ	thermal conductivity
λ_k	speed of k-th wave
λ	mean free path
λ	wavelength
$\tilde{\lambda}$	numerical viscosity
η	viscosity
ν	frequency
$\nu'_{s,r}, \nu''_{s,r}$	stoichiometric coefficients
ν^*_{er}	effective collision frequency of electrons with *r* particles
$\dot{\omega}_s$	species production term
Φ_λ	Voigt line profile
φ	azimuth
Ψ_e	electronic wave function
Ψ_v	vibrational wave function
ρ_s	density of species *s*

ρ_i	nondimensional number density for state i
σ	collision cross section
τ_s^{ij}	stress tensor of species *s*
$\tau_{s,k}$	relaxation time, species s in bath of k particles
θ	inclination
$\theta_{el,s}$	characteristic electron temperature, species s
$\theta_{v,s}$	characteristic vibrational temperature, species s
ζ	generalized body-tangent coordinate direction

Subscripts, Superscripts and Indices

0	value at line center
a	adjacent cell
bb	bound-bound
bf	bound-free
c	continuum
e', *e*"	upper and lower energy levels
ff	free-free
g	ghost cell
i	value associated with i-th direction
i, *j*	vector/tensor indices
i, *j*	upper and lower energy levels

k	value associated with k-th face
L, R	left and right hand sides of cell interface
n	time step
ν	frequency
p	value associated with p-th cell center
r	reaction
s	species
u, l	upper and lower energy levels
$\tilde{W}$	Roe-averaged value
z	degree of ionization

Preface

Perseverance is more prevailing than violence; and many things which cannot be overcome when they are together, yield themselves up when taken little by little.

-Plutarch, Parallel Lives, Sertorius, 1st c.

Analysis—definition: noun. 1. a detailed examination of the elements or structure of something, 2. the separation of something into its constituent elements

-Oxford English Dictionary, 3rd ed., revised, 2008

Plutarch's observation regarding the career of the Roman general Quintus Sertorius holds fairly well by analogy to the task of analysis set before the student—and perhaps even especially so for anyone conducting research within the field of hypersonics. The implications of hypersonic flight for mankind are indeed exciting, and many large, national programs have been enthusiastically advanced in pursuit of this lofty goal. However, many of them have failed to persevere under various technological, institutional, fiscal and political constraints; that this is evident may be seen from the fits-and-starts history of hypersonics to date. The great challenge is that hypersonic flows are intrinsically multiphysical in nature and encompasses numerous physical phenomena issuing from many distinct fields of inquiry: gasdynamics, gaskinetic theory, thermodynamics, turbulence, material science, chemistry, radiative transport, quantum mechanics, *et cetera*. Thus, those who would master the theoretical and technological challenges of the field must, like the Roman generals who shrewdly expanded upon the earth a vast and disparate empire, carefully examine in detail these varied phenomena with an eye to their characteristics individually, as well as their characteristics in interaction with one another. Such is the nature of even modest applications of theoretical knowledge to the design and analysis of real-world hypersonic flight technologies.

COUPLED RADIATION-GASDYNAMIC SOLUTION METHOD FOR HYPERSONIC SHOCK LAYERS IN THERMOCHEMICAL NONEQUILIBRIUM

I. Introduction

At the time of this writing, the fact that national interest in hypersonics is alive and well—or at least making one of its periodic comebacks—is evident by the hundred-million-dollar expenditures which the DoD has made in this past decade to reinvigorate our national competency in hypersonics (OSD, 2008). Recent comments from Dr. Dahm, former Chief Scientist of the Air Force, are a further indication of this upward swing in interest. Dr. Dahm has been a potent advocate for hypersonics within the DoD and has labored to aid decision makers in understanding the contemporary implications of hypersonic systems, noting that "…this wouldn't just do what we do today faster. We could do things differently" (Barnes, 2010). In other words, the fielding of operational hypersonics systems by the United States or a competitor nation would constitute a disruptive paradigm shift (Borger, 2007), substantially affecting the way in which wars are prosecuted and the homeland defended. However, Dr. Dahm and other proponents of the military utility of such hypersonic systems must wait patiently, if not a bit anxiously, for the completion of the requisite basic research and technology development. Perhaps this anxiety is understandable, since the corporate memory of the hypersonics community is haunted by the ghosts of many canceled programs which either failed to perform according to stakeholder expectations or which were otherwise deemed too risky to

pursue (Heppenheimer, 2007; Hallion 2005; Anderson, 1984). Yet, despite towering technical challenges and many perceived setbacks, the Air Force has throughout its history maintained some vision for the utilization of hypersonic flight vehicles, although reformulated in various ways according to the perceived needs of the day. In recent years, these needs have come to be redefined within the purview of the Operationally Responsive Space and Global Strike/Global Persistent Attack CONOPS, for which some sort of reusable, air-breathing or rocket-launched platform is typically envisioned (Fuchs, *et al*., 2000; Tichkoff, *et al.*, 1998; McCall, *et al*., 1995; McLucas, *et al.*, 1989).

Whatever vehicle concept is chosen to enable these CONOPS, the basic design and analysis tasks in the development of a hypersonic system remain fundamentally unchanged. This fact is quite evident from even a cursory reading of Heppenheimer's Facing the Heat Barrier: a History of Hypersonics. Whether discussing X-15, Dyna-Soar, Apollo, NASP, or X-51, the same technical problem areas are addressed again and again, namely: propulsion, materials, structures, transition/turbulence, control, and, finally, thermal management.

The scope of the accomplished research is first within the bounds of the latter problem area. As Heppenheimer's selected title indicates, one of the most significant physical barriers of the hypersonic flight envelope is imposed by the tremendous heat loads experienced in flight. Every undergraduate engineering student is taught that heat transfer occurs due to three basic mechanisms: convection, conduction and radiation. In most flight regimes, the aerodynamicist can simply concentrate on convection and conduction, completely ignoring the contributions from radiation. For flows around reentry vehicles, this approach is no longer valid. In order to perform analyses of the

radiating shock layers, it is absolutely essential to account for the contributions of air chemistry and radiation effects to the overall heat transfer problem. Additionally, severe thermal and chemical nonequilibrium are known to occur at the high Mach numbers characteristic of reentry conditions, therefore it is necessary to account for these relaxation processes as well.

Finally, it is noted that radiation is transmitted both towards and away from a body reentering the atmosphere. The radiation transmitted toward the body is of interest to the design engineer who is concerned with the heat transfer problem described above. However, the radiation transmitted away from the body is of interest not only to engineers and researchers but to MASINT personnel also. It is conceivable that a competitor state with an adequate technological and industrial base could in the near future pursue stealthy hypersonic weapon systems as a deterrent to future US systems of like construction. Given the speeds involved in a hypersonic strike, the time to detect an enemy‘s hypersonic weapon system will be perhaps *the* critical link in the kill chain for US countermeasures. Therefore, it is relevant to the national security of the US to be able to detect these stealthy vehicles. Fortunately, while it may be possible to reduce the radar cross-section of a vehicle or even to mask propulsion signatures, it is impossible to conceal the radiation which is emitted by the highly energetic gas in the shock layers surrounding vehicles moving at high Mach numbers. The degree to which one can correctly model these phenomena will have a direct bearing upon the ability of future MASINT personnel to correctly identify hostile vehicles *en route* to attack the US, its interests and its deployed forces. It is in light of these considerations especially that the method which is developed in the following chapters is proposed.

II. Background

Computational models have been used extensively in the field of hypersonics since the 1950s and 1960s. Many of these early calculations based on curve-fitted experimental data, while others were more closely related to first principles. In either case, it's rather impressive that these models provided reasonable enough estimates to design the reentry vehicles of the early manned space programs (Berman, 1983). From this starting point, the evolution of these numerical models has naturally followed the evolution of the digital computer. The 1980s saw many impressive calculations from first principles for geometrically simplified flowfields. The developments of the last two decades have brought about epochal improvement in computational capabilities, and so the application of theory to computational models has continued to advance. These advancements have basically followed some combination of these trends: 1) higher dimensional flow fields, 2) more accurate physical models and 3) coupling of physical phenomena (i.e., flowfield, ablation, radiation, material response, *etc.*).

Today, it is possible, although rare, to see research codes capable of calculating nonequilibrium flowfields coupled with radiation and ablation (Johnston, 2006, 2008; Feldick, *et al.*, 2008). However, even today the computational cost of implementing the most general theories in an aerothermodynamic code is prohibitive and various trade-offs are made. The most expensive aspect of a fully-coupled radiation flowfield methodology is the calculation of the spectral data and radiative transport. This expense is due to the influence of a single additional independent variable, wavelength. Radiative transport in a participating or grey medium, such as a high temperature gas, depends on the spectral properties of the transport medium such as emission, absorption and scattering. (Modest,

2003; Zel'dovich and Raizer, 2003) —Band models" are the simplest approach to modeling this part of this dependency. These models are based upon the assumption of equilibrium state populations according to a single equilibrium heavy-particle temperature. Thus, radiative phenomena for a given species are lumped into a band, wherein the magnitude of the radiative flux is a direct empirical result of this temperature and the species number density. These methods have the advantage, in coupled flowfield solutions of being computationally inexpensive. However, because of the chemical and thermal equilibrium assumptions inherent in these methods, they are not always applicable in hypersonic flows where these assumptions are violated. (Olstad, 1971; Zoby, 1993) There have been some limited attempts to adjust banded models for nonequilibrium effects (Greendyke and Hartung, 1991; 1994), but in many cases, radiative phenomena are too complex to accommodate the banded models to nonequilibrium environments.

The radiation observed within a high-temperature gas exhibits a complex structure in terms of its spectral characteristics. This structure ranges from the very coarse, which spans hundreds or thousands of nanometers, such as molecular bands, to the very fine, those spanning a few nanometers or less, such as line emission and absorption. Under equilibrium conditions, the band models above account fairly well for many of these coarse structures. However, the fine structures are entirely missed. This lack of detail is actually a rather significant shortcoming since the finer structures account for the bulk of the radiation emission and absorption (Herzberg, 1950). The hybrid model of Nicolet (1969, 1970) called RAD/EQUIL represented an improvement to the typical band model.

This hybrid model consists of a mixture of banded models for continuum equilibrium radiative processes, and detailed spectral analysis for certain selected line emissions.

The most advanced code for the calculation of radiative transport is the NEQAIR code originally developed by Whiting, *et al.*, (1969) as a spectrographic code. The code was later adapted for thermochemical nonequilibrium effects by Park (1985) for use in hypersonic flowfields. With this upgraded capability NEQAIR, is now capable of calculating the population of upper molecular and atomic states based upon the heavy particle, rotational, vibrational, and electron temperatures. Following from the determination of the state populations, the code then performs a line-by-line integration through the user-defined spectral region under consideration for the determination of local radiative emission and absorption. NEQAIR, while highly accurate, has a higher computational cost associated, relative to the band and hybrid models. Johnston's HARA code is another notable nonequilibrium radiation code gaining popularity in the literature for its use of some of the most recent rate data available (Johnston 2006, 2008; Feldick, *et al*., 2008). The code to be used in this research effort, SPRADIAN, is a variant of NEQAIR and was developed by researchers Fujita and Abe at JAXA (1997). It has been chosen because of the highly detailed line-by-line method it uses to calculate emission and absorption coefficients and the ease with which it may be modified to accommodate the multitemperature thermal model herein discussed.

Despite the existence of such a detailed method as SPRADIAN, the accuracy of the radiative solution will only be as high as is allowed by the accuracy of the solution for the thermodynamic state of the flowfield. Furthermore, for any investigation concerned with the radiation resulting from reentry conditions, it is necessary to account for the

nonequilibrium of the thermodynamic state. This characterization of the nonequilibrium may be accomplished at varying levels of approximation. Those models which involve the least approximation directly simulate the state-to-state transitions among the internal energy levels of the flow species (Magin, *et al.*, 2008; Josyula 2000; Park, 1992).

While potentially very accurate, this class of models presents a set of calculations that are far more expensive to perform than some other useful approximations. The distribution of energy within the internal energy manifolds may also be approximated by partitioning the internal energy modes and assuming equilibrium within or among them, according to the nature of the relaxation processes involved. When the internal energy modes are thus partitioned, the nonequilibrium state is adequately specified with knowledge of the species number densities, N_i, and the temperatures which are characteristic of the thermal nonequilibrium, T, $T_{rot,i}$, $T_{vib,i}$ and T_e. The methods of this class which are proposed in the literature basically differ according to the assumptions made regarding the nature of the relaxation processes. For instance, the popular two-temperature model of Park (1985, 1992) posits that the thermodynamic nonequilibrium may be adequately characterized by utilizing a common temperature heavy particle temperature for T and $T_{rot,\ i}$ based on a heavy particle energy equation and a common electronic-vibrational temperature T_{ev} based on an electron-electronic energy equation. It has been proposed that the nonequilibrium may be modeled with improved accuracy by relaxing the second assumption made under the two-temperature model (Josyula and Bailey, 2003). By relaxing this assumption, the vibrational temperature is allowed to vary by species and is no longer artificially constrained by the electron temperature.

Thus, this so-called multispecies multitemperature model allows the internal energy to be redistributed in a more realistic fashion.

In spite of the potential benefit of using the multitemperature model in a coupled flow field-radiation solution method, the two-temperature model pervades the literature as the *de facto* standard method. Prior to this research activity, virtually no work has been performed investigating the effect of exchanging the two-temperature model of thermal nonequilibrium for the multitemperature model in a coupled flow field-radiation computer code with a line-by-line specification of the radiation transport solution. As stated previously, this highly-accurate implementation of the coupled flowfield and radiation solutions is important to the current methodology. With the high degree of accuracy comes severe computational cost. This trade-off between accuracy and the efficiency computation of solutions is accepted up front.

The primary objective of this research effort is to accomplish a loosely-coupled implementation of a detailed radiation solver, such as SPRADIAN, within a suitable nonequilibrium flowfield solver. Prior to the early 1990s, many efforts to accomplish this type of coupling have been attempted on a simplified level and have maintained the equilibrium assumptions. A very notable exception to this history has been the LORAN code of Hartung (Hartung 1991, Chambers 1994), which implemented Nicolet‘s RAD/EQUIL code—utilizing Park‘s nonequilibrium state population calculation—within the LAURA code (Gnoffo 1990, Cheatwood 1996). LAURA is a finite volume based method for nonequilibrium hypersonic flows in chemical and thermal nonequilibrium using finite rate chemical reactions and Park‘s two-temperature model for thermal nonequilibrium (Park, 1987). Another notable exception would be the development of

HARA and its coupled implementation in a viscous shock layer code, again utilizing Park's nonequilibrium model (Johnston, 2006). The goal of both the LORAN code and the Johnston viscous shock layer code was to provide relatively fast coupled solution methods for engineering design and analysis of hypersonic vehicles. To date, these codes represent the "state-of-the-art" for coupled radiation flowfield solution methods. A more detailed method would involve the use of a thermal model which accounts for the conservation of vibrational energy on a species-by-species basis, such as the method implemented by Josyula & Bailey (2006). This computer code, hereafter referred to as NH7AIR, has already been utilized to accomplish simplified uncoupled radiative flowfield calculations—both along the stagnation line and for the whole flowfield (Komives, 2009 a. and b.; Martin 2010).

There exists only one detailed radiation analysis code in practical use today – the NEQAIR (SPRADIAN) code—and it has never been used in a coupled fashion with any flowfield solution method. There have been several attempts at coupling other radiative solution methods to flowfield codes, and even some attempts to look at the effects of both radiation and ablation in flowfields (Nicolet 1970, Sutton 1973), but never with such a detailed line-by-line method as SPRADIAN. Also, these research efforts utilized relatively simple approximations of the nonequilibrium flow field conditions. The method detailed in this dissertation advances the state-of-the-art with both the detailed radiation solution enabled by SPRADIAN and the enhanced nonequilibrium flow field solution provided by NH7AIR.

This work reported in this dissertation was conducted according to the following research objectives. These research objectives are intended to be overarching, with specific supporting details deferred to Chapters III, IV and V.

> Research Objective 1: Develop a computer code suitable for the loosely-coupled calculation of nonequilibrium radiative heat transfer within reentry body shock layers. The calculation of emission and absorption coefficients shall be performed by a highly accurate, line-by-line method. The nonequilibrium state of the flowfield shall be solved by *via* a multitemperature nonequilibrium flow solver capable of separately tracking the vibrational energy of each diatomic species and the energy of the free electrons.
>
> Research Objective 2: Implement two radiative transport schemes. The first shall utilize the tangent slab assumption. The second shall be based on the conservation of radiative energy; namely, it shall be a finite volume method scheme.
>
> Research Objective 3: Validate the developed computer code against the benchmark FIRE II flight experiment (Lewis and Scallion, 1966; Cornette, 1966; Cauchon, 1972).

Chapters III and IV provide a summary of the theory and methodology, respectively, which attend the present research activity. Given the complexity of the problem investigated, a generous amount of space has been devoted to a discussion of the theory and computational methodology. Specific details regarding the computer implementation of the above theory and methodology follow in Chapter V. Results are presented in Chapter VI, and the conclusions drawn from the performed research are reported in Chapter VII.

III. Theory

The focus of this dissertation is the development and validation of a computational method suitable for calculating, in a detailed manner, the flow field-radiation solution of typical shock layers in thermochemical nonequilibrium about reentry vehicles of interest. In this chapter the basic theory associated with the development of such a method is outlined. The theory is presented under two broad headings concerning those aspects of the research activity which pertain to the flow field and radiative solutions, respectively.

Characterizing the Hypersonic Environment

In the strictest sense, the demarcation between subsonic and supersonic refers to that condition wherein the local free stream velocity exceeds the local speed of sound—that is to say, $M > 1$. Unlike the easy distinction made between subsonic and supersonic, distinguishing between supersonic and hypersonic flows in terms of a Mach number is somewhat arbitrary. This observation should not be terribly surprising since—ignoring other effects for a moment—there are no sudden qualitative changes in the behavior of the flow relative to the propagation of acoustical information within the domain, as there are when a flow reaches the speed of sound. Despite the inherent limitation of such a description, as a general rule of thumb, this change is said to occur in air somewhere around Mach 5 (Anderson, 2006). Yet, it is perhaps more instructive to say that the hypersonic regime is one characterized by certain flow features and physical phenomena which become increasingly influential upon flow behavior, with increasing Mach number, and that this influence is first appreciable around Mach 5.

Anderson (2006) and Bertin (1994) proceed from this observation to delineate some of these characteristic features and phenomena. The first and most basic such feature is that of the shock layer. As Mach number increases, the shockwave moves in closer to the body, and the air between the shockwave and the body is thus confined to an increasingly smaller region. This thin region near the body is called the shock layer. It is convenient to discuss the other characteristics as they become of significance in terms of increasing velocity and altitude. With increasing velocity, the bow shock becomes incredibly strong and the kinetic energy of the free steam is increasingly transferred to the internal energy modes of the gas particles. This energy transfer leads to vibrational excitation and ultimately chemical reactions—the dissociation of molecular oxygen and nitrogen and eventually the ionization of the constituent flow species. Also, nonequilibrium chemical and thermal conditions become significant due to the slow characteristic time scales of these relaxation processes relative to the time scales of the flow. The character of the flow also changes with increasing altitude. At altitudes which are sufficiently low, the mean free path of the flow is small enough relative to the characteristic length scales of the flow that the continuum approximation may be assumed. As altitude is increased, interesting features begin to arise. First the entropy layer increases in height and begins to engulf the boundary layer, thus introducing a troublesome vorticity interaction *via* Crocco‘s theorem. Also, the boundary layer and shock layer begin to merge, and the shock layer thickens. As altitude increases still further, so does mean free path, and transition begins to the free molecular regime, where thermal and velocity slip become important effects near the wall. Furthermore, the

continuum assumption begins to deteriorate, and it becomes necessary to transition to an appropriate particle description of the system.

The Knudsen number, $Kn = \lambda / L$, is the ratio of the mean free path to the characteristic flow length and is a parameter used primarily to distinguish continuum flow conditions from non-continuum flow conditions. As such, it provides a convenient rule of thumb regarding applicability of continuum formulations to a set of flow conditions. For $Kn < 0.1$, the flow is said to be in a continuum regime, while for $Kn >> 1.0$, the flow is said to be in the free molecular regime. For continuum calculations, the flow situation may be calculated from the Navier-Stokes equations. The non-continuum conditions require using an appropriate kinetic or particle-based, description (Evans and Harlow, 1957; Bird, 1994). While it has been a common practice to utilize one method or another in the course of a particular investigation, it has been observed that a certain hybrid flows may exhibit regions of transition between continuum and non-continuum conditions. So-called hybrid solvers have been proposed and extensively developed to provide a method of treating these flow situations (Kolobov, *et al.*, 2006). For the investigated trajectory points of the FIRE II experiment, the Knudsen number is around 0.001 and thus the continuum, or fluid, description is applicable.

Governing Fluid Equations

Given the applicability of the continuum assumptions to the present investigation, it is possible to utilize a suitable Navier-Stokes solver. The Navier-Stokes equations in their canonical form do not address chemical or thermal nonequilibrium or any of the relaxation mechanisms associated with these conditions. Therefore, in order to accommodate this formalism to the study of high-temperature gas flows, in which these

features are important, several further _improvements' must be made by incorporating additional source terms to model these sources of nonequilibrium . These improvements upon the basic governing equations have been well developed by others and are presented below in the subsections which follow (Park, 1992; Lee, 1986; Appleton and Bray, 1964; Holt, 1965).

Conservation of Species Mass.

In a reacting multispecies flow it is necessary to account for the effects of both species diffusion and species production and destruction (Josyula and Bailey, 2003).

$$\frac{\partial}{\partial t}\rho_s + \frac{\partial}{\partial x^j}\left(\rho_s u^j\right) = \frac{\partial}{\partial x^j}\left(\rho_s V_s^j\right) + \dot{\omega}_s \tag{1}$$

The first term on the right hand side represents the divergence of the species mass flux vector, as illustrated by the definition of the diffusion velocity.

$$V_s^j = u_s^j - u^j \tag{2}$$

And the second term on the right hand side is the species production term. For continuity, it is required that each of the two new terms equal zero when summed over all the constituent species.

$$\sum_s \dot{\omega}_s = 0 \tag{3}$$

$$\sum_s \rho_s V_s^j = 0 \tag{4}$$

It is also noted that the mixture density is obtained from

$$\rho = \sum_s \rho_s = \sum_s N_s m_s \ . \tag{5}$$

The production term $\dot{\omega}_s$ accounts for the contributions to species *s* by chemical sources and sinks in the flow such as dissociation, ionization, recombination and attachment.

These processes are modeled *via* the use of the rate equation (Vincenti and Kruger, 1967). Consider a gas mixture of species *s* undergoing *r* elementary chemical reactions

$$\sum_{s=1}^{l} \nu'_{s,r} \mathrm{X}_s \underset{k_{b,r}}{\overset{k_{f,r}}{\rightleftharpoons}} \sum_{s=1}^{l} \nu''_{s,r} \mathrm{X}_s \tag{6}$$

where $\nu'_{s,r}$ and $\nu''_{s,r}$ are the stoichiometric coefficients of the reaction and $k_{f,r}$ and $k_{b,r}$ are the forward and backward rate constants. Whereby, the contribution of reaction *r* to the rate of change of the concentration of species *s* is given by

$$\left(\frac{d[\mathrm{X}_s]}{dt}\right)_r = \left(\nu''_{s,r} - \nu'_{s,r}\right) k_{f,r} \prod_{s=1}^{l} [\mathrm{X}_s]^{\nu'_{s,r}} + \left(\nu'_{s,r} - \nu''_{s,r}\right) k_{b,r} \prod_{s=1}^{l} [\mathrm{X}_s]^{\nu''_{s,r}} \tag{10}$$

In this way, the total rate of change of the molar concentration of species s $[\mathrm{X}_s]$ is given by summing over all contributing reactions *r*.

$$\frac{d[\mathrm{X}_s]}{dt} = \sum_{r=1}^{y} \left(\nu''_{s,r} - \nu'_{s,r}\right) \left\{ k_{f,r} \prod_{s=1}^{l} [\mathrm{X}_s]^{\nu'_{s,r}} - k_{b,r} \prod_{s=1}^{l} [\mathrm{X}_s]^{\nu''_{s,r}} \right\} \tag{11}$$

For equilibrium calculations, the implementation of the foregoing equations can be simplified by use of the so-called equilibrium constant from the law of mass action, which relates the forward and backward reaction rates according to

$$K_{c,r} = \frac{k_{f,r}}{k_{b,r}} \tag{12}$$

Conservation of Momentum.

The species conservation of momentum equation is given by

$$\frac{\partial}{\partial t}\left(\rho_s u_s^i\right) + \frac{\partial}{\partial x^j}\left(\rho_s u^i u^j\right) + \frac{\partial}{\partial x^j}\left(\rho_s u^i V_s^j + \rho_s u^j V_s^i\right) + \frac{\partial p_s}{\partial x^j} - \frac{\partial \tau_s^{ij}}{\partial x^j} = F_{ele,s}^i + F_{ela,s}^i + F_{inela,s}^i \tag{13}$$

The various forces $F^i_{m,s}$ arise from different collision types—namely, elastic or inelastic, neutral or charged species. Because of its importance in plasma, the electron momentum equation is stated explicitly here

$$\frac{\partial}{\partial t}\left(\rho_e u_e^i\right)+\frac{\partial}{\partial x^j}\left(\rho_e u^i u^j\right)+\frac{\partial}{\partial x^j}\left(\rho_e u^i V_e^j+\rho_e u^j V_e^i\right)+\frac{\partial p_e}{\partial x^j}-\frac{\partial \tau_e^{ij}}{\partial x^j}= -N_e\varepsilon E^i - N_e M_e \sum_r \nu_{er}^*\left(u_e^i-u_r^i\right) \tag{14}$$

where E^i is the electric field associated with either an external or induced electric field and ν_{er}^* is the effective collision frequency as given by Lee (1983, p.38). The electric field solution in the absence of an external or induced magnetic field reduces to a solution of the Poisson equation by which the space charge distribution within plasma is related to the electrostatic potential. The numerical solution of the Poisson equation is relatively expensive. Various approximate models may be used in order to evaluate the electric field in a computationally efficient manner, such as the electron gas pressure or ambipolar diffusion approximations. In the current implementation, it is assumed that electrons and ions diffuse in an ambipolar fashion, wherein the fluxes of electrons and ions are assumed to be equal and related to one another through the ambipolar diffusion coefficient D_a

$$\Gamma_e=\Gamma_I=\Gamma=D_a\nabla N \tag{15}$$

The electric field in such situations may be given by

$$E^i=\left[\frac{\left(D_I-D_e\right)}{\left(\mu_I+\mu_e\right)}\right]\left(\frac{\nabla N}{N}\right) \tag{16}$$

Having approximated the electric field in this way, the volumetric electric field force F^i_{ele} is given by

$$F^i_{ele} = \sum_s N_s e Z_s E^i \quad . \tag{17}$$

Finally, summing up the contribution from each species the total momentum equation is given as

$$\frac{\partial}{\partial t}\left(\rho\, u^i\right) + \frac{\partial}{\partial x^j}\left(\rho_s u^i u^j\right) + \frac{\partial p}{\partial x^j} - \frac{\partial \tau^{ij}}{\partial x^j} = F^i_{ele} + F^i_{ela} + F^i_{inela} \quad . \tag{18}$$

Thermal Nonequilibrium .

The popular two-temperature model approximates the nonequilibrium situation by postulating the existence of a common heavy-particle temperature T characteristic of the translational and rotational energy modes and a second temperature T_V characteristic of the energy contained within the combined vibrational energies of all diatoms, the electronic energy and the energy in the free electrons. This nonequilibrium model utilizes a single vibrational-electronic energy equation from which T_V is calculated (Gnoffo, *et al.*, 1990).

$$\frac{\partial}{\partial t}\left(\rho e_V\right) + \frac{\partial}{\partial x^j}\left(\rho e_V u^j\right) = -p_e \frac{\partial u^i}{\partial x^j} + \frac{\partial}{\partial x^j}\left[\left(\eta_v + \eta_e\right)\frac{\partial T_V}{\partial x^j}\right] + \left(\frac{\mathcal{M}_e}{\hat{N}}\right)\sum_{s,r}\dot{N}_{e_{s,r}}\left(\rho e\right)_{s,r} + Q_{ele,e} + Q_{inel,e} + Q_{T-V} - Q_{rad} + \sum_{s=mol.} \dot{\omega}_s D_s \tag{19}$$

The justification for a two-temperature model is based on two considerations: 1) the rapid energy transfer between the translation of free electrons and the vibrational motion of the diatoms and 2) that the distribution of internal energy among the low-lying

electronic states of the heavy particles may be characterized as being in equilibrium with the ground electronic state at the electronic temperature.

The multispecies multitemperature thermal model referred to throughout this dissertation consists in the following details regarding the conservation of energy among the various internal energy modes within the flow, together with the various terms which model the energy exchanges which take place between them. The key feature of this multispecies multitemperature model is the separate tracking of energy in the electron-electronic state, Equation (23), and in the vibrational energy manifolds of each diatomic species, Equation (27).

Conservation of Energy.

The expression for the conservation of internal energy for atomic and diatomic species is given by

$$\begin{aligned} &\frac{\partial}{\partial t}\rho_s\left(\frac{1}{2}u^2+u^iV_s^i+e_s\right)+\frac{\partial}{\partial x^j}\rho_s u^j\left(\frac{1}{2}u^2+e_s\right)+\frac{\partial q_s^j}{\partial x^j}+ \\ &\frac{\partial}{\partial x^j}\left(\frac{1}{2}\rho_s u^2V_s^j+\frac{1}{2}\rho_s u^ju^iV_s^i\right)+\frac{\partial}{\partial x^i}\left(u^ip_s\right)-\frac{\partial}{\partial x^j}\left(u^i\tau_s^{ij}\right)= \\ &\left(\frac{\mathcal{M}_s}{\hat{N}}\right)\sum_{s,r}\dot{N}_{s_{s,r}}\left(\rho e\right)_{s,r}+P_{ele,s}+Q_{ele,s}+Q_{inel,s}-Q_{rad} \end{aligned} \tag{20}$$

where the total species energy is given by the following equations according to the species kind.

Atoms:
$$e_s=\frac{3}{2}\frac{k}{m_s}T+\left(\frac{k}{m_s}\right)\theta_{el,s}\frac{\left(g_{1,s}/g_{0,s}\right)e^{-\theta_{el,s}/T_e}}{1+\left(g_{1,s}/g_{0,s}\right)e^{-\theta_{el,s}/T_e}}+e_s^0 \tag{21}$$

Diatoms:
$$e_s=\frac{5}{2}\frac{k}{m_s}T+\left(\frac{k}{m_s}\right)\frac{\theta_{v,s}}{e^{-\theta_{v,s}/T_v}-1}+\left(\frac{k}{m_s}\right)\theta_{el,s}\frac{\left(g_{1,s}/g_{0,s}\right)e^{-\theta_{el,s}/T_e}}{1+\left(g_{1,s}/g_{0,s}\right)e^{-\theta_{el,s}/T_e}}+e_s^0 \tag{22}$$

The electron-electronic energy conservation equation is very similar to the species conservation equation.

$$\begin{aligned}&\frac{\partial}{\partial t}\rho_e\left(\frac{1}{2}u^2+u^iV_e^i+e_e\right)+\frac{\partial}{\partial x^j}\rho_e u^j\left(\frac{1}{2}u^2+e_e\right)+\frac{\partial q_e^j}{\partial x^j}+\\&\frac{\partial}{\partial x^j}\left(\frac{1}{2}\rho_e u^2V_e^j+\frac{1}{2}\rho_e u^ju^iV_s^i\right)+\frac{\partial}{\partial x^i}\left(u^ip_e\right)-\frac{\partial}{\partial x^j}\left(u^i\tau_e^{ij}\right)=\\&\left(\frac{\mathcal{M}_e}{\hat{N}}\right)\sum_{s,r}\dot{N}_{e_{s,r}}\left(\rho e\right)_{s,r}+P_{ele,e}+Q_{ele,e}+Q_{inel,e}-Q_{rad,e}\end{aligned}\tag{23}$$

where the internal energy of electrons is given by

$$e_e=\frac{\left[3/2kT_e+\left\langle\varepsilon_{\text{int},e}\right\rangle\right]}{\mathcal{M}_e}\tag{24}$$

The electron energy conservation equation is stated separately from the general species energy conservation equation here to illustrate the additional source terms which play a relatively important role in the overall energy. The first such term represents the energy gained by the production of electrons.

$$\sum_{s,r}\dot{N}_{e_{s,r}}\left(\rho e\right)_{s,r}\tag{25}$$

The next term $P_{ele,s}$ models the work done by the electric field upon the electrons, which is also known as Joule heating.

$$P_{ele,s}=N_sZ_sE^iu_s^i\tag{26}$$

In lieu of a more detailed approach, such as solving the vibrational master equations *via* a detailed balancing procedure (Park, 1992), the vibrational energy conservation equation is solved for each of the diatomic species using the macroscopic nonequilibrium vibrational temperatures and the Landau-Teller formalism (Landau and Teller, 1936)

$$\frac{\partial}{\partial t}\left(\rho_s e_{v,s}\right)+\frac{\partial}{\partial x^j}\left(\rho_s e_{v,s}u^j\right)=\frac{\partial}{\partial x^j}\left(\eta'_{v,s}\frac{\partial T_v}{\partial x^j}\right)-\frac{\partial}{\partial x^j}\left(\rho_s e_{v,s}V_s^j\right)+ Q_{T-V}+Q_{V-V}+Q_{e-V}-Q_{rad-V}+\dot{\omega}_s D_s \tag{27}$$

The vibrational energy $e_{v,s}$ represents the total energy in the vibrational manifold of the diatomic species, which are modeled as harmonic oscillators. The energy levels are assumed to be populated by a Boltzmann distribution at the species vibrational temperatures. This assumption holds well for low vibrational states. High vibrational states deviate from this assumption, but the total energy contained in these higher levels is negligible (Lee, 1985). The source terms Q_{m-V} model the exchange of energy between the various energy modes. The effect of vibrational population depletion arising from dissociation is accounted for in the vibration-dissociation coupling term $\dot{\omega}_s D_s$.

The total energy conservation equation is given by

$$\frac{\partial}{\partial t}\left[\rho\left(\frac{1}{2}u^2+e\right)\right]+\frac{\partial}{\partial x^j}\left[\rho u^j\left(\frac{1}{2}u^2+e\right)\right]+\frac{\partial q^j}{\partial x^j}+\frac{\partial}{\partial x^j}\left(u^i p\right)- \frac{\partial}{\partial x^j}\left(u^i\tau^{ij}\right)=\sum_s N_e Z_s E^i u_s^i-Q_{rad} \tag{28}$$

where the total energy is given as

$$\rho e=\sum_{s\neq e}\rho_s C_{v,s}T+\frac{1}{2}\sum_{s\neq e}\rho_s u^i u^j+\sum_{s\neq e}\rho e_{v,s}+E_e+ \sum_{s\neq e}\rho_s h_s^0+\sum_{s\neq e}\rho_s e_{el,s} \tag{29}$$

The translational-rotational temperature is obtained from equation (29) by solving for T. In a similar fashion the species vibrational temperatures are recovered by solving the following expression for the energy contained in the harmonic oscillator for $T_{v,s}$

$$e_{v,s}=\rho\left(\frac{R}{\mathcal{M}_s}\right)\left[\frac{\theta_{v,s}}{e^{-\theta_{v,s}/T_{v,s}}-1}\right] \tag{30}$$

These are not only primary thermodynamic quantities of interest, but they are also needed to calculate reaction rates at the next time step. Additionally, they are needed as input into the radiation solver.

Transport Processes.

Accounting for the transport of mass, momentum and energy in the conservation equations is made somewhat more of a challenge for a high-temperature gas mixture. In order to calculate those terms which account for the non-convective transport of these quantities, it is first necessary to compute both mixture and species diffusivities, viscosities, and thermal conductivities. The species viscosities are calculated from the curve fits of Blottner (1971), which are known to be reasonably accurate up to 10,000 K (Josyula and Bailey, 2003). Unfortunately, reentry flowfields contain regions that are commonly at temperatures well outside this range. Therefore, these viscosity values are used tentatively, and it is here noted that it would be desirable at a later time to implement better suited curve fit data (Gupta, *et al.*, 1987), thus extending the viscosity calculation out to 30,000 K and reducing the uncertainty inherent in the current approach. The species thermal conductivities were calculated *via* Eucken's relation (Vincenti and Kruger, 1963)

$$\kappa_i = \mu_i \left(\frac{5}{2} C_{v,trans,i} + C_{v,int,i} \right). \tag{31}$$

From the species transport properties the, mixture viscosity and thermal conductivity were computed by using Wilke's semi-empirical mixing rule (Bird, 1960)

$$\mu_{mix} = \sum_{\alpha} \frac{[\mathrm{X}]_\alpha \, \mu_\alpha}{\sum_{\beta} [\mathrm{X}]_\beta \, \Phi_{\alpha\beta}} \tag{32}$$

where

$$\Phi_{\alpha\beta} = \frac{1}{\sqrt{8}}\left(1+\frac{\mathcal{M}_\alpha}{\mathcal{M}_\beta}\right)^{-1/2}\left[1+\left(\frac{\mu_\alpha}{\mu_\beta}\right)^{1/2}\left(\frac{\mathcal{M}_\beta}{\mathcal{M}_\alpha}\right)^{1/4}\right]^2 \tag{33}$$

Finally, it is noted that only ordinary diffusion is accounted for, whereby Ficke's Law

$$\rho_i u_i = -\rho D_{ij} \nabla c_i \tag{34}$$

is adequate in providing an estimate of the diffusion mass flux resulting from gradients in the species concentrations. This theory is in contrast with the higher order binary diffusion processes described by the Stefan-Maxwell equations (Cussler, 1976), which account for the influence of the diffusion of other species upon the diffusion of the species of interest.

Kinetic Processes.

The theoretical study of nonequilibrium gasdynamics is in large part an effort to understand and describe the nature of the kinetic processes which restore a gas to its equilibrium condition. Entire volumes could be (and have been) filled in efforts to catalog the various models which have been advanced to characterize these processes. Volumes 196 and 197 of the AIAA series Progress in Aeronautics (2002, 2004) provide such a listing of the most up-to-date information. The interested reader may consult these volumes for additional details concerning alternate approaches if desired. Only those process models which have been adopted in this solution methodology are discussed here. For ease of discussion, it is convenient to group these processes under one of the following headings: vibrational relaxation, chemical reactions and thermal ionization (Stupechenko, 1967).

Vibrational Relaxation.

The technique for modeling vibrational relaxation follows from the theoretical development presented in Vincenti and Kruger (1967) of the Landau Teller formalism. Making use of this theory, the rate of change of the vibrational energy due to the translational-vibrational coupling can be modeled by a simple linear ordinary differential equation of the form

$$\frac{dE_v}{dt} = \frac{E^*(T) - E_v}{\tau(T,p)} . \tag{35}$$

While the solution to the above differential equation is well-known, it depends on the local macroscopic thermodynamic state *via* the experimentally derived relaxation time $\tau_s(T,p)$. The species translational-vibrational relaxation time is calculated from the Landau-Teller interspecies relaxation times $\tau_{s,k}$ according to

$$\tau_s = \frac{\sum_s X_s}{\sum_k X_k / \tau_{s,k}} \tag{36}$$

The work of Milikan and White (1963) furnishes a suitable method and experimental data whereby to approximate the value of $\tau_{s,k}$. This approximation is accomplished by way of the experimental correlation

$$p\tau_{s,k} = \exp\left[A\left(T^{-1/3} - 0.015\mu^{1/2}\right) - 18.42 \right] \quad (\text{atm sec}) . \tag{37}$$

In this manner, the translational-vibrational energy exchange source term may be cast as

$$Q_{T-V} = \rho_s \frac{\left(e^*_{v,s} - e_{v,s}\right)}{\tau_s} . \tag{38}$$

The electron-vibrational energy exchange may be modeled as proposed by Lee (1985).

$$Q_{e-V} = \rho_s \frac{\left(e_{v,s}^{**}(T_e) - e_{v,s}(T_v)\right)}{\tau_{es}} \tag{39}$$

where $e_{v,s}^{**}$ is the vibrational energy taken to be at equilibrium with the electron temperature. Additionally, τ_{es} is calculated as

$$\tau_{es} = \frac{1}{\left(1 - e^{-\theta_v/T_e}\right)^2 K_0} \tag{40}$$

where the equivalent heat conductivity K_0 is given as

$$K_0 = \frac{1}{2} n_e \int k_{oj} (j)^2 dj \tag{41}$$

Data for τ_{es} is calculated for species N_2 only since the efficiency of vibrational excitation through electron impact is roughly two orders of magnitude less efficient for O_2, NO and NO+ (Park, 1992). However, if it should become of interest to investigate the contribution of electron impact excitation to the vibrational modes of these other species summaries of cross section and rate data may be obtained from the work of Ali (1981) and Slinker (1982).

Chemical Reactions.

The species mass source terms in the conservation equations are intended to model the contribution of the various chemical reactions involved such as dissociation, ionization, recombination and attachment. In order to calculate these rate terms, it is first necessary to have a means whereby to do so. For weakly ionized flows, the 7-species air model is considered to be a reasonable approximation of the significant kinetic processes. The species considered in the seven-species model (which the flow solver presently uses)

are O2, O, N2, N, NO, NO+ and e- and the significant kinetic processes are expressed in the following reaction equations.

$$\begin{aligned} N_2 + M &\rightleftharpoons 2N + M \\ O_2 + M &\rightleftharpoons 2O + M \\ NO + M &\rightleftharpoons N + O + M \\ N_2 + O &\rightleftharpoons NO + N \\ NO + O &\rightleftharpoons O_2 + N \\ N + O &\rightleftharpoons NO^+ + e^- \end{aligned} \tag{42}$$

The first three reactions are dissociation-recombination and the fourth and fifth are exchange reactions. The reaction rates for each equation are calculated according to the Arrhenius equation and the equilibrium constant which have been extended by use of an effective temperature T_a which takes the place of the usual equilibrium temperature

$$k_f\left(T_a\right) = C_f T_a^{\eta} \exp\left(\theta_d / T_a\right) \tag{43}$$

$$k_b\left(T_a\right) = \frac{k_f\left(T_a\right)}{K_{eq}\left(T_a\right)} \tag{44}$$

The constants required to evaluate the forward reaction rates k_f and the experimental curve-fit for K_{eq} are taken from (Park, 1985), more recent data on reaction rates may also be found in Park (1989, 1990, 1992), Gupta and Yos (1987) and Bose and Chandler (1997). The calculation of the effective temperature varies according to the nature of the reaction. For the dissociation-recombination reaction $T_a = T^{q-1}T_v^q$ is calculated according to the empirical relationship proposed by Park (1992) to model the vibrational-dissociation coupling. Typical values of the exponent q range from 0.3 to 0.5; 0.5 is used in the flow solver used in the present work. The reaction rates for exchange reactions

depend upon the translational temperatures of the diatomic molecules only, that is to say $T_a = T$

Thermal Ionization.

In the 7-species air model, there are two reactions by which NO is ionized—associative-ionization and electron-impact ionization. At speeds below about 9 km/s the associative-ionization process is dominant due to its relatively low reaction threshold (2.67 eV), as compared to that of electron-impact ionization (9.25 eV). In fact, the associative-ionization provides the seeding electrons which are responsible for the subsequent production of electrons in the electron avalanche process. As speed increases, the electron-impact ionization becomes dominant, and other species begin to ionize as well, forming N2+, O2+, N+ and O+. Again, in the present investigation only the formation of NO+ is considered (Park, 1985, 1986, 1987). The effective temperatures for associative-ionization and electron-impact ionization are taken as T and $\sqrt{TT_e}$, respectively, although electron-impact ionization is neglected in the present study. Only the forward reaction rates have been discussed in the subsections above. The reverse reaction rates may be calculated by using the equilibrium constant at the appropriate effective temperature.

Radiative Transport

Radiation in gas fields has long been studied by astrophysicists, for whom the spectral characteristics of the radiation from stars are the main experimental verification of astrophysical theories. As a result of these activities, a mature body of theory and a wealth of data exist concerning the spectral behavior of the gas species which must be modeled in a radiation-gasdynamic solution method (Pai, 1963; Hertzberg, 1950). In developing a suitable solution method, it is necessary to not only model the spectral behavior of the participating species but also the transport of radiation within the solution domain. Here again, a mature body of theory exists with an extensive array of highly sophisticated methods and techniques available to model the transport of radiation in a participating media, such as the high-temperature air surrounding a reentry vehicle (Modest, 2003). Therefore, the challenge in developing a suitable solution method lies not in an inadequate theoretical basis for the proposed models, rather in the fact that the computation of the most general transport models is prohibitively expensive. As such, varying degrees of approximation are accepted in the solution method—typically with regard to either or both the determination of the spectral behavior of the media or the solution of transport equation within the media. For instance, in years past step radiation models were quite standard in modeling the spectral behavior of the media, while in modeling the radiation transport, it has been a common practice, even to the present, to use the tangent-slab approximation. In order to address some of these issues, the following subsections will address in turn the various sources of emission and absorption within a high-temperature gas, the transport of the resulting radiation, and, finally, the coupling of the radiative energy into the governing gasdynamic equation set.

Emission and Absorption Mechanisms.

Calculating the solution of the radiative transport equation is a relatively straightforward matter in cold air, *vis-à-vis* high-temperature air. The reason that the latter is so much more difficult is that media such as high-temperature air are said to _participate' in the transport calculation by emitting and absorbing radiation within the solution domain; this transport is in addition to the radiative transport which is a result of the radiative boundary conditions. Therefore, where radiative transport in high-temperature gases is concerned, two major tasks are presented to be accomplished. The first task concerns the determination of the so-called emission and absorption coefficients within the gas volume. (The second task is the subsequent solving of the radiative transport equation. This discussion is deferred to the next section.) These coefficients are calculated through a combination of empirical and theoretical considerations which pertain to the mechanisms by which these phenomena occur—namely, the various electronic transitions which are possible in atomic and diatomic systems. There are three basic classes of transitions which are generally discussed: 1) free-free (Bremsstrahlung), 2) bound-free/free-bound (photoionization/-recombination), and 3) bound-bound (line and band spectra). The methods available for calculating the spectra which result from the above transition types are be discussed in the subsections which follow. In this presentation, discussion is restricted to that theory which is necessary to establish a common understanding of the basic principles implemented in SPRADIAN, the radiation solver utilized in this investigation (Fujita and Abe, 1997). Many excellent supporting texts also exist and have been consulted where they facilitate the discussion (Zeldovich and Raizer, 1967; Hertzberg, 1950; Penner and Olfe, 1968; and Park 1992).

Free-Free Transitions.

In high-temperature air, such as is observed at reentry speeds ($T > 15,000K$), atomic species are much more prevalent than the diatomic species, which have at this point mostly dissociated. Additionally, the reactions precipitated by electron-impact are well underway, whereby electrons collide with heavy particles such as ions and neutral particles. In these inelastic collisions, the electron may excite the heavy particle, possibly causing the heavy particle to ionize further, or alternately, to recombine with ions to reduce their degree of ionization, or even attach to neutrals to form negative ions. These types of collision are not considered for the moment, and instead the reader's attention is directed to the inelastic collisions between electrons and heavy particles, particularly ions, wherein an electron interacts with an ion but does not result in either ionization or recombination, rather in the emission or absorption of a photon

$$A^z + e_l + h\nu \rightleftharpoons A^z + e_u \tag{45}$$

where A^z is a heavy particle with z-valence, e_l and e_u are free electrons in lower and upper kinetic energy states respectively, and $h\nu$ is the photon. These types of collision are associated with the so-call free-free transitions, and they may result in the emission or absorption of a photon with energy $E = h\nu$ due to the acceleration, $\mathbf{w}$, experienced by the electron in the field of the heavy particle and corresponding to the resulting energy exchange

$$\Delta E = \frac{16\pi^2}{2}\frac{e^2}{c^3}\int_0^\infty \mathbf{w}_\nu^2 d\nu \;\; \mathbf{w}_\nu = \frac{1}{2\pi}\int_{-\infty}^{\infty} \mathbf{w}(t) e^{-i2\pi\nu t} dt \tag{46}$$

.

In the literature, the radiation resulting from this mechanism is referred to as bremsstrahlung, that is ~~–b~~raking radiation" (Zeldovich and Raizer, 1967).

The spectral coefficients may be conceptualized by utilizing the idea of a collision cross-section $\sigma_{ff}^{z-1}\left(\lambda, T_{el}\right)$. In the expressions below, for an ionized gas, with an equilibrium electron velocity distribution, the emission and absorption coefficients can be expressed in terms of electron and ion number density, wavelength, and electron temperature

$$\kappa'\left(\lambda\right) = n^z n_e \sigma_{ff}^{z-1}\left(\lambda, T_{el}\right)\left[1 - \exp\left(\frac{hc/\lambda}{kT_{el}}\right)\right] \tag{47}$$

and, by virtue of Kirchhoff's law,

$$\varepsilon\left(\lambda\right) = \frac{2hc^2}{\lambda^5} n^z n_e \sigma_{ff}^{z-1}\left(\lambda, T_{el}\right)\exp\left(-\frac{hc/\lambda}{kT_{el}}\right). \tag{48}$$

However, with the particular values of the cross-sections unknown for the moment, it is necessary to obtain them by some means.

Consider the Planck equation, which specifies the spectral radiation density distribution for equilibrium radiation

$$U_{\nu p} = \frac{8\pi h\nu^3}{c^3}\frac{1}{e^{h\nu/kT} - 1}. \tag{49}$$

From here, an expression for the absorption coefficient, a_ν, of the bremsstrahlung absorption per ion per electron is sought. In this sort of collision ions are considered stationary and electrons moving with velocity V. Then the absorption of radiation at equilibrium conditions, in the frequency interval ν to $\nu + d\nu$, per unit time per unit volume by electrons with velocity in the range V to $V + dV$ is given by

$$N_+ N_e U_{\nu p} d\nu \cdot cf\left(v\right) dv \cdot a_\nu \left(1 - e^{-h\nu/kT}\right). \tag{50}$$

where the factor $\left(1-e^{-h\nu/kT}\right)$ accounts for induced emission. The radiation emitted under the same conditions is

$$N_+ N_e f\left(\nu'\right) d\nu \nu' dq_\nu(\nu'). \tag{51}$$

Noting that $\nu d\nu = \nu' d\nu'$, the general relation between a_ν and the differential radiation cross section, $d\sigma_\nu$ is given

$$a_\nu = \frac{c^2 \nu'^2}{8\pi\nu^2 \nu} \frac{d\sigma_\nu(\nu')}{d\nu}. \tag{52}$$

Finally, noting that $dq_\nu = h\nu d\sigma_\nu$ and by utilizing the approximation for dq_ν given by Landau and Lifshitz (1962)

$$dq_\nu = \frac{32\pi^2}{3\sqrt{3}} \frac{Z^2 e^6}{m^2 c^3 \nu^2} d\nu \tag{53}$$

an expression for the unit absorption coefficient a_ν in terms of the degree of ionization Z, the electron velocity v and the frequency *v* is obtained

$$a_\nu = \frac{4\pi}{3\sqrt{3}} \frac{Z^2 e^6}{hcm^2 \nu \nu^3}. \tag{54}$$

In order to obtain the absorption coefficient, κ_ν, of the bremsstrahlung radiation at the electron temperature, the above expression may be multiplied by N_+ and N_e and averaged over the electron velocity by use of the Maxwell velocity distribution function.

$$\kappa'_\nu = \frac{4}{3}\left(\frac{2\pi}{3m_e kT}\right)^{1/2} \frac{Z^2 e^6}{hcm_e \nu^3} N_+ N_e \tag{55}$$

Again, the emission and absorption coefficients may be related through Kirchhoff's law.

$$\varepsilon_\nu = \frac{8}{3}\left(\frac{2\pi}{3m_e kT}\right)^{1/2} \frac{Z^2 h^2 e^6}{c^3 m_e} N_+ N_e e^{-h\nu/kT} \tag{56}$$

The above derivations used to develop expressions from the emission and absorption coefficients utilize classical mechanics in their approach (Griem, 1964). Predictions based on the classical mechanical approach differ from the quantum mechanical calculations by a factor referred to as the Gaunt factor (Zel'dovich and Raizer, 1967)

$$g_B = \left(\frac{dq_\nu}{d\nu}\right)_{quantum} \Big/ \left(\frac{dq_\nu}{d\nu}\right)_{classical} \tag{57}$$

The Gaunt factors used by SPRADIAN are taken from Peach (1970).

Bound-Free Transitions.

Now, the reader's attention is turned to the ionization-recombination collisions as developed in Zeldovich and Raizer (1967). In these collisions, energy must be absorbed or released by the electron-ion system as the electron is captured or, alternately, freed. This capturing or freeing of an electron may occur by transferring energy to or from the internal structure of the ion, a third body or a photon

$$A_l^{z-1} + h\nu \rightleftharpoons A_u^z + e \,, \tag{58}$$

where A^z is a heavy particle with z-valence, e is the free electron and $h\nu$ is energy of the photon. Here the transfer of energy by a photon is considered. Let us begin by considering the energy levels E_n of a hydrogenic atom which are given in terms of the principle quantum number n which ranges from 1 to ∞ at the ground and free states, respectively,

$$E_n = -\frac{I_H Z^2}{n^2} = -\frac{I}{n^2} \tag{59}$$

and

$$I_H = \frac{e}{2a_0} = \frac{2\pi^2 me^4}{h^2} \tag{60}$$

Here *I* denotes the ionization potential, whereby the binding energy of an electron in the *n-th* quantum state, $E_n = |E_n| = I/n^2$ is obtained. The energy of the emitted or absorbed photon then is given by

$$h\nu = E + |E_n| = \frac{mv^2}{2} + \frac{I_H Z^2}{n^2}. \tag{61}$$

Again, it is possible to calculate the emission and absorption coefficients by beginning with the principle of detailed balancing. The number of electrons captured in the photo-ionization process with electron speeds in the range v to v+dv and being captured into the *n-th* energy level of the ion per unit volume per unit time

$$N_+ N_e f(v) dv \cdot v \cdot \sigma_{cn}. \tag{62}$$

where N_+ and N_e are the number densities of ions and electrons and σ_{cn} is the capture cross section into the *n-th* level. This process results in the emission of photons in the frequency range ν to ν+dν.

Accounting for induced emission as before, the photoionization process from the n-th quantum level by photons of frequency ν in the range ν to ν+dν per unit volume per unit time is given by

$$N_n \frac{U_{\nu p}}{h\nu} f(v) dv \cdot c \cdot \sigma_{\nu n} \left(1 - e^{-h\nu/kT}\right). \tag{63}$$

where $\sigma_{\nu n}$ is absorption cross section for a photon $h\nu$ into the *n-th* state, N_n is the number of such atoms per unit volume. Assuming complete thermodynamic equilibrium, it is permissible to substitute the Maxwellian velocity distribution for *f(***v***)* and thus arrive at an expression for N_n

$$N_n = N_1 \frac{g_n}{g_1} e^{-\frac{(E_n - E_1)}{kT}} = N_1 \frac{g_n}{g_1} e^{-\frac{I}{kT}\left(1-\frac{1}{n^2}\right)}. \tag{64}$$

For a hydrogenic atom the degeneracy of the *n-th* energy level may be given by $g_n = 2n^2$. In the expression above N_1 represents the number of the atoms in the ground state with degeneracy $g_1 = 2$. The excitation energy E_n of a given state is given by $E_n - E_1 = I_H Z^2 \left(1 - 1/n^2\right) = I\left(1 - 1/n^2\right)$. In order to relate the cross sections for photoionization and recombination, Saha's equation is also needed

$$\frac{N_+ N_e}{N} = 2\left(\frac{2\pi mkT}{h^2}\right)^{3/2} \frac{z_+}{z} e^{-I/kT}. \tag{65}$$

where $N = z\frac{N_1}{g_1}$ and where z and $z_+ = 1$ are the partition functions of the atom and ion, respectively. Finally, equating the rates given by equations (62) & (63) and performing some algebraic substitutions, the following expression relating the photoionization and radiative capture cross sections is obtained as

$$\sigma_{\nu n} = \frac{z_+}{g_n}\left(\frac{m\nu c}{h\nu}\right)^2 \sigma_{cn}. \tag{66}$$

The emission cross section is given by

$$\sigma_{cn} = \frac{128\pi^4}{3\sqrt{3}} \frac{Z^4 e^{10}}{mc^3 h^4 \nu^2 \nu} \frac{1}{n^3} \tag{67}$$

and, finally, the absorption cross section is

$$\sigma_{\nu n} = \frac{64\pi^4}{3\sqrt{3}} \frac{e^{10} m Z^4}{h^6 c \nu^3 \nu^5} \propto \frac{n}{Z^2}\left(\frac{\nu_n}{\nu}\right)^3. \tag{68}$$

With the cross section thus obtained, the absorption coefficient follows according to the following expression, with the emission coefficient again obtained *via* Kirchhoff's law

$$\kappa'_{\nu} = \sum_{n^*}^{\infty} N_n \sigma_{n\nu} \,. \tag{69}$$

At each wavelength, the photon energy to a specific bound-free transition is calculated by subtracting the threshold energy from the energy at a particular wavelength. The Gaunt factor is obtained by interpolation from the look up table as before (Zeldovich and Raizer, 1967).

Atomic Bound-Bound Transitions.

The line spectra of atomic systems are the result of electronic transitions, whereby a photon may be either emitted or absorbed.

$$A_l + h\nu \rightleftharpoons A_u \tag{70}$$

Emission of radiation from an atomic system occurs in both a spontaneous and an induced manner. Spontaneous emission of a photon, with wavelength λ_{ul}, occurs due to the random transition of an electron from the upper to lower electronic energy levels *u* and *l*, respectively. This probability of transition is quantified through the Einstein coefficient A_{ul} and related to the emission coefficient through

$$\varepsilon_{\lambda} = \frac{n_u h c A_{ul}}{4\pi\lambda_{ul}} \Phi_{\lambda} \tag{71}$$

The contribution of the induced emission is taken into consideration with the total absorption, since both occur in proportion to the incident radiation. The Einstein B coefficient is used to quantify these processes and is related to the net absorption coefficient through

$$\kappa'_{\lambda} = \frac{h\lambda_{ul}}{c}\left(n_l B_{lu} - n_u B_{ul}\right)\Phi_{\lambda} \tag{72}$$

It is possible to recast the net absorption coefficient in terms of the Einstein A coefficient through the relations

$$A_{ul} = \frac{8\pi h}{\lambda_{ul}^3 B_{ul}} \tag{73}$$

and

$$g_u B_{ul} = g_l B_{lu} . \tag{74}$$

The resulting expression for the net absorption coefficient is thus

$$\kappa_\lambda ' = n_l \frac{A_{ul}\lambda_{ul}^4}{8\pi c}\frac{g_u}{g_l}\left(1 - \frac{n_u g_l}{n_l g_u}\right)\Phi_\lambda . \tag{75}$$

The line spectra emitted due to the bound-bound transitions within an atomic system are not discretely distributed over the wavelength domain, but in fact have a distribution about the wavelength λ_{ul} denoted by Φ_λ above, which is the Voigt line profile. This profile is the result of a phenomenon called line broadening. Three major classes of line broadening are customarily considered: natural broadening, Doppler broadening and pressure broadening. Natural line broadening is the result of the uncertainty principle and may be quantified relatively easily from an application of classical mechanics to a damped oscillator, whereby it is found that for radiation damping the half width of the line is independent of photon wavelength as is given by

$$\Delta\lambda_n = \frac{2\pi c\gamma}{\omega_0^2} = \frac{4\pi e^2}{3mc^2} = 1.18\times 10^{-4}\ \text{Å} . \tag{76}$$

Doppler broadening occurs due to random thermal velocity of the radiating atoms and results in a Gaussian distribution with a half width given by

$$\Delta\lambda_D = \left(\frac{2kT\ln 2}{\mathcal{M}_{ave}c^2}\right)^{1/2}\lambda_0 . \tag{77}$$

Pressure broadening is due to collisions with other particles. The calculation of the associated broadening parameters depends on the type of collision partner involved. Stark broadening is due to collisions with charged partners. The resulting collision width is calculated according to the following empirical relations. The results of Griem (1964) are used, when available, to quantify the full-half Stark

$$\Delta\lambda_S = \gamma\left(\frac{T_e}{10^4}\right)^n\left(\frac{N_e}{10^{16}}\right)\text{ Å}. \tag{78}$$

Where data is not available from Griem, the values of γ and n are evaluated according to the method proposed by Arnold and colleagues (1980)

$$\gamma = 0.42\left(\frac{\lambda}{\left(I - E_k\right)}\right)^2\text{ Å}. \tag{79}$$

Broadening also occurs due to non-resonant collisions

$$\Delta\lambda_{p,non-res} = 0.2w_H\sqrt{\frac{T}{10^4}}\left(\frac{N_H}{10^8}\right)nm = 5.85\times10^{-30}\sqrt{\frac{2T}{\mathcal{M}_{ave}}}N_{hvy}\lambda_0\text{ Å}. \tag{80}$$

In the case of resonant collisions, the citation within the source code comments matches the implemented code. From Traving,

$$\Delta\lambda_{p,res} = 5.48\pi\left(\frac{g_i}{g_k}\right)^{1/2}\frac{e^2 f_a}{2m\omega_0}n_i. \tag{81}$$

Noting that

$$\omega_0 = 2\pi\frac{c}{\lambda_0} \tag{82}$$

and taking the oscillator strength from Richter (1968)

$$f_a = 1.50\left(\frac{g_k}{g_i}\right)\lambda_0^2 A_{ki} \tag{83}$$

the desired line broadening term is thus obtain

$$\Delta\lambda_{p,res} = 8.22\left(\frac{g_k}{g_i}\right)^{1/2} \frac{e^2\lambda_0^3}{4mc\omega_0} A_{ki} n_i \ . \tag{84}$$

The broadening due to each of the foregoing mechanisms has been characterized by a single parameter, namely, the full width at half maximum (FWHM) associated with each. However, it is, in general, a difficult matter to describe the resulting line profile which results from the combination of these various widths. Therefore, it is done in an approximate way according to the method proposed by Olivero and Longbothom (1977), whereby

$$\begin{aligned}\Phi(\lambda) = A\Bigg\{&(1-t)\exp\left(-2.772L^2\right) + \frac{t}{1+4L^2} + \\ &0.016(1-t)t\left[\exp\left(-0.4L^{2.25}\right) - \frac{10}{10+L^{2.25}}\right]\Bigg\}\end{aligned} \tag{85 a.}$$

$$A = \frac{1}{\Delta\lambda_V\left(1.065 + 0.44t + 0.058t^2\right)} \tag{85 b.}$$

$$L = \frac{\lambda - \lambda_C}{\Delta\lambda_V} \tag{85 c.}$$

$$t = \frac{\Delta\lambda_L}{\Delta\lambda_V} \tag{85 d.}$$

$$\Delta\lambda_V = \frac{\Delta\lambda_L}{2} + \sqrt{\left(\frac{\Delta\lambda_L}{2}\right)^2 + \Delta\lambda_G} \tag{85 e.}$$

Diatomic Bound-Bound Transitions .

The band spectra of diatomic systems are significantly more complex to calculate than the line spectra of atomic systems. This increased level of complexity arises from the fact that while the internal energy of a molecule likewise depends on its electronic state, there is also a complex dependence on the excitation of the additional vibration and rotational energy modes and the various transitions possible among them. This additional complexity enters through the calculation of the Einstein A coefficient

$$A_{J'J''} = \frac{1}{4\pi\varepsilon_0}\frac{26\pi^4}{3h}\frac{1}{\lambda^3_{J'J''}}\frac{\left|R_{v'v''}\right|^2 S_{J'J''}}{2J'+1}. \tag{86}$$

via the electronic transition strength $\left|R_{v'v''}\right|^2$ and the Honl-London factor, $S_{J'J''}$, which quantify the probability of vibrational and rotational transitions, respectively. The electronic transitional dipole moment is found from the inner product of the vibrational and electronic wavefunctions, Ψ_v and Ψ_e, with the electronic transition dipole moment matrix element $\mathbf{M}_e$

$$\begin{aligned}\left|R_{v'v''}\right|^2 &= \left|\iint \Psi^*_{v'}\Psi^*_{e'}\mathbf{M}_e\Psi_{v''}\Psi_{e''}d\tau_e dr\right|^2 \\ &= \left|\int \Psi^*_{v'}R_e\Psi_{v''}dr\right|^2\end{aligned} \tag{87}$$

where the inner product of the electron wavefunction with the electron transition dipole matrix has been combined in the electron dipole moment, $R_e(r)$

$$R_e(r) = \int \Psi^*_{e'}\Psi^*_{v}\mathbf{M}_e\Psi_{v''}\Psi_{e''}d\tau_e. \tag{88}$$

This expression can be approximated through the Franck-Condon principle, where the weak dependence of the dipole moment $R_e(r)$ on the internuclear displacement, r, is approximated though the introduction of the v‘-v‘‘ transition centroid defined as

$$r_{v'v''} = \frac{\int \Psi^*_{v'} r \Psi_{v''} dr}{\int \Psi^*_{v'} \Psi_{v''} dr} \tag{89}$$

Since the vibrational and rotational wavefunctions are independent of the electronic coordinates (Zeldovich and Raizer, p. 317, 1967), it is permissible to pull $R_e(r_{v'v''})$ out of the integral such that the transition strength is approximated as

$$\left|R_{v'v''}\right|^2 \approx \left|R_e\left(r_{v'v''}\right)\right|^2 q_{v'v''} \tag{90}$$

where the Franck-Condon factor is defined by

$$q_{v'v''} = \left|\int \Psi^*_{v'} \Psi_{v''} dr\right|^2. \tag{91}$$

SPRADIAN utilizes a lookup table to evaluate the electronic transition strength $\left|R_{v'v''}\right|^2$ — the values of the table were computed *a priori* according to the method outlined by Fujita and Abe (1997). In this method, $R_e(r_{v'v''})$ is assumed to be given experimentally or through some suitable quantum mechanical calculation, while the Frank-Condon factor is calculated as follows.

It is clear from equation (91) that the chief difficulty in computing $q_{v'v''}$ lies in obtaining the inner product of the vibrational wavefunction in the *r* coordinate system. This wavefunction must be obtained *via* a suitable numerical solution (Cooley, 1961) to the radial Schrödinger equation,

$$-\frac{h}{8\pi^2 \mu c}\frac{\partial^2 \Psi_v}{\partial r^2} + \left[U\left(r\right) - E\right]\Psi_v = 0. \tag{92}$$

The method of Rydberg, Klein and Rees (1931, 1932, and 1947, respectively) is utilized to quantify the potential energy function in terms of the vibrational energy *G(v)* at a

particular vibrational level v and on the interval $\left[r_{inner}(v), r_{outer}(v)\right]$. The turning points of the vibrational motion are calculated according to the following relations

$$r_{inner}\left(v\right) = \sqrt{\frac{f\left(v\right)}{g\left(v\right)} + f\left(v\right)^2} - f\left(v\right), \tag{93 a.}$$

$$r_{outer}\left(v\right) = \sqrt{\frac{f\left(v\right)}{g\left(v\right)} + f\left(v\right)^2} + f\left(v\right), \tag{93 b.}$$

$$f\left(v\right) = \frac{\sqrt{h}}{2\pi\sqrt{2\mu c}} \int_{-1/2}^{v} \frac{dv'}{\sqrt{G\left(v\right) - G\left(v'\right)}}, \tag{93 c.}$$

and

$$g\left(v\right) = \frac{2\pi\sqrt{2\mu c}}{\sqrt{h}} \int_{-1/2}^{v} \frac{B_{v'}dv'}{\sqrt{G\left(v\right) - G\left(v'\right)}} \tag{93 d.}$$

where $B_{v'}$ is the rotational constant for the v‘ vibrational level. For a singlet state, the vibrational energy *G(v)* may be given by the Dunham expansion

$$G\left(v\right) = \omega_e\left(\frac{1}{2} + v\right) - \omega_e x_e\left(\frac{1}{2} + v\right)^2 + \omega_e y_e\left(\frac{1}{2} + v\right)^3 - \omega_e z_e\left(\frac{1}{2} + v\right)^4 \tag{94}$$

where the vibrational constants, ω_e, $\omega_e x_e$, $\omega_e y_e$ and $\omega_e z_e$, are taken from complied spectroscopic data such as that found in (Hertzberg, 1950; Jaffe 1987). Interpolation and extrapolation is based on a Morse-type function, as in (Gilmore, 1992). First, the inverse Morse function is defined by

$$L\left(r\right) \equiv -\beta\left(r - r_e\right), \tag{95}$$

where r_e is the equilibrium bond distance and β is given as

$$\beta = \sqrt{\frac{2\pi^2 c^2 \mu}{D_e}}\omega_e. \tag{96}$$

The inverse Morse function has the follow relationship to the potential energy

$$U(r) = D_e\left[1 - e^{L(r)}\right]^2. \tag{97}$$

where D_e is the quantum well depth for the given electronic state. With the potential energy determined as above, it is introduced into the radial Schrödinger equation in order to solve for the vibrational wavefunctions ψ_v and finally the transition strength $\left|R_{v'v''}\right|^2$.

The Honl-London factor $S_{J'J''}$ quantifies the relative probability of transition between rotational levels J' and J'. Only singlet bands (i.e., $S' = S'' = 0$) are considered in the present study. A compilation of Honl-London factors is available for many types of transitions (Shadee, 1964), and those for the singlet bands are listed below in Table 1. The current version of SPRADIAN includes upper to lower transitions for the Σ-Σ, Π-Π, Π-Σ and Σ-Π electronic configurations. Line shape and line widths are calculated as in the previous section for the J=0 line of each band. This line shape is stored in an array and used for the other lines within the same band (i.e., those transitions which share the same v‘ and v‘‘).

Table 1. Honl-London Factors for Singlet Band Spectra

$\Lambda' - \Lambda''$	$J' - J'' = +1$ (P-Branch)	$J' - J'' = 0$ (Q-Branch)	$J' - J'' = -1$ (R-Branch)
+1	$\frac{(J'+1-\Lambda')(J'+2-\Lambda')}{2(J'+1)}$	$\frac{(J'+\Lambda')(J'+1-\Lambda')(2J'+1)}{2J'(J'+1)}$	$\frac{(J'+\Lambda')(J'-1+\Lambda')}{2J'}$
0	$\frac{(J'+1+\Lambda')(J'+1-\Lambda')}{(J'+1)}$	$\frac{(2J'+1)\Lambda'^2}{J'(J'+1)}$	$\frac{(J'+\Lambda')(J'-\Lambda')}{J'}$
-1	$\frac{(J'+1+\Lambda')(J'+2+\Lambda')}{2(J'+1)}$	$\frac{(J'-\Lambda')(J'+1+\Lambda')(2J'+1)}{2J'(J'+1)}$	$\frac{(J'-\Lambda')(J'-1-\Lambda')}{2J'}$

Nonequilibrium State Populations in Atomic Systems.

In the foregoing discussion of the various radiation mechanisms, it was assumed that the electronic states of the atomic state were populated according to the equilibrium distribution. This assumption was only a convenience of presentation, since ultimately one is interested in the effects of the nonequilibrium distributions upon the respective radiation mechanism above and the transport of radiation within the flowfield. In a general sense, the nonequilibrium state populations must be calculated by time-integration of the following set of differential equations

$$\frac{\partial N_i}{\partial t} = \sum_{j=1}^{m} K(i,j) N_j N_e + K(c,i) N_+ N_e^2 + \sum_{j=1}^{m} A(i,j) N_j + A(c,i) N_+ N_e - \sum_{j=1}^{m} K(i,j) N_i N_e - K(i,c) N_i N_e - \sum_{j=1}^{m} A(i,j) N_i - A(i,c) N_i. \tag{98}$$

However, such a calculation is rather impractical, not to mention unnecessary at conditions of practical interest. Instead, the calculation of the non-Boltzmann distributions is performed according to the Quasi-Steady-State (QSS) approximation, as described by Park (1992). The QSS approximation is based on the fundamental assumption that the respective sums of the ingoing and outgoing rates of transition between electronic states are each much greater than the time rate of change of the given state population

$$\left| \frac{\partial N_i}{\partial t} \right| << \sum_{j=1}^{m} K(i,j) N_j N_e + K(c,i) N_+ N_e^2 + \sum_{j=1}^{m} A(i,j) N_j + A(c,i) N_+ N_e \tag{99}$$

and

$$\left| \frac{\partial N_i}{\partial t} \right| << \sum_{j=1}^{m} K(i,j) N_i N_e + K(i,c) N_i N_e + \sum_{j=1}^{m} A(i,j) N_i + A(i,c) N_i \,. \tag{100}$$

Consequently, one may set the LHS of equations (99) and (100) to zero and proceed to develop a suitable method for obtaining a solution to the set of m algebraic equations

$$\sum_{j=1}^{m} K(i,j) N_j N_e + K(c,i) N_+ N_e^2 + \sum_{j=1}^{m} A(i,j) N_j + A(c,i) N_+ N_e - \sum_{j=1}^{m} K(i,j) N_i N_e - K(i,c) N_i N_e - \sum_{j=1}^{m} A(i,j) N_i - A(i,c) N_i = 0. \tag{101}$$

Before proceeding with the development of the master equation, the author shall pause to introduce a couple of definitions related to the ratio of number densities for a particular electronic state *i* and the total number density of a particular species *a*:

$$\rho_i = N_i / N_{iE} \tag{102 a.}$$

$$\chi = N_a / N_{aE}. \tag{102 b.}$$

In these expressions, *E* denotes the hypothetical equilibrium values of these number densities as given by

$$N_{iE} = \frac{g_i N_+ N_e}{2Q_+} \left(\frac{h^2}{2\pi m_e k T_e} \right)^{3/2} \exp\left(\frac{E_\infty - E_i}{k T_e} \right) \tag{103 a}$$

where

$$N_{aE} = \sum_{i=1}^{m} N_{iE}. \tag{103 b}$$

Now, by substitution of these ratios into equation (100), the desired final form is obtained

$$\sum_{j=1}^{m} \left[K(i,j) + \frac{N_{jE}}{N_{iE}} \frac{A(j,i)}{N_e} \right] \rho_j + K(i,c) + A(c,i) \frac{N_+}{N_{iE}} = \left[\sum_{j=1}^{m} K(i,j) + K(i,c) + \frac{\sum_{j=1}^{m} A(i,j) + A(i,c)}{N_e} \right] \rho_i. \tag{104}$$

One must also take care that any solution to the foregoing equation does not violate the basic conservation relation

$$\sum_{i=1}^{m} \frac{N_{iE}}{N_e} \rho_i = \chi \frac{N_{aE}}{N_e} . \tag{105}$$

Unfortunately, this last expression creates a system of *m+1* equations. With the help of Park's intuition that the QSS approximation is least likely to be satisfied by the ground state, thus the foregoing derivation results in a convenient linear system in ρ and χ

$$\mathbf{M}\rho = \mathbf{C} + \mathbf{D}\chi . \tag{106}$$

where the matrix **M** and the vectors **C** and **D** are strictly functions of the electron temperature and number density. For clarity, the form of $\mathbf{M}\, C_1 = 0$, **C** and **D** is illustrated below.

-First row:

$$M(1, j) = N_{jE} / N_e \tag{107 a.}$$

$$C_1 = 0 \tag{107 b.}$$

$$D_1 = N_{aE} / N_e . \tag{107 c.}$$

-Diagonal elements of **M** matrix:

$$M(i,i) = \sum_{j=1}^{m} K(i, j) + K(i,c) + \frac{\sum_{j=1}^{m} A(i, j) + A(i,c)}{N_e} . \tag{107 d.}$$

-Off-diagonal elements of **M** matrix:

$$M(i, j) = -\left[K(i, j) + \frac{N_{jE}}{N_{iE}} \frac{A(j,i)}{N_e} \right] . \tag{107 e.}$$

-Vector **C**, i $\neq$ 1:

$$C_j = K(j,c) + A(c,j)\frac{N_+}{N_{iE}}. \qquad (107\text{ f.})$$

-Vector **D**, i ≠ 1:

$$D_j = 0. \qquad (107\text{ g.})$$

Nonequilibrium State Populations in Diatomic Systems.

The problem of calculating the nonequilibrium electronic state populations in diatomic systems is very similar to the problem just covered for atomic systems. Again the most general solutions would require the time integration of the master equation

$$\frac{\partial N_v}{\partial t} = N_x \sum_{v=0}^{m} K(v',v) N_{v'} + K(c,v) N_A N_B N_x - N_x \sum_{v=0}^{m} K(v',v) N_v - K(v,c) N_v N_x \qquad (108)$$

However, one may again apply the QSS assumption, thereby approximating the problem with a set of algebraic equations. To begin, consider the hypothetical equilibrium number density of the electronic state *i* of the diatom produced by the reaction of $atom_1$ with $atom_2$

$$\frac{n_1 n_2}{n_{iE}} = \frac{Q_1 Q_2}{Q_i} \exp\left(-\frac{D}{kT_e}\right) \qquad (109)$$

$$Q_i = g_i \exp\left(-\frac{E_e}{kT}\right) \sum_v \exp\left(1\frac{G_v}{kT_v}\right) \sum_J (2J+1) \exp\left(-\frac{F_J}{kT}\right). \qquad (110)$$

where the dissociation limit is denoted by D and the electron temperature by T_e The QSS master equation has the same form as for atomic systems,

$$\mathbf{M} = \mathbf{C} + \mathbf{D}\chi \qquad (111)$$

although the definitions of the matrix **M** and the vectors **C** and **D** have changed as detailed below

-First row:

$$M(i,j) = \frac{n_{jE}}{\sum_j n_{jE}} \tag{112 a.}$$

$$C_1 = 0 \tag{112 b.}$$

$$D_1 = 1\,. \tag{112 c.}$$

-Diagonal elements of **M** matrix:

$$M(i,i) = -K_e(i,c)\frac{n_e}{n_h} - K_h(i,c) - \sum_j \left[K_e(i,j)\frac{n_e}{n_h} + K_h(i,j) + \frac{A(i,j)}{n_h} \right]. \tag{112 d.}$$

-Off-diagonal elements of **M** matrix:

$$M(i,j) = K_e(i,j)\frac{n_{E,e}(i)}{n_{E,e}(j)}\frac{n_{E,h}(j)}{n_{E,h}(i)}\frac{n_e}{n_h} + K_h(i,j) + \frac{A(i,j)}{n_h}\frac{n_{E,h}(j)}{n_{E,h}(i)}\,. \tag{112 e.}$$

-Vector **C**, i $\neq$ 1:

$$C(i) = -K_e(i,c)\frac{n_{E,e}(i)}{n_{E,h}(i)} - K_h(i,c)\,. \tag{112 f.}$$

-Vector **D**, i $\neq$ 1:

$$D(j) = 0\,. \tag{112 g.}$$

In the expressions above, the heavy-particle excitation rate coefficients are calculated from empirical curve-fit data expressed in the Arrhenius form

$$K_h(i,j) = A\left(\frac{T_e}{6000}\right)^n \exp\left(-\frac{T_d}{T_e}\right), \tag{113}$$

where the parameters A, n and T_d are read into the computer program. The bound-bound electron impact excitation rate coefficients are calculated numerically as proposed by

Park. The average excitation rate corresponding to the transition between the electronic states $\bar{e}$ and $\bar{e}$' is expressed as

$$K(\bar{e},\bar{e}') = \frac{\sum_v \exp\left(-\frac{G_v}{kT_v}\right)\sum_J (2J+1)\exp\left(-\frac{F_J}{kT}\right)}{\sum_v \exp\left(-\frac{G_v}{kT_v}\right)\sum_J (2J+1)\exp\left(-\frac{F_J}{kT}\right)} * \frac{\sum_{v'} q(v,v')\sum_{J'}(2J'+1)K(e,v,J;e',v',J')}{\sum_v \exp\left(-\frac{G_v}{kT_v}\right)\sum_J (2J+1)\exp\left(-\frac{F_J}{kT}\right)}, \quad (114)$$

where ζ represents the electron-impact cross section for the diatomic species under consideration. This expression is in effect an average of the electron-impact transition coefficient between states (e,v,J) to (e',v',J') over the quantum numbers (v,J) as given by

$$K(e,v,J;e',v',J') = \frac{8\pi}{\sqrt{m_e}}\left(\frac{1}{2\pi k T_e}\right)^{3/2}\int_{E^*}^{\infty}\sigma\exp\left(-\frac{E}{kT_e}\right)EdE \quad (115)$$

The average is taken into account according to three considerations. First, the rate coefficient is weighted according to the _multiplicity' of each vibrational and rotational level within the initial electronic level. This weighting is accomplished through the sums

$$\sum_v \exp\left(-\frac{G_v}{kT_v}\right) \quad (116)$$

and

$$\sum_J (2J+1)\exp\left(-\frac{F_J}{kT}\right) \quad (117)$$

which are normalize by the denominator, the product of the sums of these initial state multiplicities. This result is easily confirmed by the definition of the partition function for the vibrational and rotational modes. Second, the rate coefficient is weighted

according to probability of a v-to-v‘ transition, through the Franck-Condon factor, $q(v,v')$. Finally, the rate coefficient is weighted according to the degeneracy of the final rotational state, given by the quantum number J‘.

Radiative Transport Equation

Having discussed the theory associated with the first major task in calculating the radiation field, the remainder of the discussion is directed towards obtaining a solution to the radiative transport equation. The radiative transport equation, in a non-scattering medium, is given in differential form along a single ray as

$$\frac{dI}{dx} = \varepsilon - \kappa' I \tag{118}$$

If one considers a region where the emission and absorption coefficients are uniform, such as at equilibrium, the radiative transport equation has a simple, closed-form solution

$$I = \frac{\varepsilon}{\kappa'}\left(1 - e^{-\kappa' x}\right) \tag{119}$$

This result is fundamental to the well-known radiative transport solution method discussed below.

Tangent-Slab Approximation

The method of solving the radiative transport equation used in this research is the well-known tangent-slab approximation (Modest, 2003). This method of approximation splits up the solution into to equal directional components (one forward and on reverse) along a particular ray. The radiative flux is calculated by assuming that each grid volume constitutes a thermodynamically homogeneous layer (Greendyke, 1992), whereby the

spectral radiative flux may be posed in terms of the known intensity of the preceding layer

$$I_\lambda = \left(\frac{\varepsilon_\lambda}{\kappa'_\lambda} \right) \left(1 - e^{-\kappa_\lambda z} \right) + I_{\lambda 0} e^{-\kappa_\lambda z} \tag{120}$$

The radiative flux in a given layer can then be integrated over a 2π steradians solid angle and over the wavelength interval of the spectral segment under consideration to obtain the incident radiative flux. This integration is continued in marching fashion, from the shock to the wall, along a path normal to the body.

Conservation Relation for Radiative Energy.

Finally, the radiative transport equation may be more generally stated in a conservative integral form as

$$\int_{\Omega_i} \int_{\Gamma} I_\nu \left(\hat{s} \cdot \hat{n} \right) d\Gamma d\Omega = \int_{\Omega_i} \int_{V} \left(\varepsilon_\nu - \kappa'_\nu I_\nu \right) dV d\Omega \tag{121}$$

A number of radiative transport schemes which are more spatially and directional general than the two so far discussed may be developed from this conservation statement. One such approach is the finite volume method of radiative transport. The details of this method and its application in the present investigation are briefly discussed in the following chapter (Modest, 2003).

IV. Methodology

Flowfield Solution Procedure

This section describes the implementation of the foregoing theory in a suitable numerical framework v*ia* the flowfield solver NH7AIR. The system of equations set forward in the previous chapter (consisting of the Navier-Stokes equations and the various source terms, therein considered) completely describes the physics of a flowfield in thermochemical nonequilibrium—within, of course, the inherent limitations of the assumed physical models. This set of equations however is not suitable, in its present form, for obtaining numerical solutions. Therefore, it has been recast, according to the method presented by (Walters, *et al.*, 1990), wherein the flowfield equations are numerically solved *via* a finite volume implementation of a Roe-approximate Riemann solver. This approach involves the solution of the local Riemann problem at the cell interfaces between finite volumes. The scheme developed for perfect gases developed by Roe (1986) has been extended in order to consider thermodynamic and chemical nonequilibrium in three dimensional flows. The treatment of nonequilibrium proposed by Walters and his colleagues is presented here, following a summary of the method originally proposed by Roe.

Roe Flux-Difference Splitting.

This method begins by casting the overall flowfield solution in terms of an ensemble of Riemann problems at the interfaces between the finite volume cells in the solution domain. With the problem thus defined, Roe observes that ~~t~~he Riemann

solution for any set of linear conservation laws is easily computed." Therefore, the derivation of a suitable scheme begins by considering the linear system

$$\frac{d\mathbf{w}}{dt} + \mathbf{A}\frac{d\mathbf{w}}{dx} = 0 \tag{122}$$

where $\mathbf{w} = \{\rho, \rho u, v\rho, ..., \rho e\}$ is the vector of conserved variables and **A** is the constant Jacobian matrix defined by $\partial \mathbf{F} / \partial \mathbf{w}$. If the conserved variables to the left and right of the cell interface, $\mathbf{w}_L$ and $\mathbf{w}_R$, are known, the flux difference may be uniquely expressed as

$$\mathbf{F_R} - \mathbf{F_L} = \alpha_k \lambda_k \mathbf{e}_k , \tag{123}$$

where the set $\{\mathbf{e}_k\}$ contains the right eigenvectors of A. In this way, the contribution of the *k-th* wave to the flux difference in given in terms of the wave strength α_k and wave speed λ_k. It is evident at this point that the flux at the cell interface (i+1/2) may be computed by either expression

$$\mathbf{F}_{i+1/2}\left(\mathbf{w}_L, \mathbf{w}_R\right) = \mathbf{F_L} + \sum\nolimits^{(-)} \alpha_k \lambda_k \mathbf{e}_k \tag{124 a.}$$

or

$$\mathbf{F}_{i+1/2}\left(\mathbf{w}_L, \mathbf{w}_R\right) = \mathbf{F_R} + \sum\nolimits^{(+)} \alpha_k \lambda_k \mathbf{e}_k . \tag{124 a.}$$

By averaging the two foregoing expressions

$$\mathbf{F}_{i+1/2}\left(\mathbf{w}_L, \mathbf{w}_R\right) = \frac{1}{2}\left(\mathbf{F_R} + \mathbf{F_L}\right) + \frac{1}{2}\sum \alpha_k \left|\lambda_k\right| \mathbf{e}_k \tag{124 a.}$$

In order to apply the foregoing expression to a nonlinear problem, one must first define a local linearization by utilizing $\tilde{\mathbf{A}}\left(\mathbf{w_L}, \mathbf{w_R}\right)$, wherein the eigenvalues and eigenvectors of the resulting linearization not only satisfy equation (122) but also the

eigenvectors form a suitable basis set whereby the ‗jump' in the conserved variables across the cell face may be specified by the linear combination

$$\mathbf{w_R} - \mathbf{w_L} = \sum_k \alpha_k \mathbf{e}_k \tag{125}$$

Ingeniously, this expression returns the exact solution whenever $\mathbf{w}_L$ and $\mathbf{w_R}$ lie on opposite sides of a flow discontinuity. Here then one must also require that the Rankin-Hugoniot relationship hold, which is

$$\mathbf{F_R} - \mathbf{F_L} = S\left(\mathbf{w_R} - \mathbf{w_L}\right), \tag{126}$$

where S is the shock speed. It is also required that for all *k*

$$S\alpha_k = \lambda_k \alpha_k \tag{127}$$

This statement requires that all α_k except one must vanish. Expressions for the Roe-averaged values $\hat{\alpha}_k$, $\hat{\lambda}_k$ and $\hat{\mathbf{e}}_k$ are given by Roe (1981). Substitution of these values back into the final expression for $\mathbf{F}_{i+1/2}$, gives the desired solution to the locally linearized cell-interface problem. The method does not however allow for the finite spatial distribution of expansion wave phenomena. These phenomena can be accommodated by an entropy fix which will be discussed later in this section.

Having briefly reviewed the Roe flux-splitting scheme developed for the Euler equations, consider the extension of this scheme to accommodate thermochemical nonequilibrium, as previously discussed (Walters, *et al.*, 1990). The governing equation may be written in a conservative vector from in 2D Cartesian coordinates as

$$\frac{\partial Q}{\partial t} + \frac{\partial}{\partial x}\left(\hat{F} - \hat{F}_v\right) + \frac{\partial}{\partial y}\left(\hat{G} - \hat{G}_v\right) = W\,, \tag{128}$$

where Q is the vector of conserved variables, W is the vector of source terms, $\hat{F}$ and $\hat{G}$ are the inviscid flux vectors and $\hat{F}_v$ and $\hat{G}_v$ are the viscous flux vectors. The vectors of conserved variables and source terms are given below.

$$Q = \begin{pmatrix} \rho_1 \\ \rho_2 \\ \vdots \\ \rho_N \\ \rho u \\ \rho v \\ \rho w \\ \rho_1 e_{n1} \\ \vdots \\ \rho_M e_{n_M} \\ \rho e_0 \end{pmatrix}, \qquad W = \begin{pmatrix} \dot{\omega}_1 \\ \dot{\omega}_2 \\ \vdots \\ \dot{\omega}_N \\ \sum \varepsilon N_s Z_s E^x \\ \sum \varepsilon N_s Z_s E^y \\ \sum \varepsilon N_s Z_s E^z \\ \dot{\omega}_1 D_1 + Q_{T-V,1} + Q_{e-V,1} + Q_{rad-V,1} \\ \vdots \\ \dot{\omega}_e e_{e_s} + \sum_{s,r} \dot{N}_{e_{s,r}} (\rho e)_{s,r} + P_{ele} + Q_{T-e} - \sum Q_{e-V} \\ 0 \end{pmatrix} \tag{129}$$

Before introducing the inviscid flux vectors it is necessary to introduce some nomenclature. The arithmetic average of a quantity f is calculated from the left and right states, as indicated by subscripts l and r, and is denoted by angled brackets below. Squared brackets denote the jump of quantity f across the cell interface.

$$\langle f \rangle = \frac{f_l + f_r}{2} \tag{130 a.}$$

$$f = f_r - f_l \tag{130 b.}$$

The approximate Riemann solution requires the determination of the cell interface fluxes. This flux is calculated as a summation over the absolute values of the wave speeds A, B and C.

$$\hat{F} = \left\langle \left[\!\left[\hat{F} \right]\!\right] \right\rangle - \left\langle \left[\!\left[\hat{F}\left(|\lambda_i|\right) \right]\!\right] \right\rangle \tag{131 a.}$$

where

$$\left[\!\left[\hat{F} \right]\!\right] = \left[\!\left[\hat{F} \right]\!\right]_A + \left[\!\left[\hat{F} \right]\!\right]_B + \left[\!\left[\hat{F} \right]\!\right]_C . \tag{131 b.}$$

The $\left[\!\left[\hat{F} \right]\!\right]_A$ vector corresponds to the eigenvalue $\lambda_A = \hat{u}$ and is calculated as indicated below

$$\left[\!\left[\hat{F} \right]\!\right]_A = \frac{|\nabla \xi|}{J}\left(\begin{array}{cc} \rho & -\dfrac{p}{\hat{a}^2} \end{array} \right)\hat{\tilde{u}} \begin{pmatrix} \hat{\rho}_1 \\ \hat{\rho}_2 \\ \vdots \\ \hat{\rho}_N \\ \hat{u} \\ \hat{v} \\ \hat{w} \\ \hat{e}_{n1} \\ \vdots \\ \hat{e}_{nM} \\ \hat{h}_0 - \hat{a}^2/(\hat{\gamma}-1) \end{pmatrix} + \frac{|\nabla \xi|}{J}\hat{\rho}\hat{\tilde{u}} \begin{pmatrix} \rho_1/\rho \\ \rho_2/\rho \\ \vdots \\ \rho_N/\rho \\ u \;\; -\xi_x \;\; \tilde{u} \\ v \;\; -\xi_y \;\; \tilde{u} \\ w \;\; -\xi_z \;\; \tilde{u} \\ \rho_1 e_{n1}/\rho \\ \vdots \\ \rho_M e_M/\rho \\ \Theta \end{pmatrix}, \tag{132 a.}$$

where

$$\Theta = \left(\hat{u} \;\; u \;\; + \hat{v} \;\; v \;\; + \hat{w} \;\; w \;\; \right) - \hat{\tilde{u}} \;\; \tilde{u} \;\; + \sum_{j=1}^{M} \left[\!\left[\frac{\rho_j e_{nj}}{\rho} \right]\!\right] - \sum_{i=1}^{N} \hat{\psi}_i \left[\!\left[\frac{\rho_i}{\rho} \right]\!\right]. \tag{132 b.}$$

In the same way the vectors $\left[\!\left[\hat{F} \right]\!\right]_{B,C}$ may be calculated from the eigenvalues $\lambda_{B,C} = \hat{u} \pm \hat{a}$

$$\left[\!\left[\hat{F}\right]\!\right]_{B,C} = \frac{|\nabla\xi|}{J}\frac{1}{2\hat{a}^2}\begin{pmatrix} p & \pm\hat{\rho}\hat{a} & \tilde{u} \end{pmatrix}\begin{pmatrix} \hat{\tilde{u}}\pm\hat{a} \end{pmatrix}\begin{pmatrix} \hat{\rho}_1 \\ \hat{\rho}_2 \\ \vdots \\ \hat{\rho}_N \\ \hat{u}\pm\xi_x\hat{a} \\ \hat{v}\pm\xi_y\hat{a} \\ \hat{w}\pm\xi_z\hat{a} \\ \hat{e}_{n1} \\ \vdots \\ \hat{e}_{nM} \\ \hat{h}_0 \pm\hat{\tilde{u}}\hat{a} \end{pmatrix}. \tag{133}$$

The needed Roe-averaged quantities were calculated as indicated below

$$\hat{\rho} = \sqrt{\rho_r\rho_l}\,, \tag{134 a.}$$

$$\hat{u} = \frac{\left\langle u\sqrt{\rho}\right\rangle}{\left\langle\sqrt{\rho}\right\rangle}, \quad \hat{v} = \frac{\left\langle v\sqrt{\rho}\right\rangle}{\left\langle\sqrt{\rho}\right\rangle}, \quad \hat{w} = \frac{\left\langle w\sqrt{\rho}\right\rangle}{\left\langle\sqrt{\rho}\right\rangle}, \tag{134 b.}$$

$$\hat{\rho}_i = \frac{\left\langle(\rho_i/\rho)\sqrt{\rho}\right\rangle}{\left\langle\sqrt{\rho}\right\rangle}, \qquad i = 1,...,N\,. \tag{134 c.}$$

Nonequilibrium energy terms are calculated according to

$$\hat{e}_{n_j} = \frac{\left\langle\left(\rho_j e_{n_j}/\rho\right)\sqrt{\rho}\right\rangle}{\left\langle\sqrt{\rho}\right\rangle}, \qquad i = 1,...,M\,. \tag{134 d.}$$

And the additional thermodynamic properties of enthalpy and entropy are calculated as

$$h_o = \frac{\left\langle h_o\sqrt{\rho}\right\rangle}{\sqrt{\rho}}, \qquad \psi_i = \frac{R_i T}{\hat{\gamma}-1} - \hat{e}_i + \frac{\hat{q}^2}{2}\,. \tag{134 e.}$$

where

$$T = \frac{\left\langle T\sqrt{\rho} \right\rangle}{\left\langle \sqrt{\rho} \right\rangle}, \quad \hat{e}_i = \frac{\left\langle \tilde{e}_i \sqrt{\rho} \right\rangle}{\left\langle \sqrt{\rho} \right\rangle}. \tag{134 f.}$$

Finally the average local speed of sound is calculated from the following relation

$$\hat{a}^2 = \left(\hat{\gamma} - 1\right)\left[\hat{h}_0 - \frac{\hat{q}^2}{2} + \hat{c}_v^* - \sum_{i=1}^{N} \hat{\rho}_i \hat{e}_i - \sum_{j=1}^{M} \hat{e}_{n_j} \right] \tag{134 g.}$$

where

$$\hat{\gamma} - 1 = \frac{\hat{R}}{\hat{c}_v^*}, \qquad \hat{R} = \sum_{i=1}^{N} \hat{\rho}_i R_i, \quad \hat{c}_v^* = \sum_{i=1}^{N} \hat{\rho}_i c_{vi}^* \tag{134 i.}$$

and

$$c_{vi}^* = \frac{1}{T} \int_{T_l}^{T_r} \tilde{c}_v^* dT \tag{134 j.}$$

The form of the η-direction inviscid flux vector $\hat{G}$ may be found after the same manner as the ξ-direction flux vector developed above. Utilizing a thin shear layer approximation, the viscous stress tensor $\hat{G}_v$ can be written as

$$\hat{G}_v = \begin{pmatrix} \rho D_{12} c_{1\eta} \\ \rho D_{12} c_{2\eta} \\ \vdots \\ \rho D_{12} c_{N\eta} \\ \mu u_\eta + \frac{1}{3}\mu \tilde{v}_\eta \tilde{\eta}_x \\ \mu v_\eta + \frac{1}{3}\mu \tilde{v}_\eta \tilde{\eta}_y \\ \mu w_\eta + \frac{1}{3}\mu \tilde{v}_\eta \tilde{\eta}_z \\ \rho D_{12} c_{1\eta} e_{n_1} + k_{n_1} T_{1_\eta} \\ \vdots \\ \rho D_{12} c_{1\eta} e_{n_M} + k_{n_M} T_{M_\eta} \\ \Theta_v \end{pmatrix}, \qquad (135 \text{ a.})$$

where

$$\Theta_v = \left[\frac{\mu\left(q^2\right)_\eta}{2} + kT_n + \sum_{j=1}^{M} k_{nj} T_{jn} + \rho \sum_{i=1}^{N} h_i D_{12} c_{i\eta} + \frac{\mu \tilde{v}_\eta \tilde{v}}{3} \right], \qquad (135 \text{ b.})$$

$$q = u^2 + v^2 + w^2, \qquad (135 \text{ c.})$$

and

$$\tilde{v}_\eta \equiv \tilde{\eta}_x u_\eta + \tilde{\eta}_y v_\eta + \tilde{\eta}_z w_\eta. \qquad (135 \text{ d.})$$

MUSCL Extrapolation.

Second-order spatial accuracy in the above scheme is achieved by application of the MUSCL extrapolation (Van Leer, 1979) with a minmod limiter (Yee, 1987). In essence, the MUSCL extrapolation replaces the piecewise constant interpolant with one which is piecewise linear on the solution domain, thus increasing the solution accuracy from first-order to second-order. However, so that the scheme might maintain the property of being total variation diminishing, it is necessary to drop to first-order

accuracy in the immediate vicinity of a flow discontinuity. This limiting procedure is accomplished by application of the minmod flux limiter which is defined by the function

$$\min \mathrm{mod}(x, y) = \mathrm{sgn}(x) \cdot \max\left\{0, \min\left[|x|\right], y \cdot \mathrm{sgn}(x)\right\} \tag{136}$$

One may thus identify the slope of the linear interpolants about the (i+1/2) cell interface by

$$\tilde{\Delta}_{j+\frac{3}{2}} = \min \mathrm{mod}\left(\Delta_{j+\frac{3}{2}}, \Delta_{j+\frac{1}{2}}\right) \tag{137 a.}$$

$$\tilde{\Delta}_{j-\frac{1}{2}} = \min \mathrm{mod}\left(\Delta_{j-\frac{1}{2}}, \Delta_{j+\frac{1}{2}}\right) \tag{137 b.}$$

And finally the cell-center values of the conserved quantities may be extrapolated the left and right sides of the cell interface

$$u^{R}_{j+1/2} = u_{j+\frac{1}{2}} - \frac{1}{2}\tilde{\Delta}_{j+\frac{3}{2}} \tag{138 a.}$$

$$u^{L}_{j+1/2} = u_{j} + \frac{1}{2}\tilde{\Delta}_{j-\frac{1}{2}} \tag{138 b.}$$

Entropy Fix.

In order to eliminate entropy-violating phenomena from the steady-state solution, the entropy correction $\psi(\lambda)$ is applied to the flux scheme. This entropy condition is enforced as in Josyula and Shang (1993), whereby the eigenvalues are cut off according to the relation

$$\psi(\lambda) = \begin{cases} \lambda & |\lambda| \geq \delta_1 \\ \dfrac{\lambda^2 + \delta_1^{\,2}}{2\delta_1} & |\lambda| < \delta_1 \end{cases} \tag{139}$$

The isotropic and anisotropic formulas for determining δ_i are used in the body-normal

$$\delta_n = \delta_1 J^{-1}\left[\left|\mathbf{u}\cdot\nabla\xi\right| + \left|\mathbf{u}\cdot\nabla\eta\right| + \left(a/2\right)\left(\nabla\xi + \nabla\eta\right)\right] \tag{140}$$

and body-tangential directions

$$\delta_t = \delta_1 J^{-1}\left[1 + \left(\frac{\lambda^{(\eta)}}{\lambda^{(\xi)}}\right)^{2/3}\right], \tag{140}$$

where $\lambda^{(k)} = \left|\mathbf{u}\cdot\nabla k\right| + a\left|\nabla k\right|$ and the parameter δ_1 is assigned values of 0.5 and 0.01 in the body-tangential and body-normal directions, respectively.

Predictor-Corrector Method.

Time integration is by the predictor-corrector method of MacCormack (1985). It is second-order and is implemented for the flux-splitting method in these steps:

1) Predictor step

$$\Delta U_{i,j}^{n} = -\Delta t\left(\frac{D_+ F_{i,j}^{n}}{\Delta x} + \frac{D_+ G_{i,j}^{n}}{\Delta y}\right) \tag{141 a.}$$

$$\bar{U}_{i,j}^{n+1} = U_{i,j}^{n} + \Delta U_{i,j}^{n} \tag{141 b.}$$

2) Corrector step

$$\Delta \bar{U}_{i,j}^{n+1} = -\Delta t\left(\frac{D_+ \bar{F}_{i,j}^{n+1}}{\Delta x} + \frac{D_+ \bar{G}_{i,j}^{n}}{\Delta y}\right) \tag{142 a.}$$

$$U_{i,j}^{n+1} = \frac{1}{2}\left\{U_{i,j}^{n} + \bar{U}_{i,j}^{n+1} + \Delta \bar{U}_{i,j}^{n+1}\right\} \tag{142 b.}$$

Boundary Conditions.

The Roe flux-splitting scheme together and the explicit MacCormack predictor-corrector method both allow for the use of explicit boundary conditions. The different boundary and initial conditions are discussed briefly in the following paragraphs. Since the nonequilibrium flow solver is based on the finite volume method, ghost cells are used

to implement the various boundary conditions which follow. The flow solver must be supplied with a grid which has the ghost cells explicitly built into it. Or, said another way, the code treats the cells along the edge of the grid as ghost cells.

When starting the flow solver it is necessary, due to the time-marching nature of the solution method, to provide the code with an initial condition. The flow solver accepts either the solution from a previous run or the following user-specified data through the use of an input file which is read at execution: T_{wall}, M_{ref}, L_{ref}, T_{inf}, and P_{inf}. At the first time step, the entire domain is initialized according to these reference quantities.

Given the ghost cell implementation discussed above, the wall is said to be located at the cell interface between the ghost and first interior cells. As such, the no-slip boundary condition is implemented by ‗cancelling out' the velocity components of the adjacent interior cell such that the vector average at the cell wall is identically zero.

$$u_g = -u_a \tag{143 a.}$$

$$v_g = -v_a \tag{143 b.}$$

The pressure boundary condition at the wall is implemented in a rather straight forward manner by assuming a zero pressure gradient through the boundary layer to the wall. This condition provides a means for specifying pressure in an expedient manner, so long as the boundary layer thickness is much smaller than the radius of curvature of the body (White, 2006).

$$p_g = p_a \tag{144}$$

The isothermal wall boundary condition is implemented by requiring that the flow field temperature at the wall (i.e., first cell interface) be equal to the user-specified wall temperature. This calculation is accomplished by a simple linear extrapolation

$$T_g = 2T_w - T_a \tag{145}$$

The ghost cell values of the species-specific vibrational temperatures and the electron temperature are set according to an assumed quasi-adiabatic condition. This approach is reasonable considering that these modes of energy transfer are much less efficient at removing thermal energy from the wall than collisions with heavy particles. The quasi-adiabatic condition is enforced by setting the ghost cell value equal to the adjacent cell value

$$T_{i,g} = T_{i,a} \tag{146}$$

The final wall boundary condition is a matter of specifying the nature of the chemistry at the wall. A non-catalytic boundary condition is specified at the wall, which assumes that the gradients of the mass fractions are zero at the cell interfaces. This boundary condition yields reasonable results, although it does not account for real surface chemistry effects such as recombination.

The outflow boundary condition is somewhat challenging to implement due to the mixed nature of the solution as it interacts with this boundary. Along this boundary, the velocity goes from zero at the wall, passing through the subsonic range within the boundary layer, to supersonic in the shock layer. In the subsonic region, the solution no longer hyperbolic; rather it is parabolic. That is to say, the solution on the boundary exhibits a certain dependence on the solution within the domain due to solution characteristics capable of propagating upstream. Therefore, it is desirable to split the

boundary condition in terms of the local Mach number. Where the local Mach number is greater than one, it is permissible to simply project the value in the solution domain into the ghost cell by some suitable projection. Conversely, where the local Mach number is less than one, a boundary condition which takes into account the dependence would be utilized. One such boundary condition is the characteristic outflow boundary condition of Hirsch (1987).

According to this approach the values of the flow quantities at the outflow boundary may be set as follows

$$p_b = p_d - \rho_0 a_0 \left(u_d n_x + v_d n_y \right) \tag{147}$$

$$\rho_b = \rho_d - \frac{1}{a_0^2} \left(p_d - p_b \right) \tag{148}$$

and velocity components as

$$u_g = u_a - 2\left(u_d n_x + v_d n_y \right) n_x \tag{149 a.}$$

$$v_g = v_a - 2\left(u_d n_x + v_d n_y \right) n_y \tag{149 a.}$$

where n_x and n_y are the components of the outward-facing normal vector of the boundary cell. The NH7AIR code currently implements the supersonic outflow boundary condition. It was proposed that the outflow boundary condition be improved according to the subsonic implementation discussed above. This implementation was briefly pursued. However, this introduced unexpected numerical instabilities which were not able to be resolved in a timely manner. While the mixed boundary condition would have represented the physical situation more accurately, the original boundary condition was accepted for the sake of moving forward with more central research tasks.

The implementation of the inflow boundary condition is relatively straightforward. Since the governing equation set is hyperbolic in nature ahead of the shock layer, the inflow boundary condition has no dependence on the solution within the domain. As such, it is only required that the values along this boundary (i.e., ghost cell values) be specified as the freestream values.

Grid Adaptation.

There are two regions of great interest in the flow surrounding a reentry vehicle. First, the region near the bow shock is of great importance due to the relaxation processes which occur just downstream of it. These relaxation processes greatly influence the radiative heating predicted by the radiative transport method. The second region of interest is the boundary layer, which is known, of course, to determine the convective heating predicted by the flow solver. Therefore, it is necessary to adapt the grid to adequately compute these and other important quantities. Grid adaptation is accomplished upon initiation of a given calculation session, according to the method of Gnoffo, *et al.,* (1993) and as implemented in the NH7AIR code by Komives and Greendyke (2009; Komives 2009).

The algorithm utilizes four user-specified parameters in order to perform the grid adaptation on the $k \le K$ cell faces in the wall-normal direction. The first such quantity is the cell Reynolds number, $N\,\mathrm{Re}_{cell}$, which determines the first cell size according to

$$\Delta\hat{n}(1) = \frac{N\,\mathrm{Re}_{cell}\,\mu(1)}{\rho(1)\,a(1)\,n^{(1)}(K)} \qquad (150\text{ a.})$$

where

$$N\,\mathrm{Re}_{cell} = \frac{\rho a \Delta n}{\mu} \quad . \tag{150 b.}$$

A few notes are needed here before proceeding. First let $n^{(1)}(k)$ denote the original distance between the body surface and the *k-th* cell center along the coordinate ζ. The value $\hat{n}(k) = n^{(2)}(k)/n^{(1)}(K)$ denotes the nondimensional distance in the ζ direction. Furthermore, let $\Delta\hat{n}(k) = \hat{n}(k+1/2) - \hat{n}(k-1/2)$ define the width of the *k-th* cell with the interpretation that the indices *k+1/2* and *k-1/2* refer to the outer and inner cell edges, respectively. The second parameter, F_{bl}, specifies the fraction of the total number of cells which are placed in the boundary layer by the mapping, $K_{bl} = F_{bl}K$. The following function controls the cell growth in the mapping of cells into the boundary layer

$$\Delta\hat{n}(k) = \left[1 + C\sin\left(\frac{(k-1)\pi}{K_{bl-1}}\right)\right]\Delta\hat{n}(k-1) \tag{151}$$

where

$$C = \left(\frac{F_{bl}}{\Delta\hat{n}(1)}\right)^{\frac{1}{K_{bl}}} - 1 \tag{152}$$

With the cell individual cell widths calculated according to the above expression, the distribution of $\hat{n}$ is obtained *via*

$$n(k+1/2) = \sum_{l=1}^{k} \Delta\hat{n}(l) \tag{153}$$

This transformation provides for gradual cell growth in the boundary layer. This growth slows down as the edge of the boundary layer is approached, such that the remaining cells past $k \geq K_{bl}$ are equally spaced.

The second transformation is designed to resolve the bow shock by grouping cells near the $\hat{n} = F_{sh}$ location. First, a renormalization is preformed to fix range of zeta exactly between zero and one. This normalization is done by dividing each cell face location by the cell face on the outer boundary,

$$\hat{n}\left(k+1/2\right)/\hat{n}\left(K+1/2\right)\longrightarrow\hat{n}\left(k+1/2\right). \tag{154}$$

With the renormalization complete, the transformation is performed according to

$$\hat{n}\left(k+1/2\right)=\left(1-\varepsilon\left(k+1/2\right)\hat{n}\left(k+1/2\right)\right)+F_{sh}\varepsilon\left(k+1/2\right) \tag{155 a.}$$

where

$$\varepsilon\left(k+1/2\right)=\hat{n}^2\left(k+1/2\right)\left(1-\hat{n}\left(k+1/2\right)\right)\varepsilon_0 \tag{155 b.}$$

This expression introduces the fourth user-specified parameter, ε_0, which controls how tightly the cells are group about the shock. This parameter must be chosen with care to ensure that the grid does note fold back onto itself near the shock.

The final transformation returns the distribution of cell centers in the original dimensions of the grid. A scaling factor is used to ensure that the captured shock lies at the specified fraction F_{sh} of the distance between the body and the outer boundary. This transformation is performed according to

$$n^{(2)}\left(k\right)=\frac{n^{(1)}\left(*\right)\hat{n}\left(k\right)}{F_{sh}} \tag{156}$$

where $n^{(1)}\left(*\right)$ is the location on the original grid where the captured shock is first sensed. Finally, interpolation and extrapolation are used to map all the old grid points $\vec{x}\left(n_{i,j}^{(1)}\left(k+1/2\right)\right)$ into the new grid $\vec{x}\left(n_{i,j}^{(2)}\left(k+1/2\right)\right)$.

Radiation Transport Solution Procedure

Two methods of solving the radiative transport equation were developed and used to obtain results in this research. The tangent slab method, discussed in the previous chapter, was used to obtain radiative solutions both coupled and uncoupled with the nonequilibrium flow solver. The results obtained by the finite volume method for radiative transport were so obtained in an uncoupled fashion but utilizing the coupled flow fields resulting from coupling the two-flux method with the nonequilibrium flow solver.

Tangent Slab Method.

The implementation of the tangent slab method within the context of a reentry shock layer is rather straightforward and is a stardard part of spectroscopic codes like SPRADIAN. The expression presented in equation (119) may be easily evaluated in a marching fashion toward and away from the body. With the radiative intensities thus obtained, the radiative source terms may be evaluated and coupled with the nonequilibrium solver as discussed in the following section.

Finite Volume Method.

The finite volume method of radiative transport (FVMR) is based on the conservation relation for radiative energy given in Chapter III, and its development for use in the axisymmetric flowfield, as part the present research effort, is a unique feature of this work.

$$\int_{\Omega_i}\int_{\Gamma} I_\nu \left(\hat{s}\cdot\hat{n}\right) d\Gamma d\Omega = \int_{\Omega_i}\int_{V} \left(\varepsilon_\nu - \kappa'_\nu I_\nu\right) dV d\Omega \tag{157}$$

Assuming that intensity is constant across a given face of the element, as well as over the solid angle Ω_i, in the *i-th* direction, the foregoing conservation equation can be restated in the discretized form

$$\sum_k I_{\nu ki}\left(\vec{s}_i \cdot \hat{n}_k\right) A_k = \left(\varepsilon_\nu - \kappa_\nu {}' I_{\nu pi}\right) V \Omega_i \qquad \text{(158 a.)}$$

where

$$\vec{s}_i = \int_{\Omega_i} \hat{s} d\Omega \qquad \text{(158 b.)}$$

In the above expressions, the unit normal vector and area associated with the *k-th* cell face are given by $\hat{n}_k$ and A_k, and the unit normal vector and total solid angle vector associated with the *i-th* direction are given by $\hat{s}$ and $\vec{s}_i$. Figure 1 illustrates the method by which the foregoing unit vectors are assigned to the spatial and directional discretization schemes. The intensities at the face centers I_{ki} are related to those at the volume centers according to the step scheme where a positive or negative dot product $\left(\vec{s}_i \cdot \hat{n}_k\right)$ indicates a flux out of or into a cell, respectively. First, it is assumed that for intensities leaving the control volume *P* the intensity at the *k-th* face is equal that of the subject volume's cell-center intensity I_{pi} in the *i* direction. Then for intensities entering the subject volume it is possible to take I_{ki} to equal the I_{pi} of the appropriate neighboring cell.

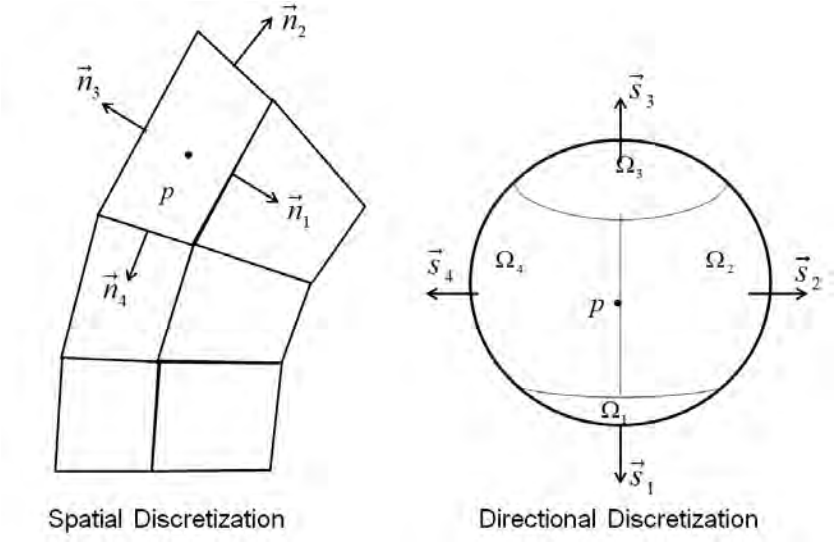

Figure 1. Spatial and Directional Discretization for Finite Volume Method for Radiation

With the spatial and directional domains specified as above, it is possible to make the appropriate substitutions, and thus solve for the cell-center intensities I_{pi} explicitly in terms of the neighboring-cell intensities $I_{k\mathrm{i}}$.

$$I_{\nu pi} = \frac{\varepsilon_\nu V \Omega_i - \sum_{k,in} I_{\nu ki} \left(\vec{s}_i \cdot \hat{n}_k \right) A_k}{\sum_{k,out} \left(\vec{s}_i \cdot \hat{n}_k \right) A_k - \kappa_\nu ' V \Omega_i} \tag{159}$$

Finally, the incidence radiation and radiative flux are calculated according to

$$G_{\nu p} = \sum_i I_{\nu ip} \Omega_i \tag{160 a.}$$

and

$$\vec{q}_{\nu p} = \sum_i I_{\nu ip} \vec{s}_i \tag{160 b.}$$

Suitable boundary conditions for the radiative transport equation can be easily obtained in a similar manner and are stated here, where ~~"s~~" a surface quantity.

$$\vec{q}_{\nu p} = \varepsilon_{\mathrm{s}} \left(I_{bs} \sum_{i,out} \vec{s}_i \cdot \hat{n}_s - \sum_{i,out} I_{si} \left| \vec{s}_i \cdot \hat{n}_s \right| \right) \tag{161}$$

Numerical Solver Details.

Given the form of equation (159), it is possible to solve for the cell-center intensities I_{vpi} utilizing one of two methods. The first method would be to obtain a solution iteratively, by guessing an initial solution for center intensities I_{vpi}. Using this initial guess, the solution is marched forward using the cell-centered intensities I_{vpi} at each $(n-1)th$ step to approximate the cell-neighbor intensities I_{vki} at the nth step and thus obtain the updated cell-center intensities. This process continues until the solution reaches an acceptable level of convergence.

A second method would be to solve the linear system of equations created by expressing equation (159) in matrix form. Where the cell-center intensities I_{vpi} are now considered as $I_{v(I,J)i}$, the intensity at grid point (I,J), and the neighbor-cell intensities I_{vki} are taken at the neighboring grid points $(I+1,J),\ (I-1,J),\ (I,J+1),\ and\ (I,J-1)$. This scheme results in the banded linear system with diagonal sub-matrices defined as follows

$$\begin{bmatrix} \ddots & & & & & \cdots & 0 \\ & \ddots & & & & & \vdots \\ & & \ddots & & & & \\ F^i_{I,J-1} & \cdots & F^i_{I-1,J} & F^i_{I,J}+\kappa' V_{I,J}\Omega_i & F^i_{I+1,J} & \cdots & F^i_{I,J+1} \\ & & & & \ddots & & \\ \vdots & & & & & \ddots & \\ 0 & \cdots & & & & & \ddots \end{bmatrix}_v \begin{bmatrix} I^i_{I,J-1} \\ \vdots \\ I^i_{I-1,J} \\ I^i_{I,J} \\ I^i_{I+1,J} \\ \vdots \\ I^i_{I,J+1} \end{bmatrix}_v = \begin{bmatrix} \vdots \\ \vdots \\ \vdots \\ \varepsilon V_{I,J}\Omega_i \\ \vdots \\ \vdots \\ \vdots \end{bmatrix}_v \qquad (162\text{ a.})$$

$$F^i_{k\neq IJ} = \begin{cases} \left(\hat{n}_k \bullet \vec{s}_i\right),\ if < 0 \\ 0 \end{cases} \qquad (162\text{ b.})$$

$$F^i_{IJ} = \sum_{k,if>0} \left(\hat{n}_k \bullet \vec{s}_i\right) \qquad (162\text{ c.})$$

This system has a bandwidth which corresponds to the number of J grid points in each grid row I. The elements F_k^i correspond to the inner product of the area normal vector $\hat{n}_k$ with the transmission direction vector $\vec{s}_i$, where $F_{I,J}$ is calculated based on the outgoing radiation and all off-diagonal F_k^i elements are based on the incoming radiation. The solver used in this code utilized Gaussian elimination with pivoting to improve numerical stability.

Additional Geometrical Considerations.

One of the additional considerations for implementing the present transport scheme is the method by which the cell-center field of view is discretized by specification of both the magnitude and direction of the differential solid angle Ω_i. For the purposes of this dissertation, the following assumptions have been made regarding Ω_i.

1. Each differential solid angle Ω_i is defined by a vector $\vec{s}_i$ which specifies its orientation and angular extent.

2. Each $\vec{s}_i$ occurs at the centroid of the differential solid angle

3. Each Ω_i consists of a continuous, ~~"re~~gular" solid angle

4. The topology of Ω_i upon the unit sphere is such the distance between the edge $d\Omega_i$ and the centroid of Ω_i is minimized.

5. Each Ω_i contributes $4\pi / N$ steradians to the total FOV, where N is the number of differential solid angles.

6. The FOV should be such that the resulting $\vec{s}_i$'s are spaced at regular intervals within the FOV

Generally speaking, the finite volume method radiative transport scheme poses no restriction on the number of transmission direction which may be considered. For the purposes of this dissertation, six transmissions have been considered—one each in the positive and negative z, r and θ directions. This is the minimum number needed to investigate possible 3D effects. This selection of transmission directions is also advantageous for comparisons with experimental data which are most often collected at orientations which are normal to coordinate system basis vectors.

One particularly challenging aspect of implementing the FVMR scheme in an axisymmetric coordinate system is related to propagating the solution across the grid singularity created by line of symmetry. The problem lies in two areas. First, there is a geometric constriction/relief effect in the r-direction and second, the simulation of adjacent neighbor cells in the θ direction. Because of symmetry, it is desirable to compute the solution on a wedge-shaped region of the total flow field. Therefore, the r-direction faces become increasingly small and vanish as the centerline is approached. Conversely, the r-direction faces become increasingly large moving away from the centerline. Here the difficulty becomes apparent as two geometric effects begin to influence the solution. Fluxes which approach the singularity are constricted. Because the FVMR conserves radiative energy, the intensity exiting through the shrinking r-faces will become increasingly large and even become unbounded at the singularity. As fluxes depart from the centerline, there is a geometric dissipation effect.

The contribution of radiative flux from these adjacent cells is approximated by assuming that the local intensity at the θ-direction cell face is equal to the intensity at IJ cell center and acting through the projection of the θ faces onto the r-z plane. However,

a straightforward application of the step scheme above would not work here since the neighboring cells in the θ direction are by symmetry the same as the cell under consideration. Considering the negative *r* transmission direction first, it is noted that the dot product of the negative *r*-direction unit vector with the unit vector of the θ faces $\left(\vec{s}_{r-}\cdot\hat{n}_{\theta}\right)$ is negative, and, therefore, the associated $F_{I,J}$ matrix element in equation (162) preserves the sign convention already establish by the step scheme. However, the situation is more difficult in the positive-r transmission direction first. In this case, the dot product $\left(\vec{s}_{r+}\cdot\hat{n}_{\theta}\right)<0$, and so there is an influx of radiative flux from the *IJ* cell center.

Unfortunately, it would violate the sign convention of the step scheme to assign a negative value of $F_{I,J}$ to the *IJ* diagonal. Thus, the following alternative approach is proposed. The approach begins with the observation that the on-diagonal elements of equation (162) consist of two terms: the cell-face view factor $F_{I,J}$ and the cell-center value of absorption $\kappa' V_{I,J}\Omega$. Furthermore, it is required that under the step scheme $F_{I,J}>0$ and generally $\kappa' V_{I,J}\Omega>0$. While it is not permissible to assign the negative value $\left(\vec{s}_{r+}\cdot\hat{n}_{\theta}\right)<0$ to the on diagonal view factor $F_{I,J}$, it is permissible to interpret this incoming radiative flux as a being a contribution to the absorption expressed by the term $\kappa' V_{I,J}\Omega$. Thus, it proposed to model this absorption *via* a geometric absorption term which is equal in magnitude and opposite in sign to $\left(\vec{s}_{r+}\cdot\hat{n}_{\theta}\right)$.

Further difficulty arises in the case of radiative fluxes in the θ direction due to the fact that only a one cell wide, wedge-shaped region of the flow field is modeled. Given the above considerations, future implementation of the FVMR scheme should avoid an

axisymmetric grid implementation such as the one described, in favor of a full 3D grid with no singularity.

Radiative-Gasdynamic Coupling

In this section a suitable coupling scheme between the radiation and gasdynamic solutions is developed. Pai (1966) offers a complete treatment of fully-coupled radiation-gasdynamic system; however, a loosely-coupled scheme is used. In such a scheme, radiation-related source terms are static (or ramped) over several iterations of the flow solver and updated according to user-specified criteria, such as order of convergence or number of iterations. This approach is allowable since time-accurate simulations are not being pursued. However, under this approach, convergence is not guaranteed and solutions may not necessarily be unique. Given the very stiff nature of the radiation terms, numerical challenges are likely to be encountered in such a coupled situation, especially when using shock-capturing techniques (Gnoffo, *et al.*, 2009).

The additional consideration of radiation in a flowfield requires the tracking of a new energy transfer mechanism, namely that energy which is transported through the solution domain due to radiation. In order to have a coupled scheme, that energy must show up in the flowfield equations. In practice, one is interested in the total radiative source term in addition to the radiation-electronic energy source term and radiation-species vibrational energy source terms, since these are the ones which are needed to couple the radiation transport and nonequilibrium flow solver codes.

Recalling the conservation relation for radiative energy, the total amount energy lost from the flow field due to radiation may be computed by integrating the divergence of the spectral intensity

$$\dot{Q}_{total} = \int_{\Omega_i} \int_{\Gamma} \int_{\nu} \left(\nabla \cdot \mathbf{I}_{\nu} \right) d\boldsymbol{\Gamma} d\boldsymbol{\Omega} \tag{163}$$

Alternately, the net emission may be integrated

$$\dot{Q}_{total} = \int_{\Omega} \int_{V} \int_{0}^{\infty} \left(\varepsilon_{\nu} - \kappa_{\nu}' \mathbf{I} \right) d\nu dV d\boldsymbol{\Omega} \tag{164}$$

This energy represents the difference between emitted and absorbed radiation. Thus, if the fluid emits more radiation than it absorbs, then the energy is lost in a phenomena known as "radiation cooling". Conversely, the fluid may be heated by absorbing radiation. In many situations, the absorption of radiation is considered to be negligible, relative to other effects. When this is the case, the media is said to be optically thin, and it is possible to evaluate the source term solely in terms of the emission coefficient *via* the simple algebraic formula

$$\dot{Q}_{total} = 4\pi \varepsilon_{\nu} V \tag{165}$$

Coupling with the vibrational energy equation occurs through the radiative species-vibrational source terms

$$\dot{Q}_{vib,s} = \int_{\Omega} \int_{V} \int_{0}^{\infty} \alpha_{\nu,s} \left(\varepsilon_{\nu,s} - \kappa_{\nu,s}' \mathbf{I}_{\nu,s} \right) d\nu dV d\boldsymbol{\Omega} \tag{166}$$

where $\varepsilon_{\nu,s}$ and $\kappa'_{\nu,s}$ denote the contribution of species s to the emission and absorption coefficients and $\alpha_{\nu,s}$ represents proportion of energy which is responsible for exciting or damping. This calculation may be accomplished by considering the separability of internal energy, whereby a portion of the energy $h\nu$ contained in the emitted/absorbed photons can be attributed to the change in vibrational energy resulting from a given

transition. Consider that the energy at a particular energy level which is the sum of the electronic, vibrational and rotational terms as shown

$$E(e,v,J) = T_e + G_v + F_J \,. \tag{167}$$

Thus the energy which must emitted or absorbed by a photon in order to undergo a state transition is given as

$$h\nu = \Delta E = (T_{e'} - T_e) + (G_{v'} - G_v) + (F_{J'} - F_J) \,. \tag{168}$$

It then follows that the proportion of that energy which contributes to the excitation of the vibrational mode is given as

$$\alpha_{vib} = \frac{(G_{v'} - G_v)}{(T_{e'} - T_e) + (G_{v'} - G_v) + (F_{J'} - F_J)} \tag{169}$$

V. Computer Implementation

Having discussed the necessary background theory and various methodological aspects of this research effort in the previous two chapters, the present chapter outlines how these concepts have been implemented in a computer code. In the course of outlining this implementation process, the basic structure and function of the two baseline codes are discussed, and the manner in which they have been modified and coupled is explained. The basic flow of the resulting computer program is illustrated below in Figure 2.

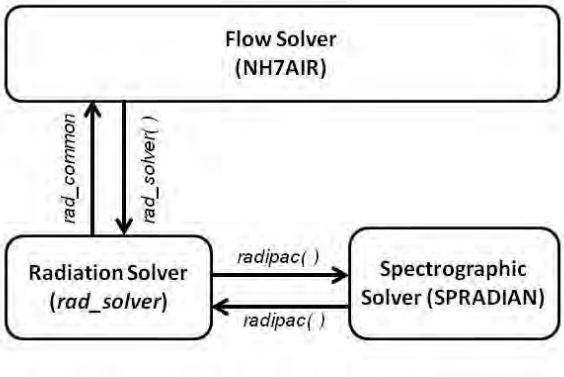

Figure 2. Flowchart for Overall Computer Program

This chapter is organized into three sections: two sections correspond to the modifications made to the baseline flow field and spectroscopic solvers, NH7AIR and SPRADIAN, respectively, and another section which follows the development of a radiation solver which calculates the solution to the radiative transport equation and handles the passage of data between the flow solver and spectroscopic code. The various elements of the computer program are listed below in Table 2.

Table 2. Summary of Computer Program Elements; *highlighting indicates those aspects of the computer code which have been modified.*

Flow Solver (NH7AIR)	Radiation Solver	Spectroscopic Solver (SPRADIAN)
subroutine a360	module rad_parameters	module size_def_mod
subroutine alignshock	module rad_vars	module struct_def_mod
subroutine bc	subroutine rad_solver	module interface_mod
subroutine const	subroutine rad_TS	subroutine radipac
subroutine cvmgp	subroutine rad_FVM	subroutine emis_absb
subroutine datin	subroutine rad_couple	subroutine atom_bb
subroutine estdt	subroutine simpson	subroutine atom_bf
subroutine fsiroe	rad_comon	subroutine atom_ff
subroutine fsjroe	rad_parameters	subroutine atom_noneq
subroutine gcomon	rad_solver90	subroutine diatom_bb
subroutine gmtry	radipac6X90	subroutine calc_diatom_dist
subroutine gridin		subroutine calc_diatomic_bb
subroutine hisstr		subroutine diat_eimp_exct
subroutine iviscrg		subroutine cros_ab
subroutine jviscrg		subroutine diatom_noneq
subroutine l		subroutine diatom_read
subroutine lmitri		subroutine H_bb
subroutine lmitrj		subroutine intpl1
program main		subroutine minv
subroutine p3dwr		subroutine monatom_read
subroutine parse		subroutine simp
subroutine plotc		subroutine taint
subroutine sourcet		subroutine tri_cont
subroutine stvar		subroutine triatom_read
subroutine transp		subroutine vuv_bf
subroutine vtkio		
subroutine wrstte		
subroutine wrtout		

Flow Solver

The discussion of the major segments of the developed computer code begins with the nonequilibrium flow solver NH7AIR, since this portion of the code most directly controls the overall execution of the program. From the perspective of the solution methodology, this aspect of the resulting code is not surprising. Consider the nature of the coupling between the flow field and the radiative solutions. At the length and time

scales involved when considering reentry situations, the radiation solution exhibits an elliptic behavior in the solution domain. Furthermore, the radiation solution may be assumed to update _instantly' to new flow field conditions; whereas several iterations of the flow solver are required to allow the flow field to adjust to new radiative source terms. The computer code which results from this methodology is one wherein the radiation solver and spectroscopic solver function as subroutines which are periodically called by the main program—the flow solver—in order to update the radiative source terms. A brief description of the most significant aspects of the baseline flow solver follows in order to facilitate the subsequent discussion of modifications made thereto. Figure 3 contains a flow chart which illustrates the logical arrangement of the most important subroutines in the flow solver.

The main program is contained in the Fortran file so named *main.f*. As is customary, the main program coordinates the execution of the overall computer code by performing the primary input/output functions and calling the various subroutines contained in the program. The subroutine *datin* is the first called and is responsible for reading the input deck and the restart files, consisting of a grid and solution files from previous runs. Initial and boundary conditions are supplied by the subroutine *bc,* which is called at restart and at each time step. The main program loop consists of calls to the subroutines indicated in Figure 3.

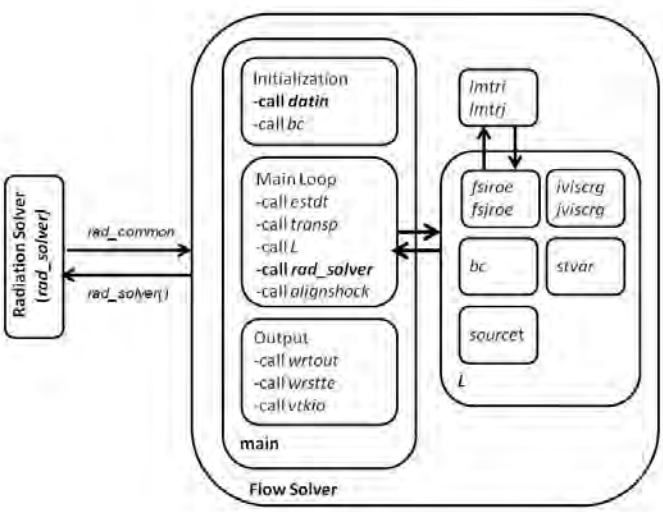

Figure 3. Flowchart for Nonequilibrium Flow Solver (NH7AIR)**;** *bold indicates areas of the code affected by modifications.*

Most of the subroutines listed in the main loop have names which suggest the function(s) they perform. The subroutine *estdt* estimates the local time step based on the CFL criteria specified by the input file. Transport coefficients for heat transfer and viscosity are calculated by *transp.* The subroutine *L* has a rather opaque name yet is critically important. This subroutine accomplishes the time-integration of the solution and performs calls to several other supporting subroutines. The calculation of convective fluxes, *via* the Roe-averaging method discussed in the previous chapter, is performed by *fsiroe* and *fsjroe,* where the subroutines *lmtri* and *limtrj* implement a minmod limiter as described previously. Calculation of the viscous fluxes is performed by *iviscrg* and *jviscrg.* Subroutine *stvar* backs out the state variables from the vector of conserved quantities and *sourcet* calculates the various source terms used in *L* to update the flow field solution. Finally, various subroutines write restart files and desired output files.

Modifications.

The modifications made to the baseline flow solver were primarily concerned with input/output functions, the passage of data between the flow and radiation solvers, and the introduction of radiative source terms into the flow solver. Listings of these modifications may be found in Appendix A and are summarized below in Table 3.

Table 3. Summary of Modifications Made to Baseline Flow Solver.

Description	Subroutine	Appendix Entry
Changes to input file	*datain*	Table 11
Radiation restart (Read)	*datain*	
Call radiation solver	*main*	Table 12
New output files	*main*	
Modifications to vtk output	*vtkio*	
Radiation restart (Write)	*wrtout*	

Here follows a brief discussion of these modifications. The first set of modifications affect the subroutine *datain,* wherein additional read statements were needed in order to input solution parameters associated with the setup and execution of the radiation solver. This subroutine was further modified in order to read radiation restart data into the program. Radiation restart files are written by statements added to the subroutine *wrtout*. In addition, various modifications were made to *main* and the subroutine *vtkio* in order to output quantities of interest associated with the radiation solution. The most significant modifications were to add a call to the radiation solver in the main loop and to update the source terms in order to account for the effects of radiation. These modifications were made to the main program and to the subroutine *sourcet*.

Radiation Solver

The discussion of the implementation effort now turns to the development of the radiation solver, which is responsible for solving the radiative transport equation (RTE) and updating the radiative source terms in the energy conservation equations of the flow solver. The radiation solver is called from within the main loop of the flow solver and thus is subordinate in program hierarchy to the flow solver. The sequence of the subroutine components (and their interaction with program segments outside of the radiation solver) is illustrated below in Figure 4.

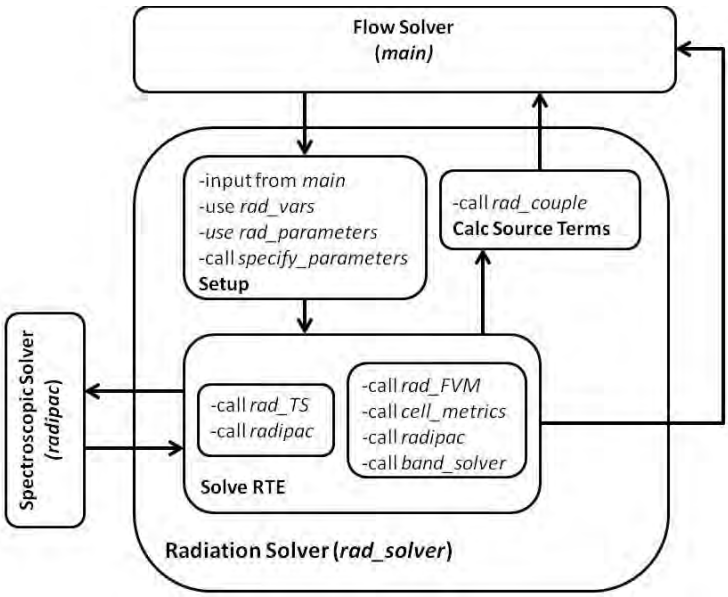

Figure 4. Flowchart for Radiation Solver (*rad_solver*)

As illustrated in the preceding flowchart, the execution of the radiation solver subroutine consists in the sequential performance of the following functions: setup, solve RTE, and calculate source terms. This functional delineation provides a convenient framework for discussing the subcomponents of the radiation solver.

The first function to be performed is to setup the radiation solver in terms of various user-specified parameters and flow field variables—all of which are passed by the main program as arguments to the subroutine *rad_solver*. Receiving these values from the main program, the remainder of the setup function is carried out by the modules *rad_vars* and *rad_parameters* and by the subroutine *specify_parameters*. The module *rad_vars* declares a variety of variables which are shared by the local subroutines contained in *rad_solver* and used in the calculation of the radiative intensities and source terms. Similarly, the module *rad_parameter* declares various parameters associated the solution procedure; most importantly, it assigns character strings to the arrays which identify the various radiative mechanisms used in both the solution of the radiative transport solution procedure and by the spectroscopic solver. The subroutine *specify_parameters* determines the number of active radiative mechanisms and parses the above string arrays in order to make them more amenable to the format of the data structures in the subroutine *rad_solver*.

Subsequent to the setup of the radiation solver, the subroutine *rad_solver* calls one of two subroutines in order to solve the radiative transport equations: *rad_TS* or *rad_FVM*. These two subroutines are addressed now in turn. The first subroutine, *rad_TS*, calculates the body-normal components of the radiative intensity in the forward and reverse directions. The general flow of this subroutine is summarized below in narrative and also in the pseudo-code provided Tables 17-22 of Appendix A. Upon declaring and initializing variables which are local to *rad_TS*, a set of nested loops is executed in order to calculate radiative intensity. The outermost loop advances the solution procedure from one body-normal path to the next. At the next level down, the

second loop selects the direction of integration—namely, the forward and reverse directions along the path specified by the outer loop. The inner loop advances the solution from one point to another along the integration path and in the direction specified in the outer two loops. At each point along the integration path, it is necessary to obtain the values of the spectral emission and absorption coefficients from the spectroscopic subroutine *radipac*, and then to obtain the radiative intensity from the tangent slab solution to the radiative transport equation. Note that the calculation of the emission and absorption coefficients is relatively expensive and is only performed only once at each point in the flow domain for a given iteration of the radiation solver. Finally, the radiative source terms are calculated from the local emission, taking into account the absorption of radiation from the two transmission directions considered.

The second subroutine, *rad_FVM*, calculates the components of the radiative intensity in the positive and negative coordinate directions of a cylindrical coordinate system aligned with the centerline of the flow field. These directions were chosen for convenience. The general flow of *rad_FVM* is summarized below in narrative and also in the pseudo-code provided Tables 23-27 of Appendix A. As before, the subroutine begins by declaring and initializing the local variables needed by *rad_FVM*. The next step is to calculate the emission and absorption coefficients. The procedure for solving the radiative transport equation is fundamentally different for the FVMR scheme and the tangent slab method. Whereas the tangent slab solution procedure utilizes an analytical approximation in a local integration, the FVMR solves the radiative transport equation over the entire problem domain by inverting a linear system formed in the manner described in the previous chapter. This linear system is constructed once for each

radiative mechanism considered and for each transmission direction considered. For instance, if three radiative mechanisms and three transmissions directions were consider, the linear system would be constructed a total nine times. Note that the coefficients of the LHS matrix and the RHS vector of source terms do vary with these different realizations of the linear system according to the mechanism-specific emission and absorption data, as well as the different direction cosines formed between the selected transmission directions and the cell face within the discretized domain. The reader is directed to the provided pseudo-code for details related to the construction of the linear system described above.

While the radiative source terms are calculate during the execution of *rad_TS* and *rad_FVM,* they are not in a form which is suitable for use in the flow solver. The source terms are thus made suitable for this use by the subroutine *rad_couple*. Finally, these source terms are stored in the common block *rad_common* and passed into the main program where they are utilized in the subroutine *sourcet*. Since radiative intensity is also a quantity of interest, it is passed into the main program and subsequently written to an output file. Unlike the two other sections of this chapter, which pertain to the flow and spectroscopic solvers, this section contains no discussion of modifications to a baseline code. The reason is that the programming of the various subcomponents of the radiation solver resulted from work conducted under the reported research activity. A summary of these programming activities is provided below in Table 4.

Table 4. Summary of Code Development Activities pertaining to Radiation Solver.

Description	Subroutine	Appendix Entries
Common Block	*rad_common*	Table 14
Specify rad parameters	*rad_parameters*	Table 15
Subroutine execution	*rad_solver*	Table 16
Tangent Slab Solver	*rad_TS*	Tables 17-22
FVM Solver	*rad_FVM*	Tables 23-26
Banded Linear Solver	*band*	Table 27
Calculate source terms	*rad_coupled*	Table 28

Spectroscopic Solver

As challenging as the coupling of the flowfield and radiation solutions may be, the tasks performed by the spectroscopic solver SPRADIAN, as implemented in the subroutine *radipac*, are critical to the accuracy of the results which are obtained by the overall solution method. The primary task is the calculation of the spectral emission and absorption coefficients. This task is supported by the secondary tasks of calculating the state populations of the atomic and diatomic systems, together with the calculation of the transition probabilities, line profiles and line strengths associated with each transition. Figure 5 below illustrates the basic structure of the *radipac.*

The execution of *radipac* begins with the passage of values into the subroutine‘s arguments from *rad_solver*. Setup of the spectroscopic solver is accomplished with these passed values and the various modules *interface_mod, structure_def_mod, size_def_mod*. At this point it, it is worth noting that SPRADIAN is a rather extensive code and significant portions of it are not needed in the present implementation. Therefore, only those subroutines which have been utilized and modified will be discussed. Figure 5 below illustrates the program flow for the utilized components of SPRADIAN.

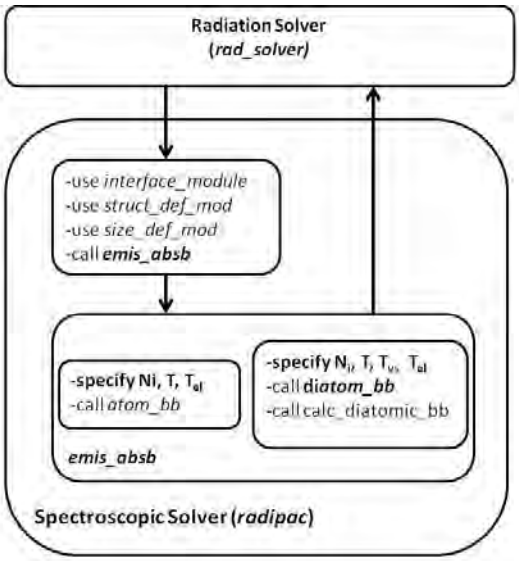

Figure 5. Flowchart for Spectroscopic Solver (SPRADIAN); *bold indicates areas of the code affected by modifications.*

The subroutine *emis_absb* is primarily responsible for coordinating the execution of the various subroutines which are called in order to calculate the emission and absorption coefficients. The first such subroutine is *atom_bb* which calculates these spectroscopic coefficients based upon the calculated number density of the internal electronic states of atomic species and tabulated spectroscopic data, such as transition probabilities. The second subroutine is *diatom_bb*; *it* calculates the spectroscopic coefficients based upon similar calculations but with a few key differences. The most significant difference arises from the necessity of considering transitions between electronic, vibrational and rotational levels within the diatomic species. These transition probabilities are calculated based upon the theoretical developments presented in Chapter III regarding bound-bound radiation in diatomic systems.

Modifications.

The modifications made to the baseline spectroscopic solver, SPRADIAN, were primarily concerned with passing data between *radipac* and *rad_solver* and with parsing the total emission and absorption coefficients into their spectral components by mechanism. Listings of these modifications may be found in Appendix A and are summarized below in Table 5.

Table 5. Summary of Modifications Pertaining to Spectroscopic Solver.

Description	Subroutine	Appendix Entries
Assign common variables	*radipac*	Table 29
Extract state populations	*radipac*	Table 30
Specify Tvibs; added logic	*emis_absb*	Table 31
Spectral emis and absb	*atom_bb*	Table 32
Spectral emis and absb	*diatom_bb*	Table 33

VI. Results

The results presented in this chapter are organized into four sections consisting of one section discussing the solution parameters as taken from the conditions of the FIRE II flight experiment and three sections corresponding to the phases of work conducted. The first of these three remaining sections details the comparison of the multispecies multitemperature and two-temperature thermal model. The comparison was conducted by examining the flow fields obtained by NH7AIR and the two-temperature flow solver LAURA. Both codes use the same air chemistry model and thermophysical data. So, any differences observed in both the flow field and the uncoupled tangent slab radiation results are due to the manner in which internal energy is distributed among the available modes.

The second phase of work includes results obtained by coupling NH7AIR and SPRADIAN with tangent slab radiative transport. A comparison of these coupled results with uncoupled NH7AIR results was conducted in order to investigate the effects of coupling the radiation source terms into the flow solver. The effects on the radiation solution observed are also reported.

The third phase work corresponds to the development of a finite volume method for radiative transport. Spectrally coarse results for three uncoupled cases are examined in this final section,

and some of the geometrical effects of the current implementation are discussed.

The FIRE II Flight Experiment

Data from the FIRE II flight experiment have been used to validate the code developed in the research activities associated with this dissertation. This flight experiment was undertaken by NASA prior to the Apollo missions to investigate the heating environment surrounding vehicles reentering the Earth‘s atmosphere. Of particular interest to this test program was the characterization of the radiance and heat transfer rates on large-scale blunt-nosed bodies. The resulting data was intended for comparison with ground-based experiments and theoretical calculations (Lewis and Scallion, 1965).

The spacecraft configuration shown in Figure 6 included three total radiometers (one on-axis, one off-axis and one aft facing) as well as a spectral radiometer which was bore sighted with the on-axis total radiometer. Additionally, a calorimeter monitored the total heat load on the forebody. The original data collection and reduction plan anticipated that it would be possible to determine the convective heat load by subtracting the radiative heat flux measured by the total radiometer from the total heat flux measured by the calorimeter. Figure 7 illustrate the various phases of the flight experiment.

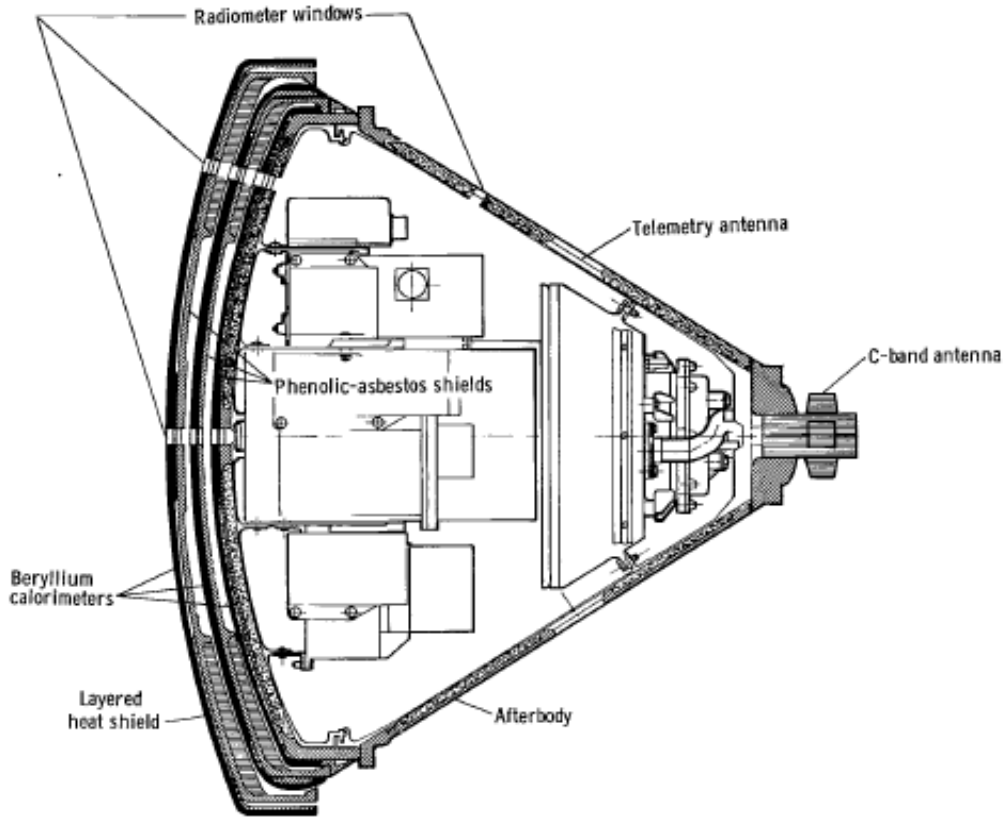

Figure 6. FIRE II Flight Vehicle

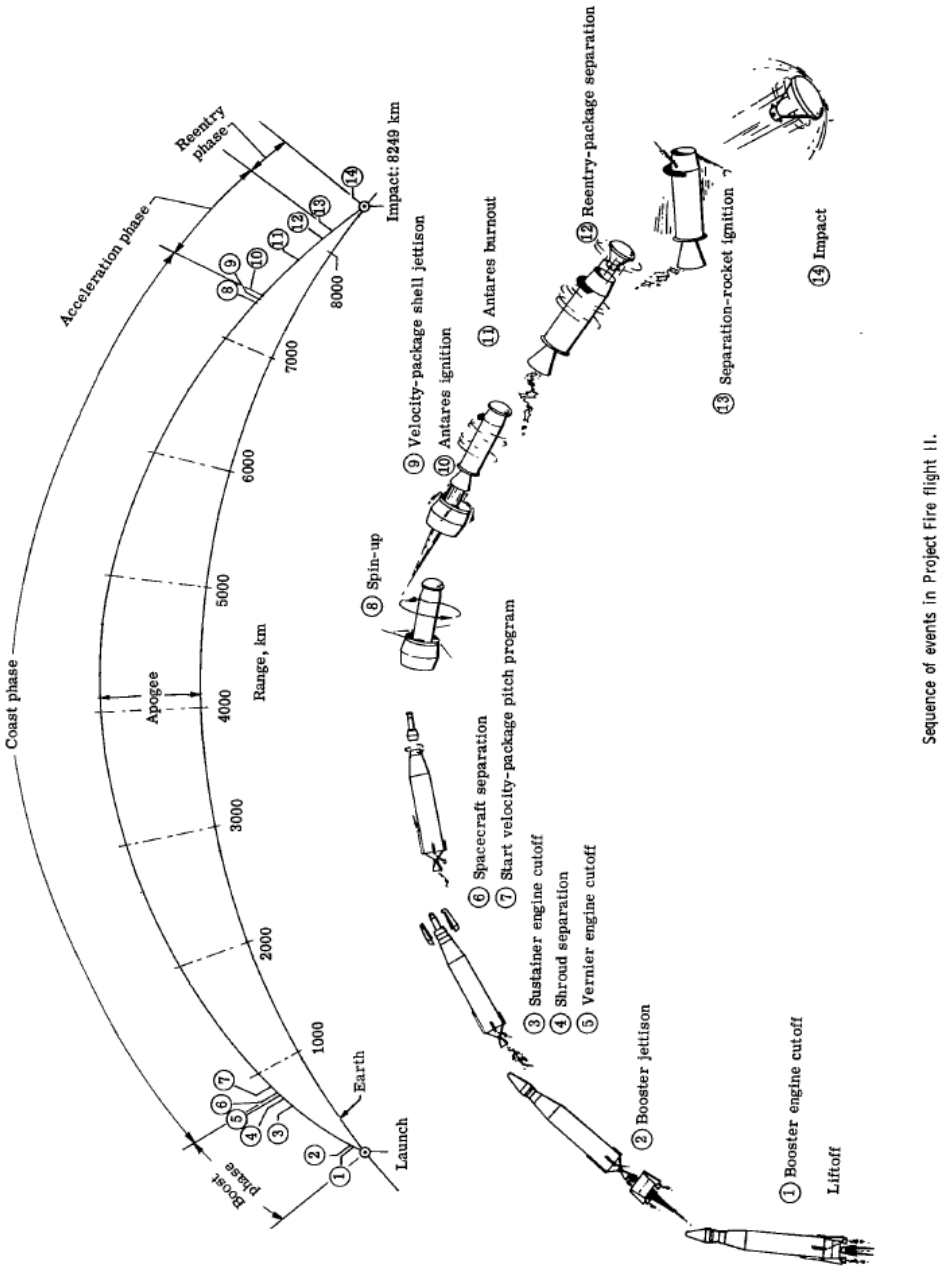

Figure 7. Mission Profile for the FIRE II Experiment

This was all based on the assumption that most of the radiation emitted in the shock layer would be above the optical cutoff of the radiometer window $\lambda > 2,000\text{Å}$. However, it was inferred from the subsequent analysis of the data collected by the total radiometers and calorimeter that strong vacuum-ultraviolet (VUV) sources were present in the flow field. Besides the presence of strong VUV absorption, it was determined that the primary source of radiative emissions were from the near-infrared lines of the atomic flow species.

The reentry of the flight trajectory consisted of three distinct phases, each of which corresponds to the ejection of one of the layered heat shields depicted in Figure 5. The first phase occurred prior to the ejection of the first heat shield beginning at a total elapsed time of 1631.3 seconds and ending at 1636.5. During this first period the flow exhibits a range of equilibrium conditions. The flow starts this experimental period in a state of severe nonequilibrium and by its conclusion has reached as state of near equilibrium. This range of equilibrium conditions makes this an ideal data set for validating a code like the one developed here.

Solution Parameters

The radiation along the stagnation line of the 1634, 1636, and 1640.5-second trajectory points of the FIRE II experiment have been investigated. These trajectory points were selected because of the range of nonequilibrium conditions exhibited: from highly nonequilibrium for the 1634-second point to near equilibrium for the 1640.5-second point. Table 6 below contains the solution parameters at these trajectory points. The freestream chemical composition is given in terms of mass fractions in Table 7. The wall chemistry was modeled using a non-catalytic boundary condition. The grids used in

this study both contained 51x61 nodes in the rotated plane of the axisymmetric body. The grid adaptation algorithm of Gnoffo, *et al.*, (1993) was used to place adequate points in the boundary layer and through the shock in order to adequately resolve the gradients there. A typical grid relative to the FIRE II vehicle is shown below in Figure 8.

Table 6. Parameters for Flowfield Solution

	Flow Field Parameters				
$t_{elapsed}$ (s)	T_{wall} (K)	T_{inf} (K)	M	Re	P_{inf} (Pa)
1634.0	615	195	40.6	1.40E+09	2.08
1636.0	810	210	38.9	1.20E+09	5.16
1640.5	1560	254	34.4	8.50E+08	28.12
	Free Stream Mass Fractions				
$t_{elapsed}$ (s)	c_{N2}	c_{O2}	c_N	c_O	$c_{NO,NO+}$
All	0.767	0.233	1.00E-06	1.00E-06	1.00E-06
			NH7AIR Grid Dim:		51x61

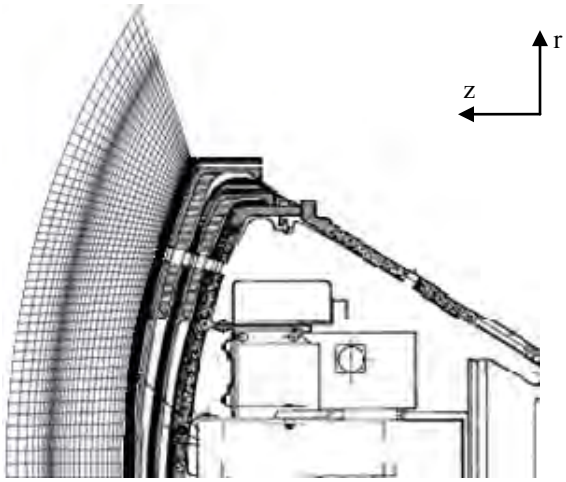

Figure 8. FIRE II Geometry and Grid with Adaptation Applied in the Shock and Boundary Layers

The parameters of the spectral calculations were chosen in order to facilitate a comparison of the different radiation solutions resulting from the multitemperature and

two-temperature flow fields. The range of wavelengths used in this study was 2,000-40,000 Angstrom with 100,000 points used to discretize this spectral range. The radiation bands and mechanisms considered in the present study are listed in Table 7.

Table 7. Parameters for Radiation Solution

Species	Mechanisms	Key	State Transitions
N_2	Vegard-Kaplan	VK	$\left(A^3\Sigma_u^+ \leftrightarrow X^1\Sigma_g^+\right)$
N_2	1st Positive	1+	$\left(B^3\Pi_g \leftrightarrow A^1\Sigma_u^+\right)$
N_2	2nd Positive	2+	$\left(C^3\Pi_u \leftrightarrow B^3\Pi_g\right)$
N_2	Lyman-Birge-Hopfield	LBH	$\left(a^1\Pi_g \leftrightarrow X^1\Sigma_g^+\right)$
N_2	Birge-Hopfield 1	BH1	$\left(b^1\Pi_u \leftrightarrow X^1\Sigma_g^+\right)$
N_2	Birge-Hopfield 2	BH2	$\left(b'^1\Pi_u \leftrightarrow X^1\Sigma_g^+\right)$
O_2	Schuman-Runge	SR	$\left(B^3\Sigma_u^- \leftrightarrow X^3\Sigma_u^-\right)$
NO	β	Beta	$\left(A^2\Sigma^+ \leftrightarrow X^2\Pi_r\right)$
NO	Γ	Gamm	$\left(B^2\Pi_r \leftrightarrow X^2\Pi_r\right)$
NO	δ	Delt	$\left(C^2\Pi_r \leftrightarrow X^2\Pi_r\right)$
NO	ε	Epsi	$\left(D^2\Sigma^+ \leftrightarrow X^2\Pi_r\right)$
N	Bound-Bound	N	
O	Bound-Bound	O	

λ_{min}	λ_{max}	N_λ
2,000	40,000	100,000

Comparison of Two-Temperature and Multitemperature Models

Three trajectory points from the FIRE II experiment were chosen for use in this investigation. This set of trajectory points exhibits a range of nonequilibrium conditions, which range from severe nonequilibrium to near equilibrium. The 1634.0-second trajectory point exhibits the highest degree of thermal nonequilibrium, while the 1636- and 1640.5-second trajectory points exhibit progressively more equilibrium behavior. In this section, the effects of exchanging the two-temperature model for the multispecies-multitemperature model are discussed according to the characteristic features observed in the flowfield quantities. Figure 9 a) presents a comparison of the temperature profiles along the stagnation line of the NH7AIR and LAURA flowfields at 1634.0 seconds. Both solutions exhibit a shock stand-off distance of about 7 cm with comparable heavy particle and electronic temperatures in the shock layer.

However, some significant difference exists between the two solutions. Of first importance, is the fact that NH7AIR predicts species-vibrational temperatures which—rising quickly within the shock—are far from being at equilibrium with the electronic temperature. That vibrational and electronic temperatures are in equilibrium is a key assumption of the two-temperature model. The effect of allowing the species-vibrational energy modes to relax separately from the electronic modes is that they are able to do so more quickly, according to their relatively faster relaxation times. This results in a predicted peak temperature for NH7AIR which is about 5,000 K lower than LAURA, as well as an observable reduction of the shock thickness. Another difference between the results of the two solution methods becomes more noticeable when the remaining two trajectory points are considered. Figures 9 b) and c) show that NH7AIR consistently

predicts a reduction in peak temperature and shock thickness. However, it is apparent with these two cases that NH7AIR predicts a higher equilibrium temperature in the shock layer than does LAURA.

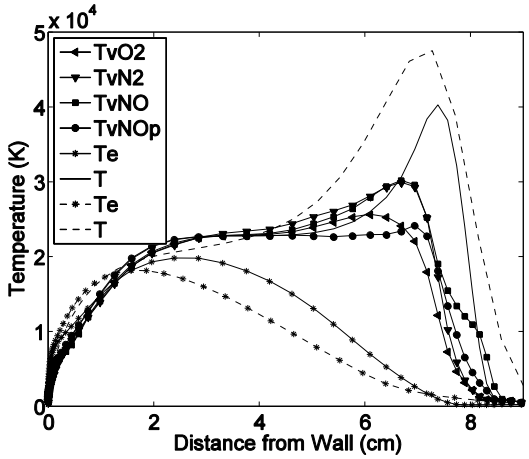

Figure 9. a) Comparison of Temperature Profiles: 1634.0 seconds; s*olid and dashed lines represent the NH7AIR and LAURA data, respectively.*

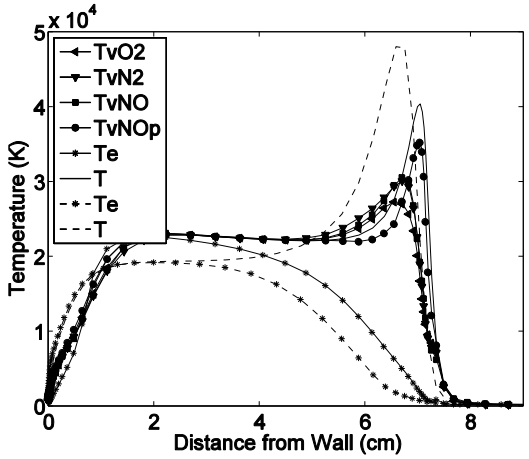

Figure 9. b) Comparison of Temperature Profiles: 1636.0 seconds

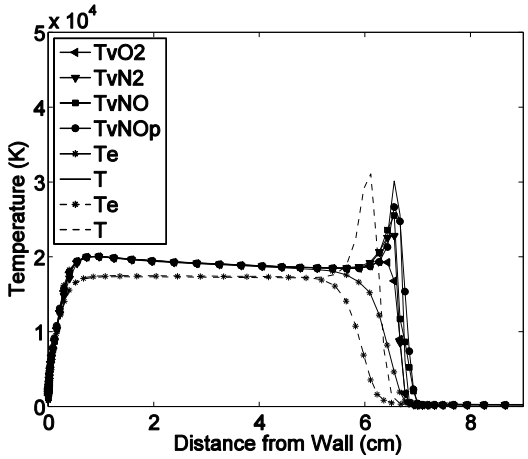

Figure 9. c) Comparison of Temperature Profiles: 1640.5 seconds

Figures 10 and 11 compare the density and pressure profiles along the stagnation streamline at each of the three trajectory points considered. While both figures indicate a substantial difference in shock strength and standoff distance at each of the three selected trajectory points, the solutions obtained by NH7AIR show a reasonable correlation in pattern with those obtained by LAURA in terms of the pre- and post-shock flow conditions. The higher temperatures predicted by NH7AIR, together with the post-shock pressures which are nearly identical to those obtained by LAURA, result in lower density in shock-layer and thereby the greater shock standoff distances observed in the NH7AIR data. It is speculated that the greater post-shock temperature rise observed in the results obtained under multispecies, multitemperature model is the result of a decreased production of entropy relative to the two-temperature model. The transfer of energy between energy modes which are out of equilibrium is somewhat analogous to the transfer of energy to a body from a surrounding heat bath (Vincenti and Kruger, 1967). However, in this case, energy in not transferred between bodies separated in space, rather it is transferred between energy modes separated by their respective degrees of freedom.

Here consider an energy mode with a particular degree of freedom (e.g., simple harmonic oscillator) which is out of equilibrium with the surrounding heat bath at temperature T. It can be shown that, for an energy mode with an energy content sufficiently specified by a characteristic temperature T_i, the entropy produced by heat transfer from the heat bath to this *i*-th energy mode is given by

$$ds_i = \left(\frac{1}{T_i} - \frac{1}{T} \right) de_i . \tag{171}$$

From this expression, it is evident that entropy production due to this transfer of energy from the heat bath to the nonequilibrium energy mode is zero only for the case where $T_i = T$ or $de_i = 0$, which is the case of thermal equilibrium. Therefore, if the thermodynamic state is closer to equilibrium, these nonequilibrium processes will produce less entropy; such is the case for the solutions obtained by the multispecies-multitemperature thermal model. A reduction in entropy production means more useful energy is recovered to expand and heat the gas in the shock-layer, thereby raising post-shock temperatures, lowering density and increasing the shock stand-off distances. This effect is more pronounced in the NH7AIR results, which is consistent with a reduction in the production of entropy through the shock wave.

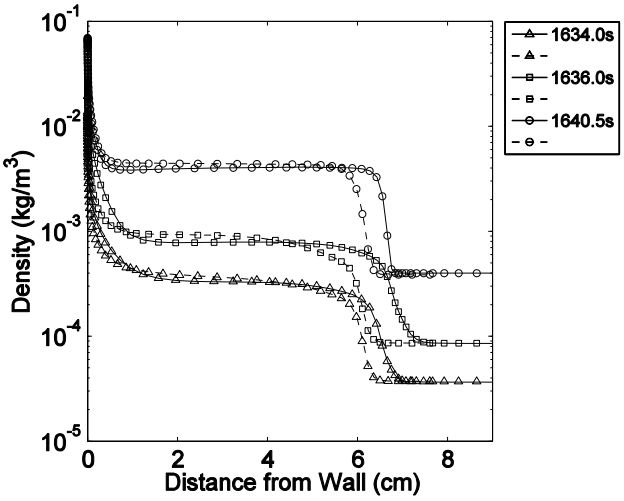

Figure 10. Comparison of Density Profiles; s*olid and dashed lines represent NH7AIR and LAURA data, respectively.*

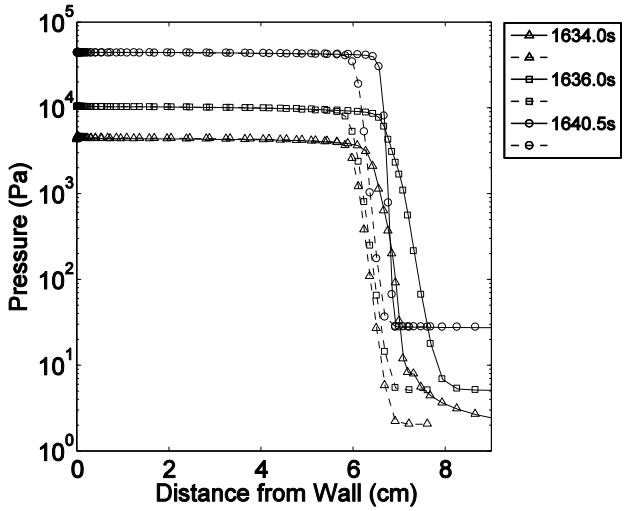

Figure 11. Comparison of Pressure Profiles; s*olid and dashed lines represent NH7AIR and LAURA data, respectively.*

Figure 12 presents data regarding the number densities calculated *via* NH7AIR and LAURA, respectively. Both depict physically realistic gas composition along the streamline, with a high degree of agreement between NH7AIR and LAURA. Ahead of the shock the concentrations reflect those specified at the inflow boundary. Through the shock, the diatoms N_2 and O_2 dissociate and, consequently, the number densities of these

species drop several orders of magnitude, from about 10^{20} particles/cm^3 down to 10^{14} particles/cm^3 at 1634 s and 10^{16} particles/cm^3 at 1640.5 s. The increase in the number densities of the atomic species, N_N and N_O, is the result of strong dissociation through the shock, causing these values to rise from their freestream values to about 10^{22} particles/cm^3 in the shock-layer. Higher atomic number densities occur at later trajectory points due to the higher freestream density. N_{NO} increases by about five orders of magnitude through the shock to a typical value of approximately 10^{17} particles/cm^3, with NO being present in small numbers due to its function as an intermediate reaction between the diatomic species and the fully dissociated and ionized species.

In the post-shock region away from the wall, the number densities of the diatomic species either level off or continue to fall. The number density for the only ionized species considered in this investigation N_{NO}+ appears to rise quickly through the shock and to level off in the shock-layer around 10^{19} to 10^{20} particles/cm^3. NO^+ constitutes about 0.1% of the flow in terms of the total number of particles. Approaching the wall, there is an increase in the number densities of the diatomic species then a sudden drop in the number densities of NO and NO^+, corresponding to a sudden rise in the atomic species at the wall. The differences between the two flowfield solution methods in terms of the number densities of the most prevalent species in the post-shock region (N, O, and NO^+) are within an order of magnitude or better for each of the selected trajectory points.

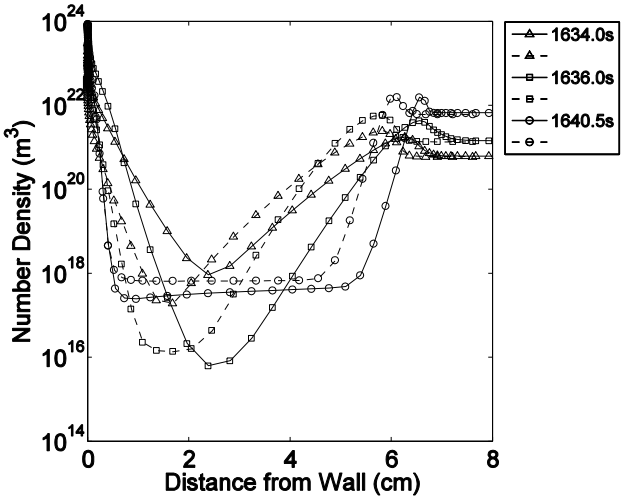

Figure 12. a) Comparison of N_2 Stagnation-Line Number Density Profiles. *Solid and dashed lines represent NH7AIR and LAURA data, respectively.*

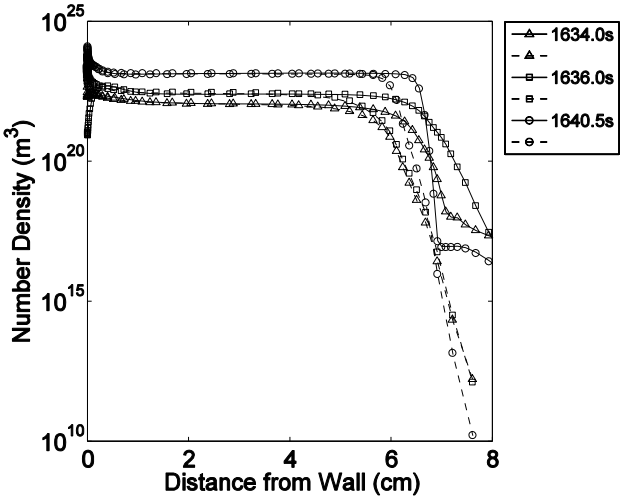

Figure 12. b) N Stagnation-Line Number Density Profiles

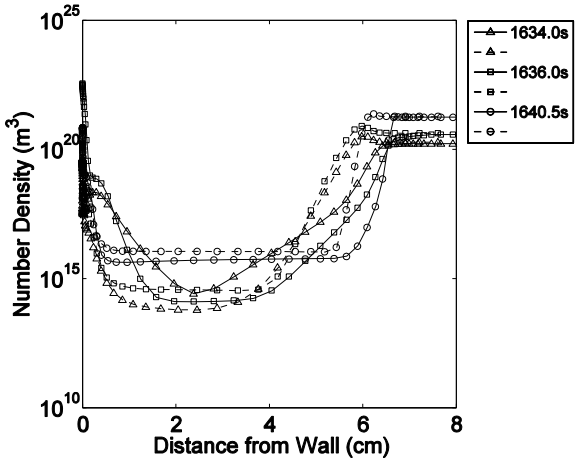

Figure 12. c) O_2 Stagnation-Line Number Density Profiles

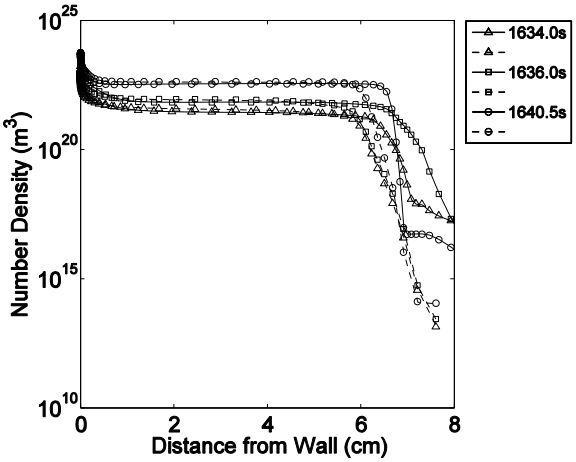

Figure 12. d) O Stagnation-Line Number Density Profiles

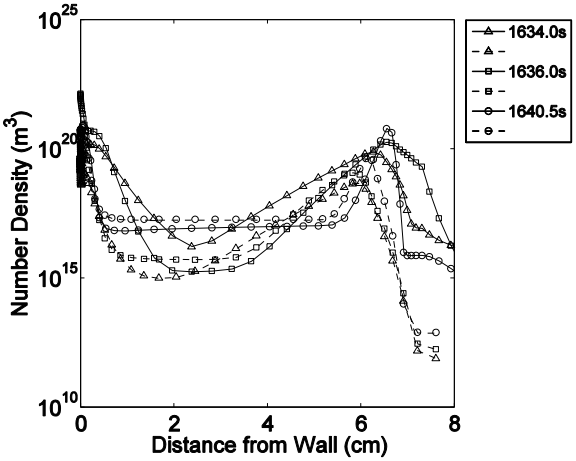

Figure 12. e) NO Stagnation-Line Number Density Profiles

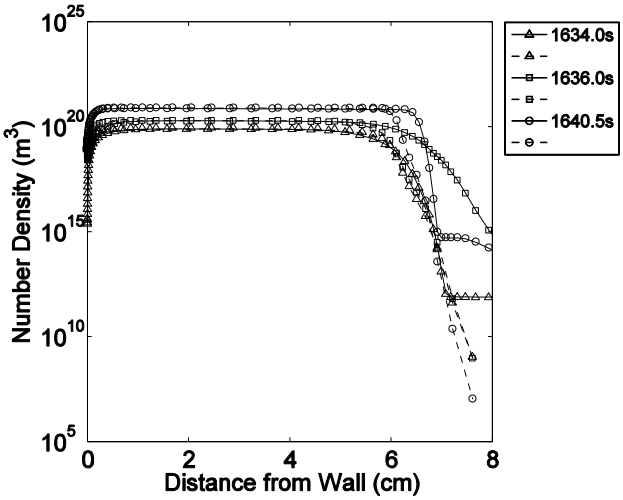

Figure 12. f) NO^{+} Stagnation-Line Number Density Profiles

Uncoupled Radiation.

In terms of the radiation solutions obtained from the flow field results above, the effects of substituting the two-temperature thermal model with the multispecies-multitemperature model are significant. Stagnation point radiative intensity at the 1634.0-second trajectory point was estimated to be 245.0 (W/cm^2–sr) and 390.0 (W/cm^2-sr) for the two-temperature and multispecies-multitemperature models, respectively. Variation of normal intensity is plotted along the stagnation line in Figure 13; the key may be referenced to the full mechanism names given previously in Table 7. It is readily noticeable that the radiation calculated from the two flow field models is very different both in terms of magnitude and spatial distribution.

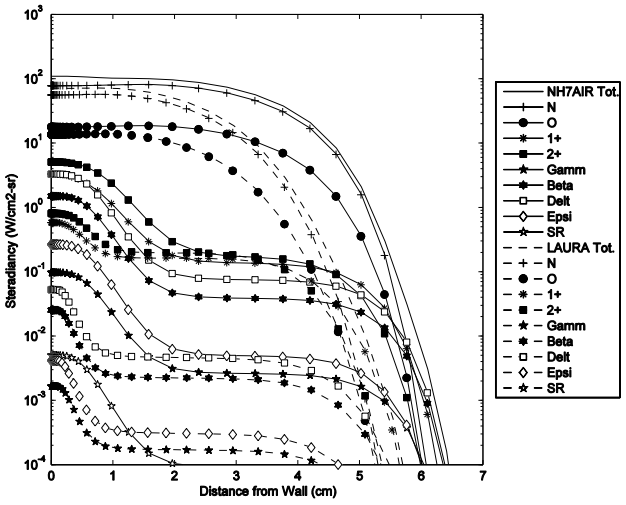

Figure 13. a) Incoming Normal Intensity along the Stagnation Line: 1634.0 seconds.

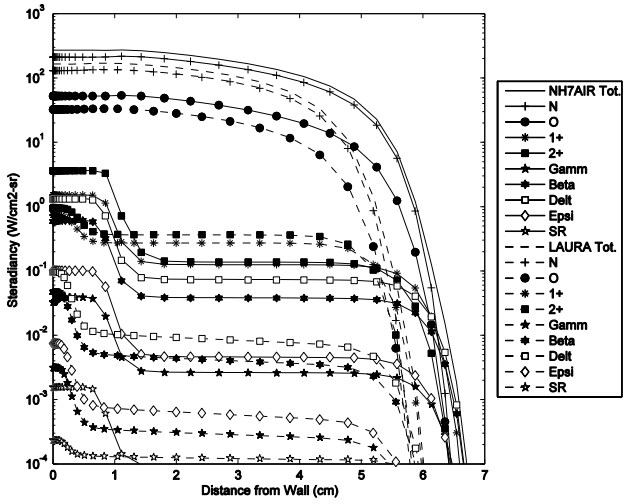

Figure 13. b) Incoming Normal Intensity along the Stagnation Line: 1636 seconds

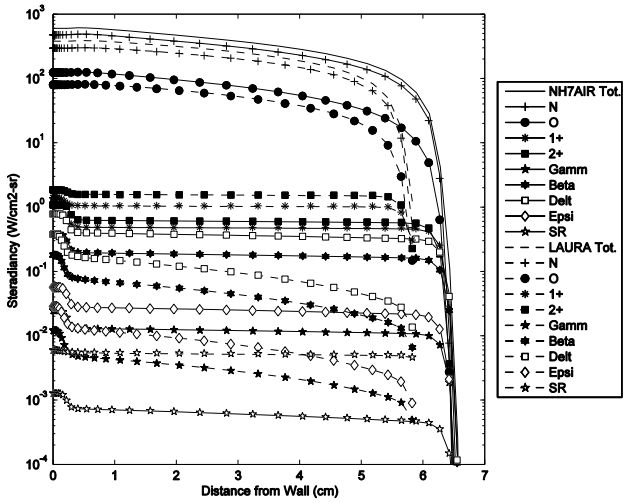

Figure 13. c) Incoming Normal Intensity along the Stagnation Line: 1640.5 seconds

Inspection of Figure 13 suggests that the vast majority of the emission is from the bound-bound transitions of the atomic species while only a very small fraction is attributable to vibrational bands of the diatomic species. It is also noted that atomic radiative emission occurs at a higher rate in the shock for the NH7AIR data. This effect is due to the higher dissociation rates there, resulting from the much higher vibrational temperatures. Table 8 presents a comparison of the radiative intensity reaching the wall

along the stagnation line for the uncoupled cases considered above. The total radiative intensities presented here have been integrated over a spectral range of 0.2-4.0 μm in order to compare them with the total radiometer measurements collected aboard the FIRE II flight experiment. The reader is reminded that the cases considered here are uncoupled from the radiative heat transfer mechanisms and thus do not take into account the very significant effect of radiation cooling which can drastically lower the radiative intensity within the flowfield. As will be shown in the next section, the effect of radiation cooling can reduce these values by an order of magnitude or more at the flow conditions.

Table 8. Radiative Intensity at the Stagnation Point for Uncoupled Cases with Flight Data from the FIRE II Experiment. *Results integrated over a spectral range of 0.2-4.0 μm.*

Time (s)	NH7AIR (W/cm^2-sr)	LAURA (W/cm^2-sr)	FIRE II (W/cm^2-sr)
1634.0	68.0	50.1	1.3
1636.0	180.0	114.0	5.0
1640.5	390.0	245.0	35.0

Comparison of Uncoupled and Coupled Radiative Transport Results

The observations made above regarding the comparison of uncoupled radiative transport solutions obtained under the two-temperature and multispecies-multitemperature thermal models reveal that although solutions under the multispecies-multitemperature model may bear a certain resemblance to their two-temperature counterparts it terms of peak temperature, shock stand-off distance and chemical composition, marked differences were easily distinguished in terms of the nonequilibrium distribution of energy among the various energy modes. The most noticeable difference

was the apparent violation of the assumption inherent in the two-temperature model, namely, that the vibrational and electronic energy manifolds are far from equilibrium within both the shock and relaxation zone. This effect is perhaps not surprising, considering that, due to the disparity in mass between electrons and heavy particles, the energy exchanges which occur between the two are relatively inefficient as compared to energy exchanges between heavy particles and diatomic molecules (Park, 1991). In Figure 14 a) - c), the disparity between vibrational and electronic temperatures is observed quite readily. The vibrational temperatures rise throughout the very diffuse shock and equilibrate with the heavy particle temperature downstream of the shock, while the electron temperature climbs slowly through both the shock and subsequent downstream region, finally equilibrating with the heavy particle and vibrational temperatures just before reaching the wall.

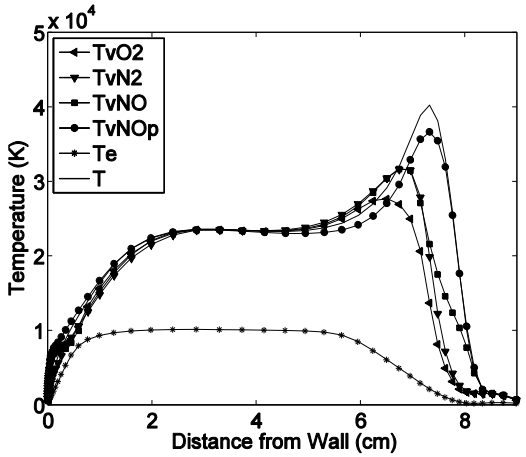

Figure 14. Stagnation-Line Temperatures from Coupled NH7AIR-SPRADIAN Solutions: a) 1634.0 seconds

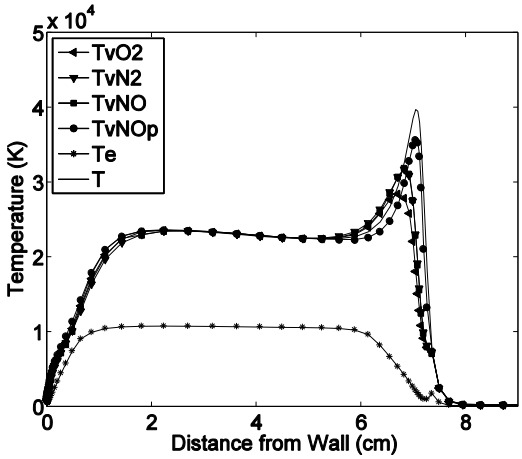

Figure 14. b) 1636.0 seconds

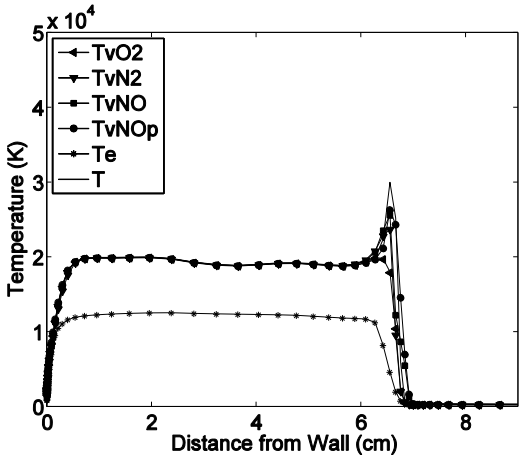

Figure 14. c) 1640.5 seconds

Leaving aside the results of the uncoupled investigation, the coupled solutions are now examined as obtained by the multispecies-multitemperature nonequilibrium flow solver. First of all, certain features of the solution were striking. One might expect a drop in all temperatures in the shock layer, a higher rate of recombination in the shock layer, and a reduction in shock standoff distance. Instead, results show a dramatic change in the nonequilibrium energy distribution within the flowfield and almost no change in flow composition. The most significant effect of coupling the radiation source terms with the nonequilibrium flow solver was the dramatic drop in electron temperature. This drop

in electron temperature was accompanied by a modest rise in heavy and species-vibrational temperatures.

While coupling radiation source terms into the flow solver resulted in a significant reduction of the electronic temperature within the flow field, this had a negligible effect on flowfield composition throughout most of the solution domain. Notwithstanding this result, some small variations in flow composition were noted for a few of the coupled cases in the regions of the flow near the wall and traversing the shock. For instance, Figure 15 shows that the coupled result, for the 1634.0-second trajectory point, exhibits a faster ionization rate traversing the shock due to the higher electronic temperature there.

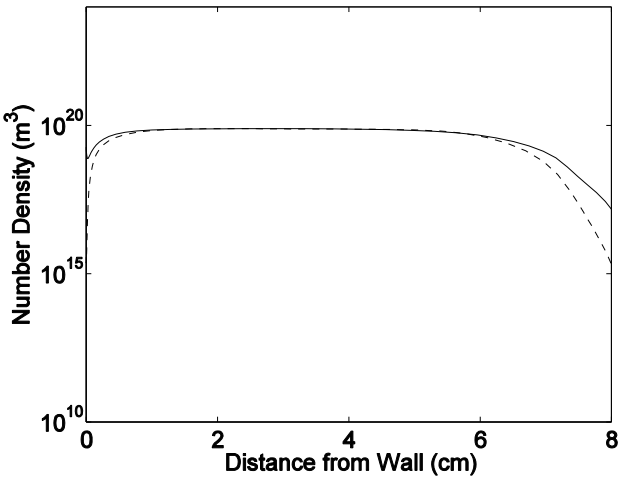

Figure 15. Stagnation-Line Number Density Profiles of NO^+: 1634.0-second; s*olid and dashed lines represent the coupled and uncoupled NH7AIR-SPRADIAN cases, respectively.*

Also, it is noted that coupling seems to have had the effect of slowing the recombination of N and O to produce O_2 and NO near the wall, for the 1636-second coupled case, as shown in Figures 16 a) and b), consistent with the higher electronic temperature observed in the uncoupled cases.

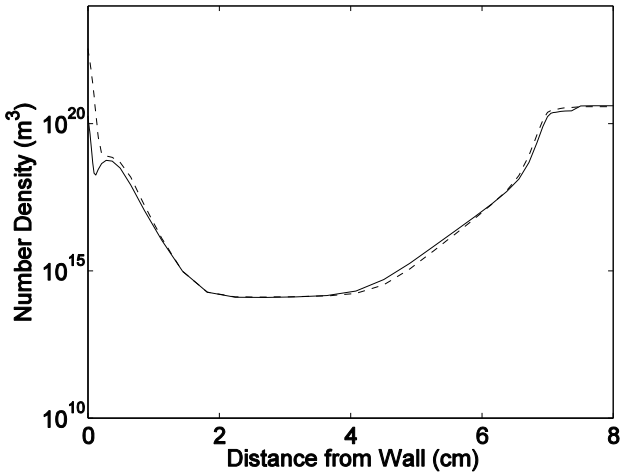

Figure 16. a) Stagnation-Line Number Density Profiles of O_2: 1636 seconds. *Solid and dashed lines represent the coupled and uncoupled NH7AIR-SPRADIAN cases, respectively.*

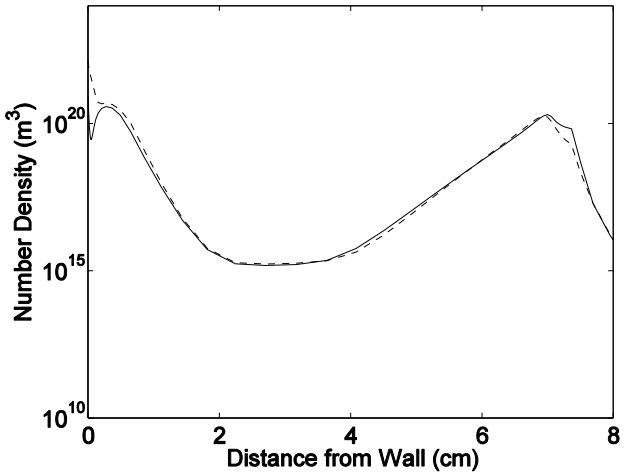

Figure 16. b) Stagnation-Line Number Density Profiles of NO: 1636 seconds

Coupled Radiation.

Results presented here are delineated according to two parameters. The first parameter is the total integrated radiative intensity, calculated using the tangent-slab approximation to radiative transport equation. Figures 17 a) - c) shows the profiles of integrated intensity for the selected trajectory points. Intensity profiles have been plotted on a logarithmic scale in order to illustrate the diverse range of contributions from the

various participating radiative mechanisms to the total radiative intensity. This figure, which is analogous to the uncoupled results in Figure 13, readily shows that the dominating radiative mechanisms are from the line emissions of the atomic species, most notably nitrogen, which generally accounts for as much as 90% of the total radiation in the cases investigated. The molecular band mechanisms contribute much less to the total radiation relative to the atomic line radiation, due largely to being much fewer in number relative to atomic species. This point is illustrated by the rise in radiative intensity approaching the wall where recombination, together with a sufficiently high electronic temperature, affects a marked rise in net radiative emission from the molecular mechanisms.

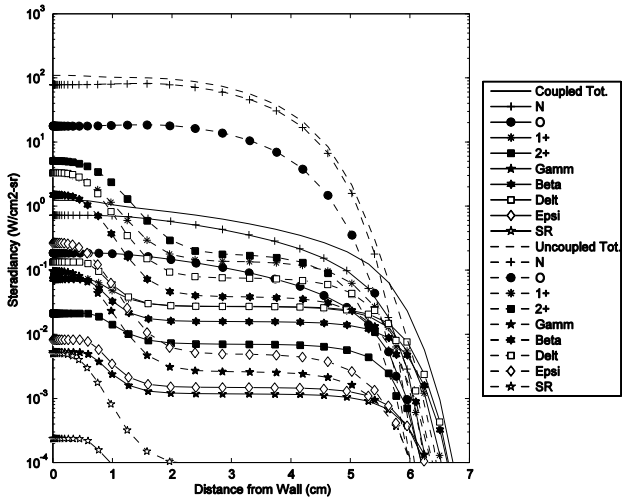

Figure 17. a) Incoming Normal Intensity along the Stagnation Line: 1634.0 seconds; s*olid and dashed lines represent the coupled and uncoupled NH7AIR-SPRADIAN cases, respectively.*

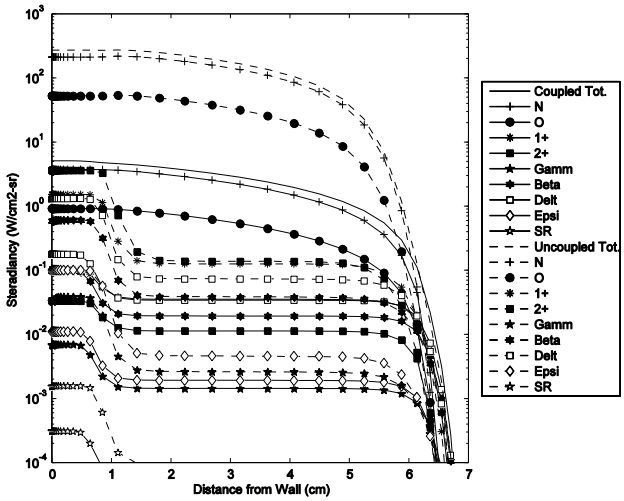

Figure 17. b) 1636.0 seconds

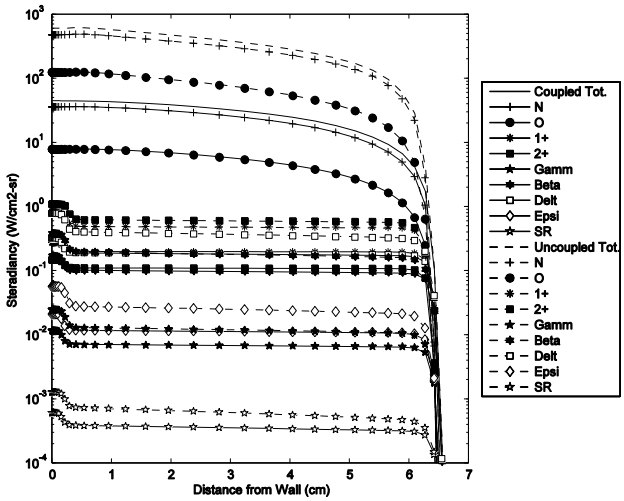

Figure 17. c) 1640.5 seconds

In general, radiative emission is a strong function of upper electronic state populations; as such, these populations serve as the second parameter along which the radiative results may be examined. Figures 18 a) and b) show a representative pair (i.e., coupled and uncoupled solution) of state populations for N.

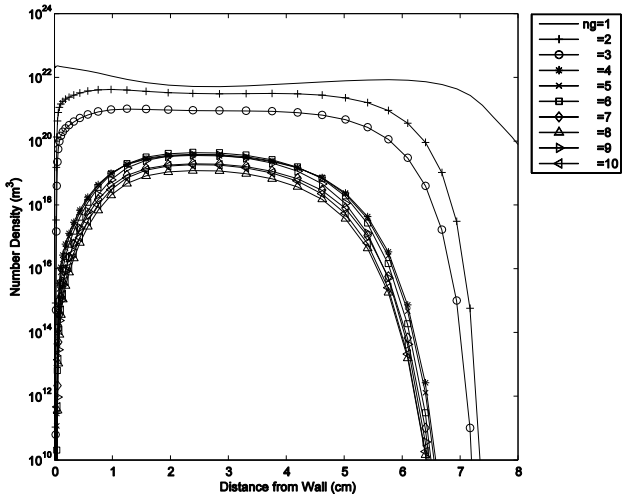

Figure 18. a) Nonequilibrium Group Populations of N: Uncoupled NH7AIR, 1634.0 seconds

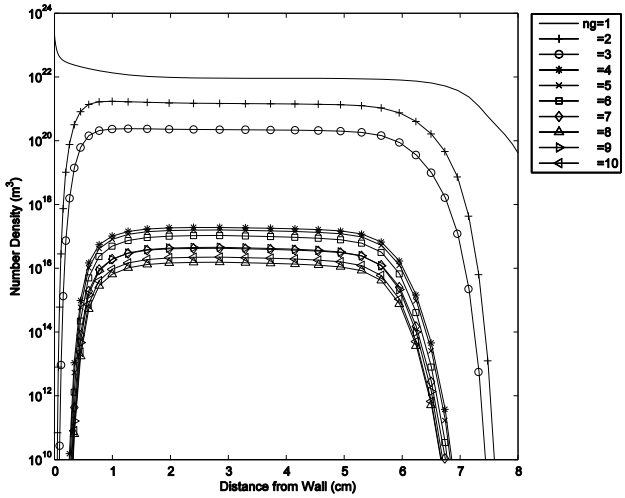

Figure 18. b) Coupled NH7AIR-SPRADIAN, 1634 seconds

Two trends are evident looking at the differences in the state populations of the various species at each of the cases. First, the populations of the ground states are fairly similar (i.e., same order of magnitude) between coupled and uncoupled cases. Second, the state populations of the upper energy states show orders of magnitude differences between coupled and uncoupled solutions. This effect is due to the change in the electron temperature. Coupled solutions exhibit a radiative cooling effect of the electrons which

redistributes the internal energy to the lower energy levels for radiating species. Plots of the state populations for the remaining species and trajectory points are listed in Appendix B.

Table 9 summarizes these results by way of comparison with experimental data obtained from the FIRE II flight experiment. As expected, coupling the radiation and flowfield solutions had the effect of significantly reducing the amount of radiative energy present in the solution domain, thus reducing the amount of radiation incident on the wall. Given the uncertainties involved with both the flight data collected from the FIRE II flight experiment and the thermophysical data available for these sorts of computations, the coupled NH7AIR-SPRADIAN results agree quite well with the experimental data. The best agreement was observed in the near equilibrium conditions of the 1640.5-second trajectory point, and the least agreement was observed in the severe nonequilibrium conditions of the 1634.0-second trajectory point. This trend in the errors is typical of the results obtained by other researchers (Johnston, 2006). However, it is key to note that the results presented here not only agree reasonably well the FIRE II data but underpredict the amount of radiation observed. The significance of this result arises in light of the fact that the radiometer windows on the FIRE II vehicle were recessed into the heat shields, thereby capturing some radiating ablation products. This trapped ablation material contaminated the radiometer data to some unknown degree, resulting in reporting of inflated intensity measurements (Greendyke, 2011). Logically, the contribution of the air species in the flow field to the radiative intensity must be lower than the reported values. Thus, the agreement between the coupled NH7AIR-SPRADIAN results reported here and the FIRE II data is better than it may initially seem, especially

for the case of severe nonequilibrium where calculated intensities tend to be higher than those reported in the FIRE II data or from comparable results in the literature as reported by Johnston (2006).

Table 9. Radiative Intensity at the Stagnation Point for Coupled NH7AIR-SPRADIAN FIRE II Cases. *Results integrated over a spectral range of 0.2-4.0 μm.*

Time (s)	Uncoupled (W/cm^2-sr)	Coupled (W/cm^2-sr)	Exp. (W/cm^2-sr)	Literature (lo-hi) (W/cm^2-sr)
1634.0	68.0	0.5	1.3	0.3-2.6
1636.0	180.0	2.8	5.0	2.6-6.8
1640.5	390.0	30.0	35.0	12.0-39.0

Finite Volume Method for Radiative Transport

The finite volume method for radiative transport (FVMR) within the flow field yields a full 3-dimensional solution to the radiative transport equation which conserves radiative energy. This property of conserving radiative energy makes the FVMR a desirable method for calculating source terms for coupling with a flow solver—an especially important consideration for strongly absorbing media such as air in the VUV spectra. However, without a parallelized solution algorithm, obtaining solutions using this method is computationally prohibitive. Since it was outside of the scope of this work to parallelize the computer code, only approximate results using the FVMR approach are presented here. These results are approximated by considering the radiative transport resulting from emission and absorption coefficients which have been calculated with a very coarse spectral resolution. A spectral resolution of 10,000 grid points has been used here in contrast to the 100,000 grid points used in the preceding sections. Also, the solutions presented here were calculated using the thermodynamic variables obtained from the flow fields in the previous section. Trying to calculate coupled solutions with

such a coarse spectral resolution would not have yielded any result more meaningful than those presented here. Finally, the radiative transport equation was solved using the spectrally coarse coefficients.

Table 10 summarizes the results obtained *via* the coarse FVMR calculation described above. These FVMR results are presented alongside tangent slab results at the same level of spectral resolution for comparison. There appears to be fairly good agreement between the two methods for the 1634.0 and 1636.0 second trajectory points. It is suspected that the unusually high value for the FVMR at 1640.5 seconds is due to geometrical effects.

Table 10. Integrated Radiative Intensity at the Stagnation Point for Uncoupled Cases (NH7AIR-SPRADIAN). *Results integrated over a spectral range of 0.2-4.0 μm with N=10,000 spectral grid points.*

Time (s)	Tangent Slab (W/cm^2-sr)	FVMR (W/cm^2-sr)
1634.0	2.2	2.3
1636.0	21.0	24.6
1640.5	187.6	671.0

The reader will recall that 6 transmission directions were considered in this work. The first two plots presented in Figures 19 a) and b) are for the positive and negative z direction transmission directions, respectively. The z-axis runs along the line of symmetry and is positive in the direction away from the body. These solutions are roughly analogous to the tangent slab solution in the stagnation region. The second set of plots presented in Figures 19 c) and d) are for the positive and negative r direction transmission directions. The r-axis runs radially from the line of symmetry out to the farfield. These two solutions exhibit the geometric effects discussed in the previous

chapter related to the calculation of radiative transmission *via* the FVMR within an axisymmetric wedge. Finally the solution in the θ direction is presented in Figure 18 e). The θ-axis is out of the plane in the figures below and has a circumferential orientation in the coordinate system. The reader will recall that it is not possible to use the FVMR to calculate a solution for transmission directions which include a component in the θ direction with the grid topology used here. In order to calculate the radiation transmitted in these directions it is necessary to use the complete, 3-dimensional domain. Therefore, the result presented below simply represents the net intensity radiated from the wedge under consideration.

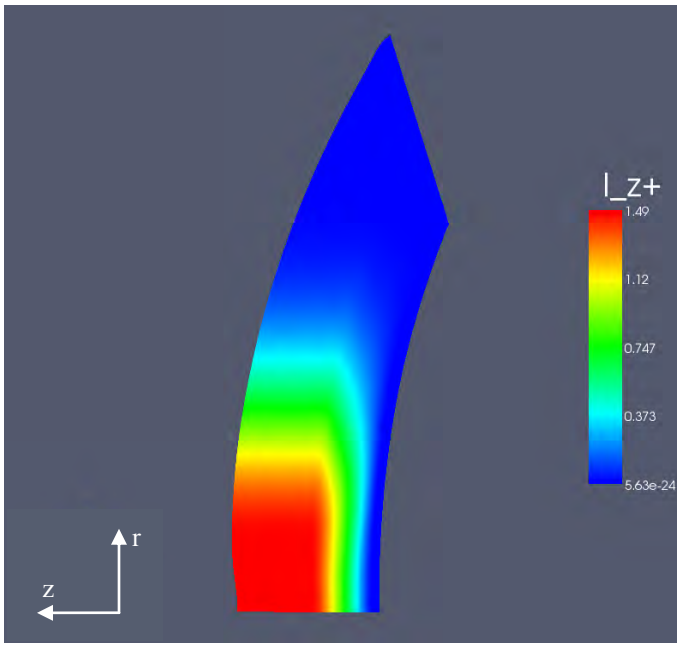

Figure 19. a) Spectrally Integrated z+ Direction Intensity, I^{z+}, from Uncoupled FVMR Solution, 1634 seconds

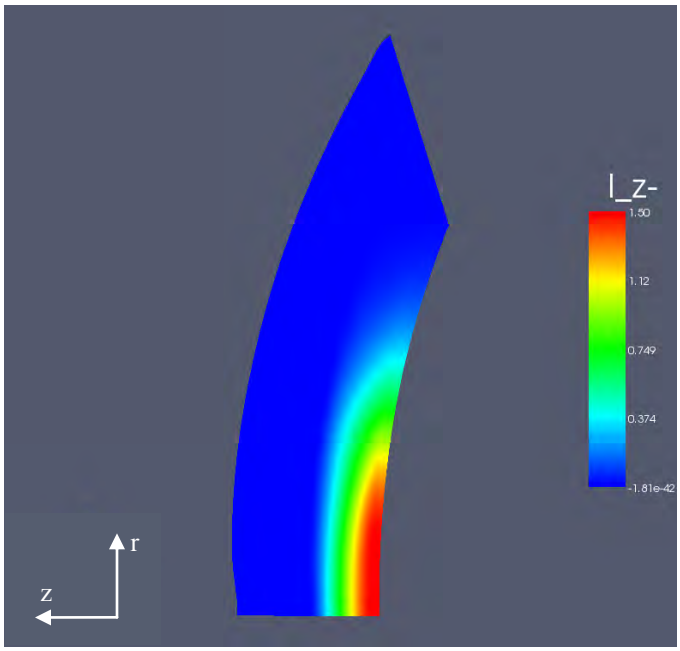

Figure 19. b) Spectrally Integrated z- Direction Intensity, I^{z-}, from Uncoupled FVMR Solution, 1634 seconds

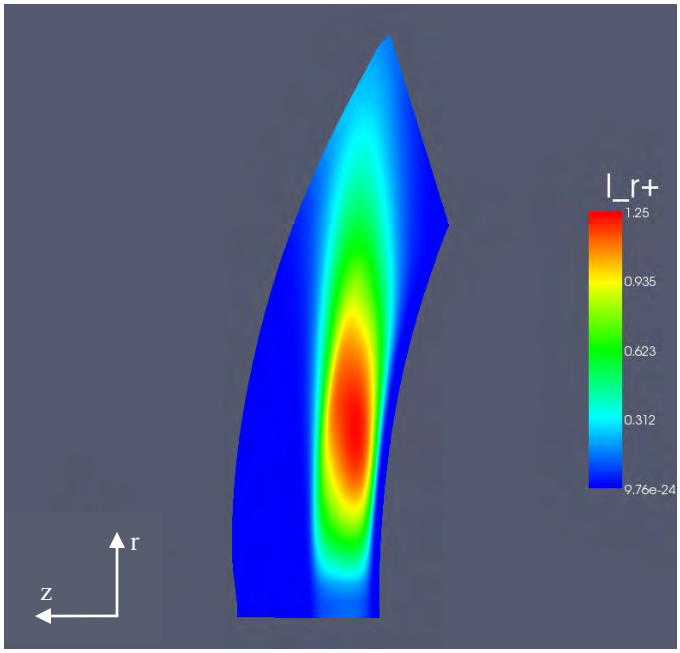

Figure 19. c) Spectrally Integrated *r*+ Direction Intensity, I^{r+}, from Uncoupled FVMR Solution, 1634 seconds

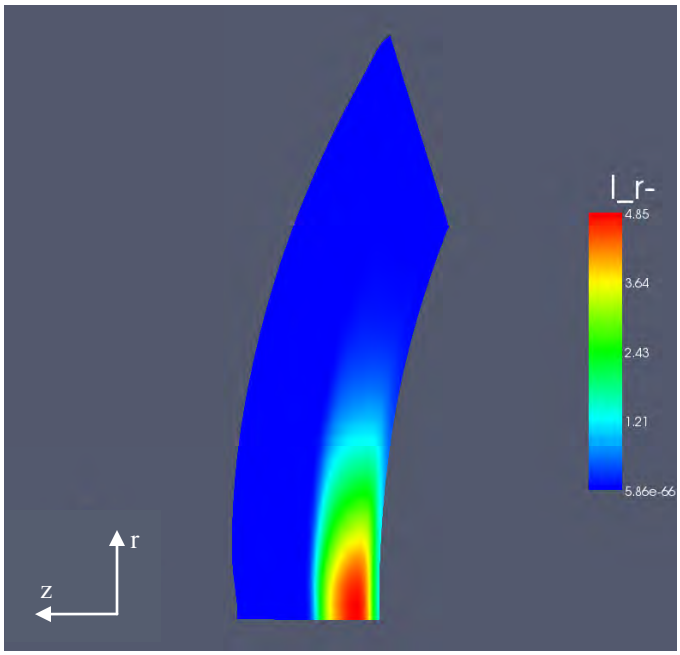

Figure 19. d) Spectrally Integrated *r*- Direction Intensity, I^{r-}, from Uncoupled FVMR Solution, 1634 seconds

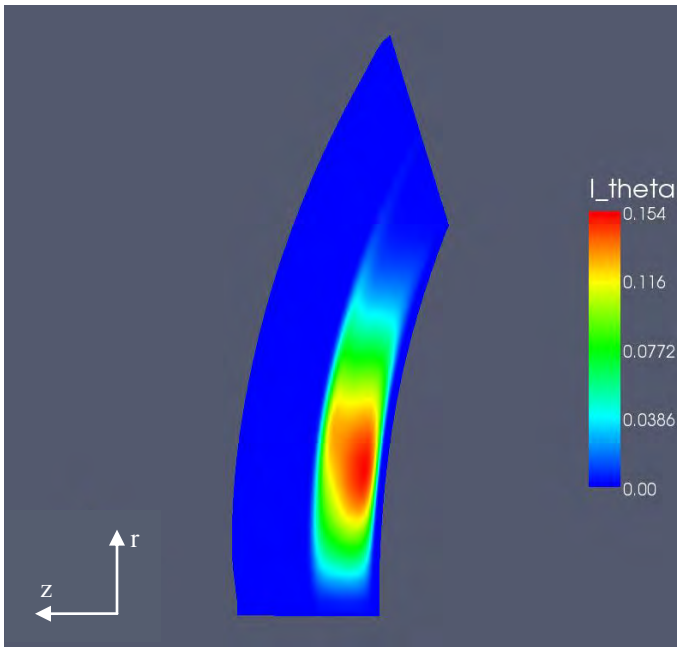

Figure 19. e) Spectrally Integrated θ Direction Intensity, I^{θ}, from Uncoupled FVMR Solution, 1634 seconds

V. Conclusions

As the United States, its allies and its foes continue to pursue the development of new hypersonic systems, the computational modeling of phenomena associated with hypersonic flight will play a key role in unlocking the physical understanding requisite to their design, manufacture and deployment. Furthermore, given the development and weaponization of such systems, highly accurate modeling of radiating shock layers may provide the critical MASINT data which will enable the timely detection and neutralization of threats of this kind to the US and its allies.

Radiation modeling has been extensively studied, particularly with respect to the atmospheric reentry of spacecraft, as exemplified by the breadth and depth of literature on the subject. Numerous computer codes have been developed for modeling the radiation produced in these situations. The level of approximation accepted in these computer codes has varied from those utilizing simple band models in order to characterize the spectral variation of the radiative transport properties to highly sophisticated, computationally expensive line-by-line methods. In the past couple of decades especially, what all these methods have shared in common has been the utilization of the two-temperature model of thermal nonequilibrium. The present work has sought to advance the state-of-the-art by proposing a more detailed model of nonequilibrium, namely the multispecies, multitemperature model. In this dissertation, a complete computational method has been developed around the line-by-line radiation solver SPRADIAN and the sophisticated nonequilibrium flow solver NH7AIR which implements this multispecies, multitemperature model.

The first phase of code development utilized the standard tangent slab method of solving the radiative transport equation. Results were obtained first without coupling radiative effects. These uncoupled results, obtained utilizing the multitemperature flow solver NH7AIR, were compared to the uncoupled results obtained utilizing the two-temperature flow solver LAURA. The result of this comparison was to show that, in the flow fields of the FIRE II cases which were examined, the two-temperature model does not describe the nonequilibrium processes involved as well as the multitemperature model. The two-temperature model accounts for the redistribution of internal energy among the vibrational, electronic and free electron manifolds, but not with as much fidelity as the multi-species, multi-temperature model. This lack of fidelity in previous methods has significant implications for the characterization of the spectral features of radiating gases modeled in reentry shock layers, since the radiative properties of the flow field depend in a strongly nonlinear fashion upon the temperatures which are calculated as a result of these nonequilibrium models.

Next, the tangent slab method was implemented within the flow field-radiation solver in a coupled manner and validated against data collected during the FIRE II flight experiment. The coupled implementation of the NH7AIR and SPRADIAN with the tangent slab method dramatically illustrated the effects of radiative cooling in the modeling of reentry shock layers. Furthermore, excellent agreement was obtained with the FIRE II experimental data, especially for the severe nonequilibrium conditions of the 1634.0-second trajectory point. An 11-species air chemistry model would likely improve these results still further.

The second phase of code development focused on the implementation of a suitable FVM scheme for solving the radiative transport equation. This FVMR solution method was successfully developed and implemented in an uncoupled fashion within the developed computer code. The results compared with those obtained from the tangent slab method. The FVMR of calculating radiative intensity is extremely memory intensive because of the extensive linear system created by attempting to resolve both the spatial, directional and spectral contributions of the radiation solution. It is necessary to parallelize the FVMR in order to use the level of spectral resolution needed in order to calculate an accurate coupled flow field-radiation solution. In an effort to present some manner of result, spectrally coarse, uncoupled calculations were performed on the FIRE II flow fields in order to obtain both tangent slab and FVMR solutions. Comparing these two solutions yielded a reasonable amount of agreement. However, in the course of analyzing the results of the FVMR scheme some undesirable geometric effects were observed which indicate that this method would be more appropriately applied in a fully three-dimensional radiation grid rather than the axisymmetric wedge used for the flow solver.

The further development of the FVMR should continue. Since it is based on a conservation law, it should yield more physical results than the tangent slab method when coupled with a flow solver. This improvement, together with the improvements afforded by the multispecies multitemperature thermal model, will ultimately result in superior coupled flowfield-radiation solutions compared with present capabilities. This improved modeling capability may one day aid in the development of a high-performance reusable space access vehicles or hypersonic cruise missile technology. Alternately, they may

serve to populate a database of MASINT signatures used to identify incoming threats. In this case, the accuracy of these methods could mean the difference between a castrophic surprise attack by a stealthy hypersonic weapon system and a successful defense against such threats.

Recommendations.

In order to further improve the solution method presented in this dissertation, a few key recommendations are here made for the consideration of those who may desire to develop this method further. The first recommendation is that the work of updating the chemistry model be undertaken. Updating the chemistry model to an 11-species air model will enable a more accurate calculation of the flow composition at the conditions of interest. The additional ionization processes will also have the effect of lowering the post-shock temperatures, which in turn will have an effect on the amount of radiation produced and coupled into the flow field solution.

The second recommendation is that a careful study of the combined flow field – radiation solver be undertaken in order to determine optimum method by which to parallelize the code. There are many time-intensive calculations within the radiation solver which are physically independent and would lend themselves well to a parallelized implementation.

Finally, it is recommended that work be done in order to develop a method by which the thermodynamic flow quantities may be interpolated onto a separate grid which has been optimized for solving the radiative transport equations. After obtaining the radiation solution on this optimized grid, the source terms could then be interpolated back

onto the flow field grid and in this way be coupled into the flow solver. Additionally, attention should also be given to enhancing the stability of the radiative coupling.

Appendix A: Selected Listings of Computer Code

Table 11. Parameters Directing Radiation Solution added to Read Statements

Subroutine *datin*; bold text indicates modifications to baseline code.

```
        OPEN(UNIT=XX,FILE=INPUT)
        READ(XX,*) i-index, j-index
        READ(XX,*) flow solver parameters
        READ(XX,*) grid adaptation parameters
        READ(XX,*) flow field reference values
        READ(XX,*) RADINT,RADREAD,IMETHOD,ISTAG,RADITV,RADOUT
        READ(XX,*) i/o parameters
        CLOSE(XX)

!       RADINT  = X    !1 = radiation solver  on
!       RADREAD = X    !1 = read prev rad soln
!       IMETHOD = X    !0 = Tangent Slab Solver; 0 = FVMR
!       ISTAG   = X    !1 = Perform stagnation line calculations
!       RADITV  = X    !N = Num iters b/w calls to rad_solver
!       RADOUT  = X    !1 = output rad solution for restart
```

Table 12. Call to Radiation Solver within Main Loop

Program *main*; bold text indicates modifications to baseline code; pseudo-code.

```
!     MAIN LOOP

      DO N=NSTART,NEND
         CALL subroutine_1
         CALL subroutine_2
         CALL subroutine_3
         NTIME=NTIME+DT
         CALL subroutine_4
         IF(RADINT.eq.1)THEN
               IF(MOD(N,INT(RADITV)).eq.0 .and. (N.NE.NEND))THEN
               write(*,*) 'call rad_solver'
                CALL RAD_SOLVER(limits,X,Y,T,T_vib_s,rho_i,c_i,parameters)
               ENDIF

        END IF
        IF((INT_5.eq.1).and.(INT_7a.eq.1))THEN
                IF(INT_8.eq.0)THEN
                CALL subroutine_5
                ENDIF
         ENDIF
      END DO
```

Table 13. Calculation of Source Terms

Subroutine *source*; pseudo-code

```
!     *****source terms due to radiation
      if(radint.eq.1)then
      du_ev_O2 = du_ev_O2-DTDG*Q_rad_O2
      du_ev_N2 = du_ev_N2-DTDG*Q_rad_N2
      du_ev_NO = du_ev_NO-DTDG*Q_rad_NO
      du_eel   = du_eel  -DTDG*Q_rad_el
      du_tot   = du_tot  -DTDG*Q_rad_tot
      end if
```

Table 14. Common Block Used by *main* and *rad_solver*

Common Block *rad_comon*

```
!*****Variable belonging to common block /rad/*****************************
       integer :: imech, nmech
       character(4)  :: mech_name(68)
       real*8, pointer :: spect_emis(:,:),spect_absb(:,:),alpha_vib(:,:)
       real*8, pointer :: wave_length(:)
       common/rad/spect_emis, spect_absb,wave_length,nmech,mech_name,alpha_vib
!***********************************************************************
!*****Variable belonging to common block /radsoln/*******************
        real*8, pointer :: tot_emis(:,:,:), tot_absb(:,:,:)
        real*8, pointer :: spect_emis_m(:,:,:,:), spect_absb_m(:,:,:,:)
        real*8, pointer :: wave_length_m(:,:,:),alpha_vib_m(:,:,:,:)
         real*8, pointer :: Q_rad_tot(:,:,:)
        real*8, pointer :: norm_int(:,:,:,:)
        real*8, pointer :: Q_rad_s(:,:,:)
        real*8, pointer :: Q_rad_vib(:,:,:) Ni_O2(:,:,:) ,Ni_N2(:,:,:), Ni_NO(:,:,:),
     1  Ni_N(:,:,:), Ni_O(:,:,:)
       common/radsoln/norm_int,Q_rad_tot,Q_rad_s,Q_rad_vib, tot_emis,tot_absb,
     1  Ni_O2, Ni_N2, Ni_NO, Ni_N, Ni_O
!*********************************************************************
```

Table 15. Calculate *nmech* and Store Values for *mech_name*

Module *rad_parameters*

```
       nmech = 1
       mech_name(1) = 'Tot.'
       do i=1,18
              if(atom_rads(1,i).ne.'  '.and.atom_rads(2,i).eq.'bb') then
              nmech = nmech + 1
              mech_name(nmech) = atom_rads(1,i)
              end if
       end do
       do i=1,40
              if(diatom_bands(1,i).ne.'    ') then
              nmech = nmech + 1
              mech_name(nmech) = diatom_bands(2,i)
               end if
       end do
```

Table 16. Control Sequence for Executing Subroutines Local to *rad_solver*

Subroutine *rad_solver*

```
!       CALL RTE SOLUTION ALGORITHM
        if(METHODINT.eq.1)then
!               write(*,*) 'called rad_TS'
                call rad_TS(STAGINT,ILD,JLD,X,Y,T,TvN2,TvO2,TvNO,TvNOpl,Tel,              &
     &  numN2, numO2, numN, numO,numNO,numNOpl, numel,numatom,nummol,numhvy,molwt)
        else
!               write(*,*) 'called rad_FVM'
!               call rad_FVM(STAGINT,ILD,JLD,X,Y,T,TvN2,TvO2,TvNO,TvNOpl,Tel,
&
!     &  numN2, numO2, numN, numO,numNO,numNOpl, numel,numatom,nummol,numhvy,molwt)
       end if
!*************************************************************************
!       CALL SOURCE TERM ALGORITHM

        call rad_couple(ILD,JLD) (See Table 27)

        write(*,*) 'exiting rad_solver'
        RETURN
        CONTAINS
```

Table 17. Basic Outline of Tangent Slab Radiation Solver; *important aspects of the subroutine rad_TS are further described in the tables indicated below.*

Subroutine *rad_TS*

```
      subroutine rad_TS

      -Declare Variables
      -Initialize Variables

      do i=1,ILD
      do dir=1,2

      spect_int = 0.0
      spect_int_old = 0.0


      do j=a,b,increment
      -Calculate emis and absb (See Table 18)
      do imech=1,nmech
      -Calculate intensity (See Table 19)
      -Calculate source terms for idir (See Table 22)
      end do !over imech

      end if

      -Calculate total intensity (See Table 21)

      end do !over j

      -Calculate total source terms (See Table 22)

      end do !over dir

      END DO

      end subroutine rad_TS
```

Table 18. Calculate Emission and Absorption Coefficients

Subroutine *rad_TS*

```
    if(dir.eq.1)then
         call radipac(0.0,nnode,0.0,method,0.0,0.0,0.0, &
     &   wavmin,wavmax,nwave,avg_num,&
     &   atom_noneqs, atom_rads, diatom_noneqs, diatom_bands,triatom_bands,&
     &   T(i,j),T(i,j),TvN2(i,j),Tel(i,j),TvO2(i,j),TvN2(i,j),TvNO(i,j),&
     &   0.0,0.0,0.0,0.0,0.0,0.0,0.0,0.0,0.0,0.0,0.0,&
     &   numN(i,j),numN2(i,j),numN2p(i,j),numel(i,j),numNO(i,j),numNp(i,j),&
     &   numO(i,j),numO2(i,j),0.0,numOp(i,j),numhvy(i,j),numatom(i,j),nummol(i,j),&
     &   molwt(i,j),Ni_O2(:,i,j),Ni_N2(:,i,j),Ni_NO(:,i,j),Ni_N(:,i,j),Ni_O(:,i,j))!,

         spect_emis_m(:,:,i,j) = spect_emis
         spect_absb_m(:,:,i,j) = spect_absb
         wave_length_m(:,i,j) = wave_length
         alpha_vib_m(:,:,i,j) = alpha_vib
    end if

       spect_emis_m(1,:,i,j) = 0.0D0
       spect_absb_m(1,:,i,j) = 0.0D0

       do imech=2,nmech
       spect_emis_m(1,:,i,j) = spect_emis_m(1,:,i,j) + spect_emis_m(imech,:,i,j)
       spect_absb_m(1,:,i,j) = spect_absb_m(1,:,i,j) + spect_absb_m(imech,:,i,j)
       end do

       if(Tel(i,j) .lt. 2000.0D0)then
       !spect_emis_m(:,:,i,j) = 0.0D0
       spect_absb_m(:,:,i,j) = 0.0D0
       end if
```

Table 19. Calculate Spectral and Normal Intensities

Subroutine *rad_TS*

```
       spect_int_old=spect_int

       do imech = 1, nmech
             do m = 1,nwave
                      if(depth*spect_absb_m(imech,m,i,j).gt.1.0e-4) then
                       blam=spect_emis_m(imech,m,i,j)/spect_absb_m(imech,m,i,j)
                       spect_int(imech,m,dir)=blam-(blam-spect_int_old(1,m,dir))*&
                         & exp(-spect_absb_m(imech,m,i,j)*depth)
                  else
                        spect_absb_m(imech,m,i,j) = 0.0
                      spect_int(imech,m,dir) = spect_int_old(1,m,dir) +
spect_emis_m(imech,m,i,j)*depth
                end if
                spect_int(imech,m,dir)=spect_int(imech,m,dir)-spect_int_old(1,m,dir)
                spect_int(imech,m,dir)=spect_int_old(imech,m,dir)+spect_int(imech,m,dir)
                if(spect_emis_m(imech,m,i,j).lt.1.0E-20) spect_emis_m(imech,m,i,j) =
0.0D0
             end do

      !Calculate Normal Intensities
      call
simpson(norm_int(imech,i,j,dir),wave_length_m(:,i,j),spect_int(imech,:,dir),nwave,ier)
      norm_int(imech,i,j,dir) = norm_int(imech,i,j,dir)*1.0e-4
```

Table 20. Calculate Partial Source Terms; Calculate Spectral Coefficients

Subroutine *rad_TS*

```
       !Calculate Source Terms
      net_emis(imech,:) = spect_emis_m(imech,:,i,j)-
spect_absb_m(imech,:,i,j)*spect_int(imech,:,dir)
      call simpson(Q_rad_dir(imech,i,j),wave_length_m(:,i,j),net_emis(imech,:),nwave,ier)
      Q_rad_dir(imech,i,j)  =         Q_rad_dir(imech,i,j)*1.0e-4

      !Calculate Vibrational Source Terms
      !net_emis_vib(imech,:) = alpha_vib_m(imech,:,i,j)*net_emis(imech,:)
      !call
simpson(Q_vib_dir(imech,i,j),wave_length_m(:,i,j),net_emis_vib(imech,:),nwave,ier)
      !Q_vib_dir(imech,i,j) = Q_vib_dir(imech,i,j)*1.0e-4

      if(dir.eq.1)then

        !Calculate Total Emisssion Coefficient
        call
simpson(tot_emis(imech,i,j),wave_length_m(:,i,j),spect_emis_m(imech,:,i,j),nwave,ier)
        tot_emis(imech,i,j)=tot_emis(imech,i,j)*1e-4

        !Calculate Total Absorption Coefficient
        call
simpson(tot_absb(imech,i,j),wave_length_m(:,i,j),spect_absb_m(imech,:,i,j),nwave,ier)
        tot_absb(imech,i,j)=tot_absb(imech,i,j)*1e-4
```

Table 21. Calculate Total Intensities

Subroutine *rad_TS*

```
    !Cacluate Total Intensities
         spect_int(1,:,dir)=0.0
         norm_int(1,i,j,dir)=0.0
      do imech=2,nmech
         norm_int(1,i,j,dir)=norm_int(1,i,j,dir)+norm_int(imech,i,j,dir)
         spect_int(1,:,dir)=spect_int(1,:,dir)+spect_int(imech,:,dir)
      end do
```

Table 22. Calculate Source Terms

Subroutine *rad_TS*

```
   do idir = 1,ndir

   ...

      Q_rad_tot(:,:,:) = Q_rad_tot(:,:,:) + 4*pi/real(ndir)*Q_rad_dir(:,:,:)
      Q_rad_vib(:,:,:) = Q_rad_vib(:,:,:) + 4*pi/real(ndir)*Q_vib_dir(:,:,:)

   ...

   end do
```

Table 23. Basic Outline of Finite Volume Method Radiation Solver*; important aspects of the subroutine rad_FVM are further described in the tables indicated below.*

Subroutine *rad_FVM*

```
subroutine rad_FVM(PARAMETERS,X,Y,T,Tv_1,Tv_2,...,Tel,nums,molwt)

    -Declare variables

    -Initialize variables

    -Calculate emis, absb

 do imech=1,nmech
   do idir = 1,ndir

    -Calculate LHS Matrix and RHS vector (See Table 24)
    -Enforce BCs    (See Table 25)

    -Solve Linear System  (See Tables 26 and 27)

 end do !idir
 end do !imech

     -Calculate source terms
 end subroutine
```

Table 24. Calculate _view factor' Matrix (LHS) and Source Term Vector (RHS)

Subroutine *rad_FVM*

```
    do i_region=2,1,-1

     do i=2,ILD
     do j=1,JLD

        if(i_region.eq.1)then
        ij=int( (i-2)*JLD + j + (ILD-1)*JLD )
        else
        ij=int( (ILD-i)*JLD + j )
        end if

        do kdir=1,4

 !***CALCULATE LHS MATRIX  (DIAGONAL ELEMENTS)

       if(dot_prod(i,j,idir,kdir,i_region).lt.0.0) then

        SELECT CASE(kdir)
        CASE(1)
        F_PENTA(1,ij)=F_PENTA(1,ij)-abs(dot_prod(i,j,idir,1,i_region))
        CASE(2)
        E_PENTA(1,ij)=E_PENTA(1,ij)-abs(dot_prod(i,j,idir,2,i_region))
        CASE(3)
        C_PENTA(1,ij)=C_PENTA(1,ij)-abs(dot_prod(i,j,idir,3,i_region))
        CASE(4)
        A_PENTA(1,ij)=A_PENTA(1,ij)-abs(dot_prod(i,j,idir,4,i_region))
        END SELECT

        else
        D_PENTA(1,ij)=D_PENTA(1,ij)+abs(dot_prod(i,j,idir,kdir,i_region))
        end if

        end do !kdir

        if(idir.eq.3)then
        D_PENTA(1,ij)=D_PENTA(1,ij)+2.0D0*abs(dot_prod(i,j,idir,5,i_region))
        end if

!***CALCULATE RHS VECTOR
        !if(imech.eq.1)then
        !B_PENTA(1,ij) = spect_emis_m(imech,:,i,j)*vol(i,j)*n_dir(idir,4)
        !else
        !B_PENTA(1,ij) = spect_emis_m(imech,:,i,j)*vol(i,j)*n_dir(idir,4)-&
      !& spect_int(1,:,i,j,idir)*spect_absb_m(imech,:,i,j)*vol(i,j)*n_dir(idir,4)
        !end if

        if(imech.eq.1)then
        B_PENTA(1,ij) = tot_emis(imech,i,j)*vol(i,j)*n_dir(idir,4)
        else
        B_PENTA(1,ij) = tot_emis(imech,i,j)*vol(i,j)*n_dir(idir,4)- &
                      & norm_int(1,i,j,idir)*tot_absb(imech,i,j)*vol(i,j)*n_dir(idir,4)
        end if

!***FINISH LHS MATRIX

        D_PENTA(1,ij)=D_PENTA(1,ij)+tot_absb(imech,i,j)*vol(i,j)*n_dir(idir,4)

     end do !j
     end do ! i

     end do !i region
```

Table 25. Enforce Boundary Conditions

Subroutine *rad_FVM*

```
!Outflow
if(i.eq.ILD .and. i_region.eq.1)then
B_PENTA(1,ij) = B_PENTA(1,ij)
D_PENTA(1,ij) = D_PENTA(1,ij)
F_PENTA(1,ij) = 0.0D0
C_PENTA(1,ij) = C_PENTA(1,ij)
A_PENTA(1,ij) = A_PENTA(1,ij)
E_PENTA(1,ij) = E_PENTA(1,ij)

!Outflow
if(i.eq.ILD .and. i_region.eq.2)then
B_PENTA(1,ij) = B_PENTA(1,ij)
D_PENTA(1,ij) = D_PENTA(1,ij)
F_PENTA(1,ij) = F_PENTA(1,ij)
C_PENTA(1,ij) = C_PENTA(1,ij)
A_PENTA(1,ij) = A_PENTA(1,ij)
E_PENTA(1,ij) = 0.0D0

!Wall
if(j.eq.1)then
B_PENTA(1,ij) = B_PENTA(1,ij)
D_PENTA(1,ij) = D_PENTA(1,ij)
F_PENTA(1,ij) = F_PENTA(1,ij)
C_PENTA(1,ij) = C_PENTA(1,ij)
A_PENTA(1,ij) = 0.0D0
E_PENTA(1,ij) = E_PENTA(1,ij)
end if

!Inflow
if(j.eq.JLD)then
B_PENTA(1,ij) = B_PENTA(1,ij)
D_PENTA(1,ij) = D_PENTA(1,ij)
F_PENTA(1,ij) = F_PENTA(1,ij)
C_PENTA(1,ij) = 0.0D0!
A_PENTA(1,ij) = A_PENTA(1,ij)
E_PENTA(1,ij) = E_PENTA(1,ij)
end if
```

Table 26. Call Linear Solver; Respecify Solution in Terms of Global Discretization Indices

Subroutine *rad_FVM*

```
    call band(B_PENTA,E_PENTA,A_PENTA,D_PENTA,C_PENTA, &
            & F_PENTA,2*int(JLD)+1,npenta,nmech,nwave)

    do j=1,JLD
       do i=2,ILD

       ij=int( (i-2)*JLD + j + (ILD-1)*JLD )
       norm_int(imech,i,j,idir) = B_PENTA(1,ij)

       if(idir.eq.3)then
       ij=int( (i-2)*JLD + j + (ILD-1)*JLD )
       norm_int(imech,i,j,3) = B_PENTA(1,ij)

       ij=int( (ILD-i)*JLD + j )
       norm_int(imech,i,j,4) = B_PENTA(1,ij)
       end if

       end do

       norm_int(imech,1,j,idir) = norm_int(imech,2,j,idir)
       norm_int(imech,1,j,4) = norm_int(imech,2,j,4)

    end do
```

Table 27. Linear Solver Used for Implicit FVMR Scheme

Subroutine *band*

```
subroutine band(B,E,A,D,C,F,M,N,nmech,nwave)

      implicit none
      integer :: nmech,nwave,iwave,ia,ib
      real*8 :: E(N),A(N),D(N),C(N),F(N),&
                     !& B(nwave,N)
                     & B(N)

      integer g,h,i,j,k,m,n,r
      real*8 :: aa(n,m)
      real*8 :: eps

      write(*,*) 'in band'

      nwave = 1 !added for FVM mod
      iwave = 1 !added for FVM mod

      r = (m+1)/2
      eps = 1.0D-10

      aa=0.0D0

      aa(:,1  )=E
      aa(:,r-1)=A
      aa(:,r  )=D
      aa(:,r+1)=C
      aa(:,m  )=F

      do 20 k = 1,n
!      if( abs (aa(k,r)) .le. eps)
        aa(k,r) = 1.0D0/aa(k,r)
       h = r-1
       i = k+1
10     if(h.lt.1 .or. j .gt. n) goto 20
```

```
        aa(i,h) = aa(i,h)*aa(k,r)
                j = h+1
                g = r+1
30              if(g.gt.m .or. j.gt.(r+n-i) ) goto 40
                aa(i,j) = aa(i,j) - aa(i,h)*aa(k,g)
                j = j+1
                 g = g+1
                 goto 30
40      continue
        i=i+1
        h=h-1
        goto 10

20     continue

       do i=1,n
       write(69,*) (aa(i,j), j=r-1,r+1)
       end do

!      Forward Elimination


       do 100 k = 1,n-1
        i=k+1
        j=r-1
110     if(j.lt.1 .or. i.gt.n) goto 100
         !do iwave = 1,nwave
        !b(iwave,i) = b(iwave,i) - aa(i,j)*b(iwave,k)
        b(i) = b(i) - aa(i,j)*b(k)
         !end do
        i = i+1
        j = j-1
        goto 110
100    continue


!      Back Substitution

        do 120 k = n,1,-1
                i=k+1
                j=r+1
130             if(j.gt.m .or. i.gt.n) goto 140
                !do iwave = 1,nwave
                !b(iwave,k) = b(iwave,k) - aa(k,j)*b(iwave,i)
                !end do
                b(k) = b(k) - aa(k,j)*b(i)
                i=i+1
                j=j+1
                goto 130
140     continue
         !do iwave = 1,nwave
        !b(iwave,k) = b(iwave,k)*aa(k,r)
        b(k) = b(k)*aa(k,r)

         !if(abs(b(iwave,k)) .lt. 1.0D-14) b(iwave,k)=0.0D0

         !end do

120     continue


       end subroutine band
```

Table 28. Calculate Source Terms for Flow Solver

Subroutine *rad_couple*

```
        subroutine rad_couple(ILD,JLD)

        use rad_parameters
        use rad_vars


        !Q_rad_s(1,i,j) = total E rad source term
        !Q_rad_s(2,i,j) = O2   Evib rad source term
        !Q_rad_s(3,i,j) = N2   Evib rad source term
        !Q_rad_s(4,i,j) = NO   Evib rad source term

!Calculate Source Terms
        do iatoms=1,18
        if(atom_rads(1,iatoms).ne.'  ')then
               do imech=1,nmech
                !Calculate source term for E
                if(atom_rads(1,iatoms).eq.mech_name(imech))then
               Q_rad_s(1,:,:) = Q_rad_s(1,:,:) + Q_rad_tot(imech,:,:)
                end if
                end do
        end if
        end do

        do iatoms=1,40
        if(diatom_bands(1,iatoms).ne.'    ')then
               do imech=1,nmech
                !Calculate source term for E
                if(diatom_bands(1,iatoms).eq.mech_name(imech))then
               Q_rad_s(1,:,:) = Q_rad_s(1,:,:) + Q_rad_tot(imech,:,:)

                !Calculate source term for Evib_O2
                if((diatom_bands(1,iatoms).eq.'O2  ').and.
(diatom_bands(2,iatoms).ne.'cont'))then
               Q_rad_s(2,:,:) = Q_rad_s(2,:,:) + Q_rad_vib(imech,:,:)
                end if

                !Calculate source term for Evib_N2
                if((diatom_bands(1,iatoms).eq.'N2  ').and.
(diatom_bands(2,iatoms).ne.'cont'))then
               Q_rad_s(3,:,:) = Q_rad_s(3,:,:) + Q_rad_vib(imech,:,:)
                end if

                !Calculate source term for Evib_NO
                if((diatom_bands(1,iatoms).eq.'NO  ').and.
(diatom_bands(2,iatoms).ne.'cont'))then
               Q_rad_s(4,:,:) = Q_rad_s(4,:,:) + Q_rad_vib(imech,:,:)
                end if

                end if
                end do
        end if
        end do

        write(*,260) maxval(Q_rad_s)
260     format('maxval(Q_rad_s)=',1pe10.3,'W/m3')

        end subroutine
```

Table 29. Assign Local Variables to Shared Variables

Subroutine *radipac*

```
    call emis_absb  (See Table 30)

    spect_emis(1,:)=spect%emis
    spect_absb(1,:)=spect%absb
    do isp=1,num_diatoms
    if(diatoms(isp)%name.eq.'N2') Ni_N2 = diatoms(isp)%state_pop
    if(diatoms(isp)%name.eq.'O2') Ni_O2 = diatoms(isp)%state_pop
    if(diatoms(isp)%name.eq.'NO') Ni_NO = diatoms(isp)%state_pop
    end do

    do isp=1,num_atoms
    if(atoms(isp)%name.eq.'N') Ni_N = atoms(isp)%state_pop
    if(atoms(isp)%name.eq.'O') Ni_O = atoms(isp)%state_pop
    end do
```

Table 30. Calculate Species Contributions to Spectral Coefficients

Subroutine *emis_absb*; indicates modifications to baseline code.

```
! bound-bound radiation; atomic (See Table 32)
      ibb = 0
      do i=1,18
        if((atoms(isp)%name.eq.atom_rads(1,i)).and.(atom_rads(2,i).eq.'bb'))then
        ibb = 1
!        write(*,*) 'ibb=',ibb
         do j=1,nmech
               if(mech_name(j).eq.atom_rads(1,i)) then
                imech=j
!              write(*,*) 'imech=', j, 'mech_name=',mech_name(j)
               end if
         end do
        end if
      end do

      if(ibb.eq.1) then
        if(atoms(isp)%name.ne.'H ') call atom_bb(isp, atoms, t, spect,imech)
        if(atoms(isp)%name.eq.'H ') call h_bb(isp, atoms, t, spect)
      end if

! bound-bound radiation; diatomic (See Table 33)
      ibb = 0
      do i=1,40

if((diatoms(isp)%name.eq.diatom_bands(1,i)).and.(diatom_bands(2,i).ne.'cont'))then
         ibb = 1
         do j=1,nmech
               if(mech_name(j).eq.diatom_bands(2,i)) then
                imech=j
!              write(*,*) 'imech=', imech, 'mech_name=',mech_name(imech)
               end if
         end do
        end if
      end do
      if(ibb.eq.1) call diatom_bb(isp, diatoms, dens, t, spect, diatom_bands,imech)
```

Table 31. Assign Nonequilibrium Temperatures and Number Densities

Subroutine *emis_absb*

```
 !Assign Temps an Num Densities; diatomic sp

      if(diatoms(isp)%name.eq.'N2  ') then
        t(isp)%vib%val = tvib_N2(inode)
        diatoms(isp)%dens_diatom = 1.0e-6 * concN2(inode)
        diatoms(isp)%dens_atom1 = 1.0e-6 * concN(inode); diatoms(isp)%dens_atom2 = &
  &       1.0e-6 * concN(inode)
      endif

      if(diatoms(isp)%name.eq.'NO  ') then
        diatoms(isp)%dens_diatom = 1.0e-6 * concNO(inode)
        t(isp)%vib%val = tvib_NO(inode)
        diatoms(isp)%dens_atom1 = 1.0e-6 * concN(inode); diatoms(isp)%dens_atom2 = &
  &       1.0e-6 * concO(inode)
      endif
      if(diatoms(isp)%name.eq.'O2  ') then
         t(isp)%vib%val = tvib_O2(inode)
        diatoms(isp)%dens_diatom = 1.0e-6 * concO2(inode)
        diatoms(isp)%dens_atom1 = 1.0e-6 * concO(inode); diatoms(isp)%dens_atom2 = &
  &       1.0e-6 * concO(inode)
      endif
```

Table 32. Calculate Bound-Bound Radiation from Atomic Species

Subroutine *atom_bb*; indicates modifications to baseline code.

```
!*****Variable belonging to common block /rad/*****************************************
        integer :: imech, nmech
        character(4)  :: mech_name(68)
        real*8, pointer :: spect_emis(:,:),spect_absb(:,:),alpha_vib(:,:)
        real*8, pointer :: wave_length(:)
        common/rad/spect_emis, spect_absb,wave_length,nmech,mech_name,alpha_vib
!*******************************************************************************************
      do m = nstart,nend
        dlam = 1.0d0/(1.0d0/spect%min - spect%itv * (ncentr - 1.0d0))
&
  &      - 1.0d0/(1.0d0/spect%min - spect%itv * (m - 1.0d0))
        emission = e *(((1.0d0-widthl/widthv) * exp(-2.772*(dlam/widthv)**2)+        &
  &       (widthl/widthv)/(1.0d0+4.0d0*(dlam/widthv)**2.0d0) + 0.016d0*(widthl/widthv)*
&
  &       (1.0d0-widthl/widthv)*(exp(-0.4d0*(abs(dlam)/widthv)**2.25d0) - 10.0d0/
&
  &       (10.0d0+(abs(dlam)/widthv)**2.25d0)))/denom)
        spect%emis(m) = spect%emis(m) + emission
        blam = 1.1904d-16 * ax/((1.0d-8*spect%wavel(m))**5.0d0*(1.0d0 - ax))
        spect%absb(m) = spect%absb(m) + emission/blam
                spect_emis(imech,m)=emission
                spect_absb(imech,m)=emission/blam
      end do !over m
```

Table 33. Calculate Bound-Bound Radiation from Diatomic Species

Subroutine *diatom_bb*; indicates modifications to baseline code.

```
!*****Variable belonging to common block /rad/*****************************************
       integer :: imech, nmech
       character(4)  :: mech_name(68)
       real*8, pointer :: spect_emis(:,:),spect_absb(:,:),alpha_vib(:,:)
       real*8, pointer :: wave_length(:)
       common/rad/spect_emis, spect_absb,wave_length,nmech,mech_name,alpha_vib
!*******************************************************************************

!   Sigma(upper)-Sigma(lower) transition
          if((diatoms(isp)%di_lev( diatoms(isp)%di_line(tr)%up_state )%lambda.eq.0) &
  &         .and.(diatoms(isp)%di_lev( diatoms(isp)%di_line(tr)%lo_state )%lambda   &
  &         .eq.0)) then
!           r-branch (j+1->j)
            do j = 1,maxj
              s_jj = real(j, prec)
              call calc_diatomic_bb(isp, diatoms,&
                & dev, bvu, bvl, dvu, dvl, geu, teu, evu, qtot, re1,                &
                & j, s_jj, 'r', spect, wavelx, emisj, ncentr)
!
!             duplicate line profile of band origin
              do m = -nspred,nspred
                if((ncentr(j)+m.gt.0).and.(ncentr(j)+m.le.spect%wave_num)) then
                  emission = emisj(j) * y(m)
                  ax = exp(- 1.43877*1.0e8/(spect%wavel(ncentr(j)+m)*               &
  &                 t(isp)%el_tr%val))
                  blam = 1.1904e-16 * ax/((1.0e-8*spect%wavel(ncentr(j)+m))**5*     &
  &                   (1.0 - ax))
                  absorption = emission/blam
                  alpha_vib(imech,m) = exp(-1.43877*evu/t(isp)%vib%val)/qtot
                  spect_emis(imech,ncentr(j)+m)=emission
                  spect_absb(imech,ncentr(j)+m)=absorption
                  spect%emis(ncentr(j) + m) = spect%emis(ncentr(j) + m) + emission
                  spect%absb(ncentr(j) + m) = spect%absb(ncentr(j) + m) + absorption
                end if
              enddo
            end do
```

This modification repeated for other transition types (i.e., S-P, P-S, P-P).

Appendix B: State Populations

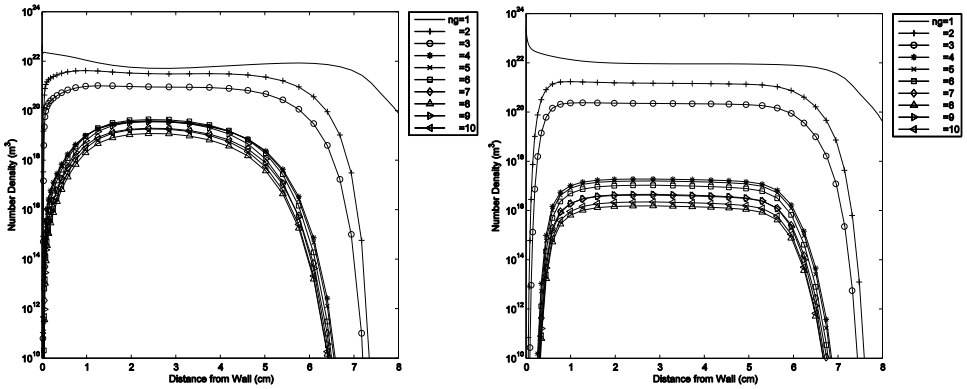

Figure 20. a) State Populations of N, 1634.0 seconds *(left uncoupled, right coupled)*

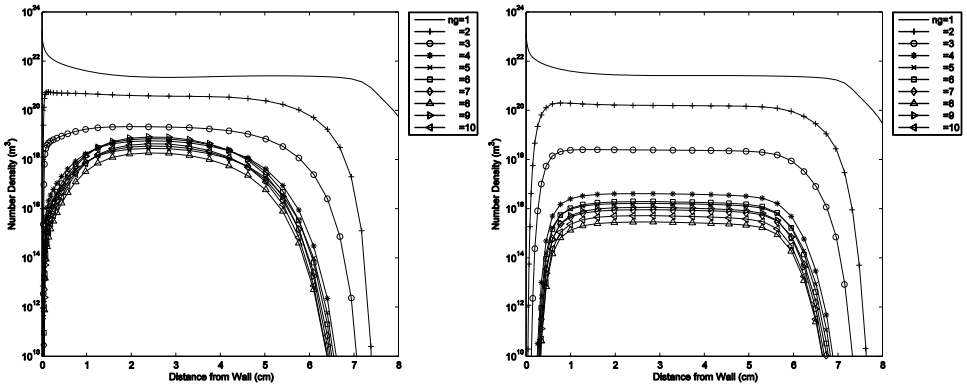

Figure 20. b) State Populations of O, 1634.0 seconds *(left uncoupled, right coupled)*

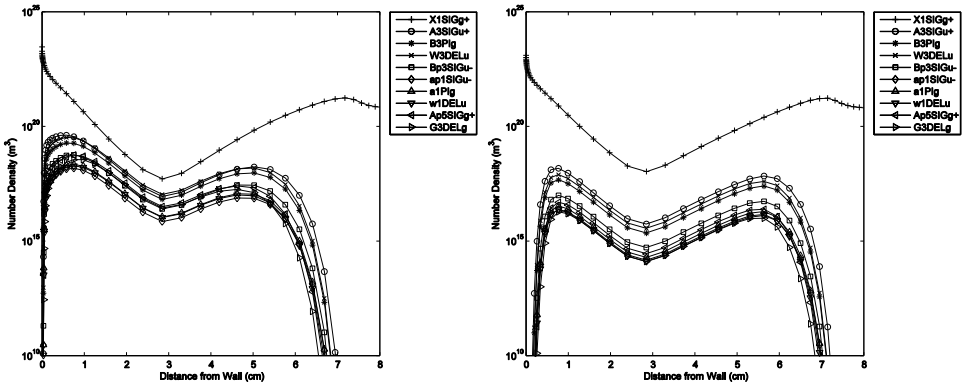

Figure 20. c) State Populations of N_2, 1634.0 seconds *(left uncoupled, right coupled)*

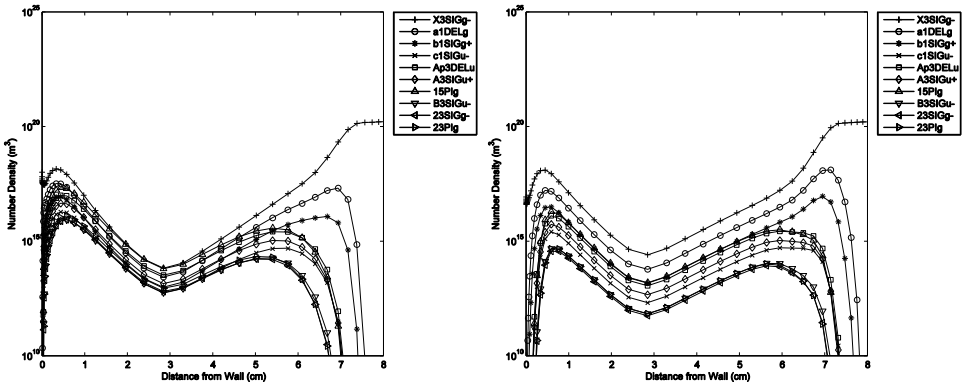

Figure 20. d) State Populations of O_2, 1634.0 seconds *(left uncoupled, right coupled)*

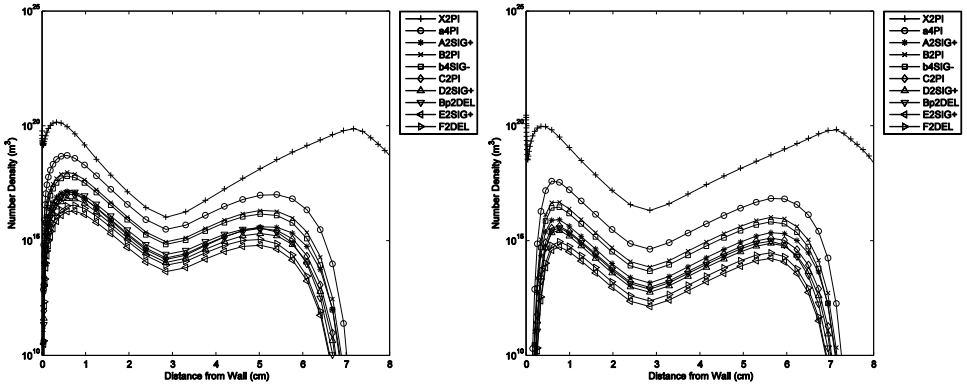

Figure 20. e) State Populations of NO, 1634.0 seconds *(left uncoupled, right coupled)*

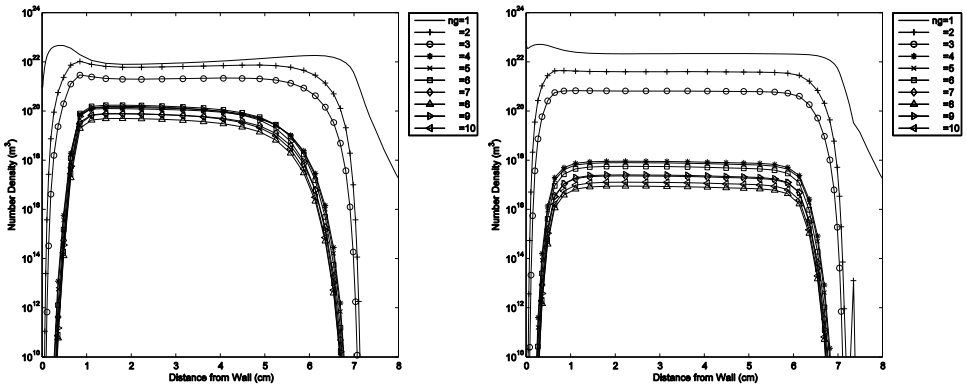

Figure 21. a) State Populations of N, 1636.0 seconds *(left uncoupled, right coupled)*

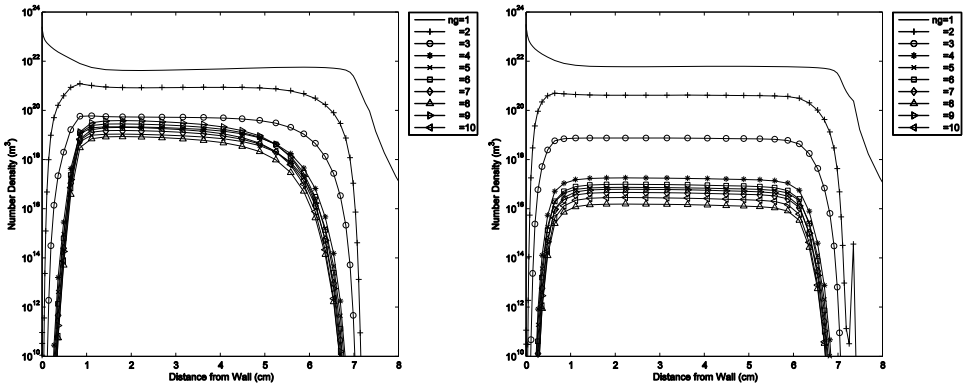

Figure 21. b) State Populations of O, 1636.0 seconds *(left uncoupled, right coupled)*

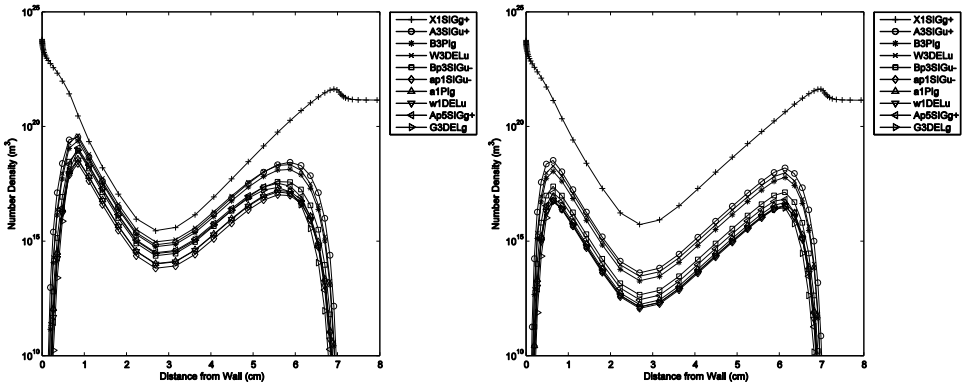

Figure 21. c) State Populations of N_2, 1636.0 seconds *(left uncoupled, right coupled)*

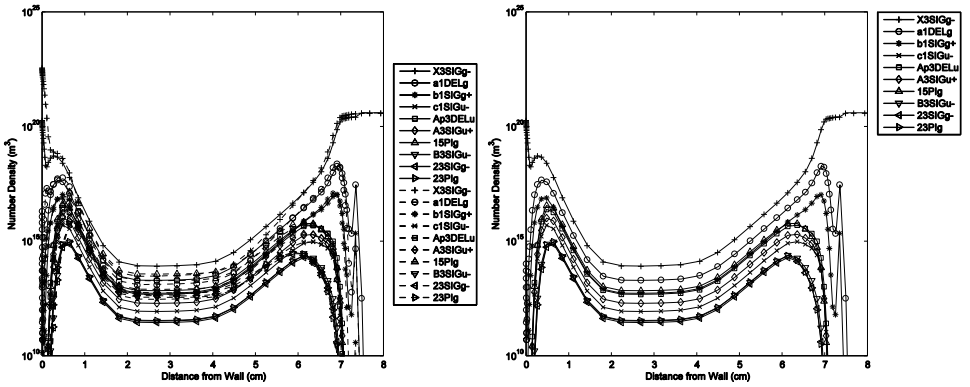

Figure 21. d) State Populations of O_2, 1636.0 seconds *(left uncoupled, right coupled)*

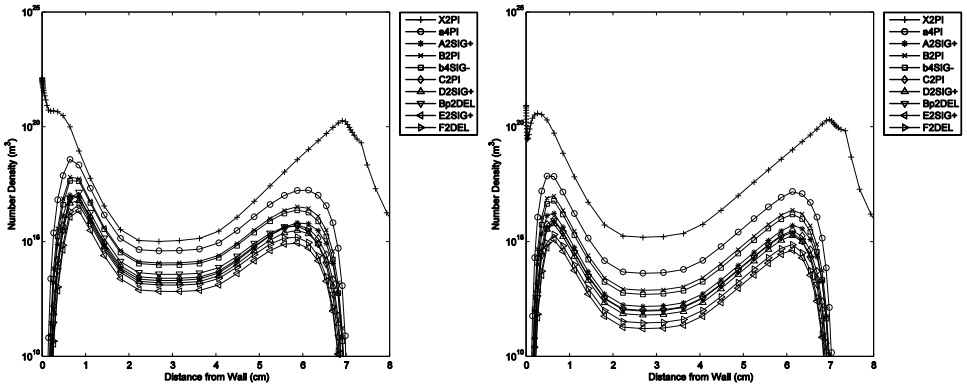

Figure 21. e) State Populations of NO, 1636.0 seconds *(left uncoupled, right coupled)*

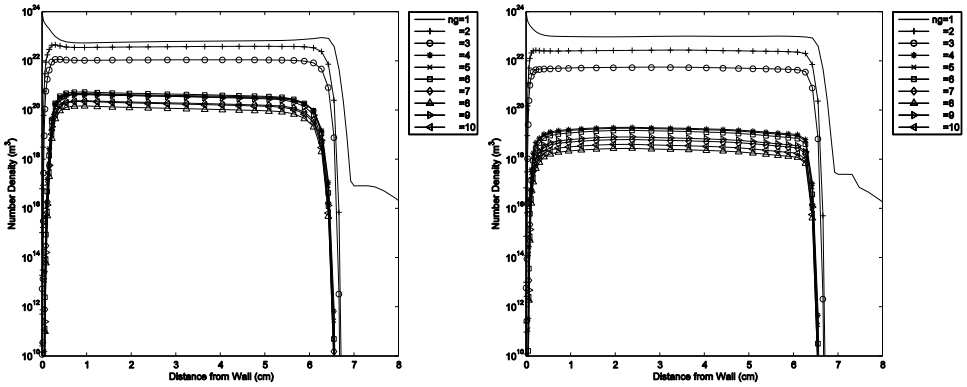

Figure 22. a) State Populations of N, 1640.5 seconds *(left uncoupled, right coupled)*

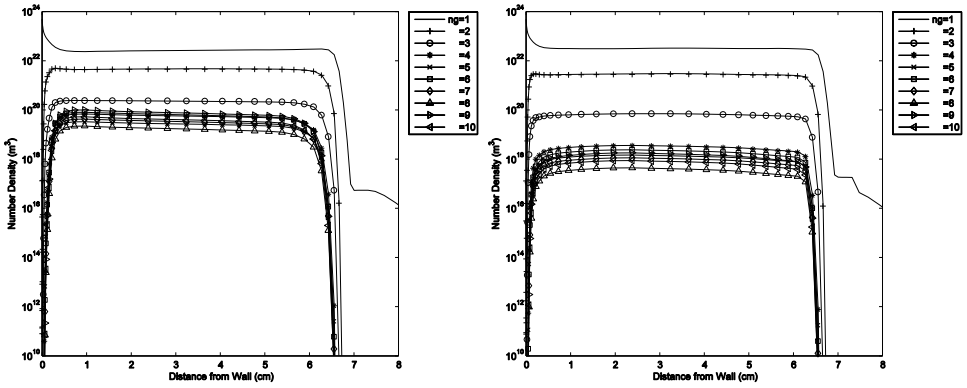

Figure 22. b) State Populations of O, 1640.5 seconds *(left uncoupled, right coupled)*

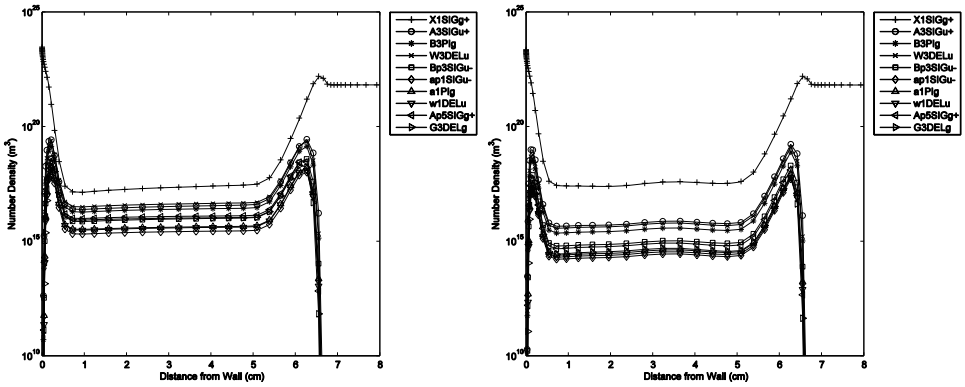

Figure 22. c) State Populations of N_2, 1640.5 seconds *(left uncoupled, right coupled)*

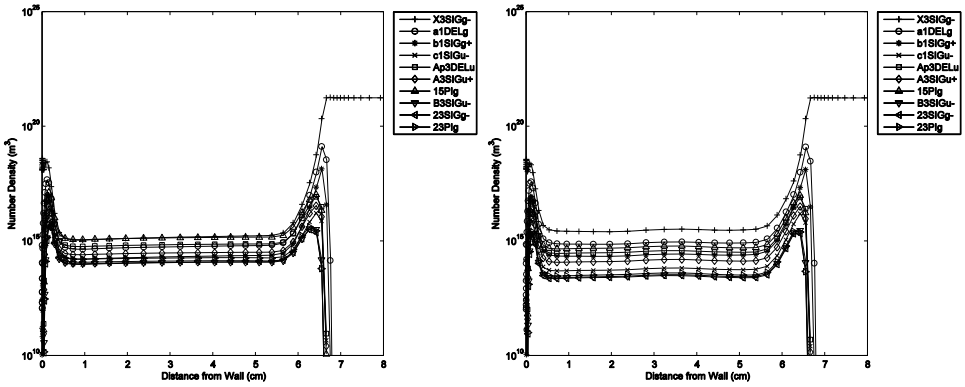

Figure 22. d) State Populations of O_2, 1640.5 s *(left uncoupled, right coupled)*

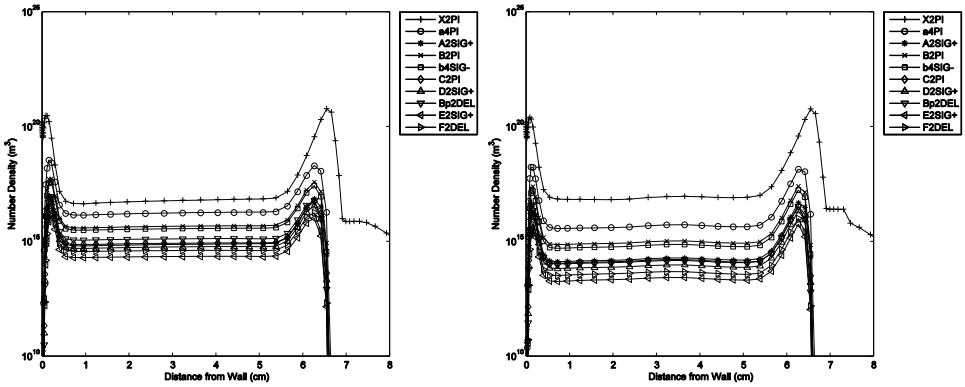

Figure 22. e) State Populations of NO, 1640.5 s *(left uncoupled, right coupled)*

Bibliography

Ali, A. W., "Excitation and Ionization Cross-Sections for Electron Beam and Microwave Energy Deposition in Air," NRL Memorandum Report 459780, Naval Research Laboratory, 1981.

Anderson, J. D., Jr., "A Survey of Modern Research in Hypersonic Aerodynamics," AIAA-1984-1578, AIAA 17th Fluid Dynamics, Plasma Dynamics, and Lasers Conference, Snowmass, CO, June, 1984.

Anderson, J. D., Jr., Hypersonics and High-Temperature Gas Dynamics, AIAA Education Series, AIAA, Reston, VA, 2006.

Appleton, J., and Bray, K., "The Conservation Equations for a Nonequilibrium Plasma," Journal of Fluid Mechanics, Vol. 20, No. 4, 1964, pp.659-672.

Arnold, J. O., Cooper, D. M., Park, C., and Prakash, S. G., "Line-by-line Transport Calculations for Jupiter Entry Probes," in Entry Heating and Thermal Protection, Progress in Astronautics and Aeronautics, Vol. 69, W.B. Olstad, ed., 1980, pp. 52-82.

Barnes, J. E., "Flights of Fancy Meet Air Force Scientist," L.A. Times, 26 March, 2010.

Berman, H.A., Anderson, John D., Jr., and Drummond, J. P., "Supersonic Flow over a Rearward Facing Step with Transverse Nonreacting Hydrogen Injection," AIAA Journal, Vol. 21, No. 12, December, 1983, pp. 1707.

Bertin, J.J., Hypersonic Aerothermodynamics, AIAA Education Series, Washington, 1994.

Bird, G. A., Molecular Gas Dynamics and the Direct Simulation of Gas Flows, Claredon, Oxford, 1994.

Bird, R. B., Stewart, W. E., and Lightfoot, E. N., Transport Phenomena, Wiley, New York, 1960.

Blackman, V., "Vibrational Relaxation in Oxygen and Nitrogen," Journal of Fluid Mechanics, Vol. 1, No. 61, 1961.

Blottner, F. G., Johnson, M., and Ellis, M., "Chemically Reacting Viscous Flow Program for Multicomponent Gas Mixtures," Sandia Lab., Report No. SC-RR-70-754, Albuquerque, NM, December 1971.

Borger, W. U., "Disruptive Technology: Hypersonic Propulsion," Briefing Slides, AFRL HQ, Release No. 07-0083, September 2007.

Cauchon, D. L., "Radiative Heating Results from the FIRE II Flight Experiment at a Reentry Velocity of 11.4 Kilometers per Second," NASA TM X-1402, National Air and Space Administration, April 1972.

Chambers, L.H. (Hartung), "Predicting Radiative Heat Transfer in Thermochemical Nonequilibrium Flow Fields," NASA TM-4564, September 1994.

Chapman, S., "On the kinetic theory of gas. Part II. – A composite monatomic gas: Diffusion, viscosity, and thermal conduction," Phil. Trans. Royal So. London, 217A, 115, 1916.

Cheatwood, F.M, and Gnoffo, P.A., "User's Manual for the Langley Aerothermodynamic Upwind Relaxation Algorithm (LAURA)," NASA TM 4674, April 1996.

Chernyi, G. G., Losev, S. A., Macheret, S. O., and Potapkin, B. V, Physical and Chemical Processes in Gas Dynamics: Cross Sections and Rate Constants, Volume I, Progress in Aeronautics and Astronautics, Vol. 196, Reston, VA, 2002.

Chernyi, G. G., Losev, S. A., Macheret, S. O., and Potapkin, B. V., Physical and Chemical Processes in Gas Dynamics: Physical and Chemical Kinetics and Thermodynamics of Gases and Plasmas, Volume II, Progress in Aeronautics and Astronautics, Vol. 197, Reston, VA, 2004.

Cooley, J. W., Mathematical Computation, Vol. XV, 1961, pp. 363 ff..

Cornette, E. S., "Forebody Temperatures and Calorimeter Heating Rates Measured During Project FIRE II Reentry at 11.35 Kilometers per Second," NASA TM X-1305, National Air and Space Administration, 1966.

Cussler, E. L., Multicomponent Diffusion, Elsevier, New York, 1976.

Doroshenko, V., "Effect of the Formation of Vibrationally Excited Nitrogen Molecules in Atomic Recombination in a Boundary Layer on the Heat Transfer," High Temperature (USSR), Vol. 28, No. 1, 1990, pp. 82-89.

Enskog, D., Kinetische Theorie der Vorgange in massing verdumten Gasen, Ph.D. Thesis, University of Uppsala, Sweden 1917.

Evans, M. W., and Harlow, F. H., "The Particle-in-Cell Method for Hydrodynamic Calculations," Los Alamos Scientific Laboratory, Report No. LA-2139, Los Alamos, NM, 1957.

Fay, J., and Riddell, F. , "Theory of Stagnation Point Heat-Transfer Studies with a Blunt Body in a Shock Tube," Heat Transfer-Soviet Research, Vol. 1, No. 2, 1969, pp. 8-14.

Feldick, A. M., Modest, M., and Levin, D. A., "Closely Coupled Flowfield-Radiation Interactions For Flowfields Created During Hypersonic Reentry," 2008-4104, 40th AIAA Thermophysics Conference, June 2008.

Fuchs, R. P., *et al.*, "Why an Wither of Hypersonics Research in the US Air Force," USAF, Scientific Advisory Board, December 2000.

Fujita, K. and Abe, T., "SPRADIAN, Structured Package for Radiation Analysis: Theory and Application," Japan Aerospace Exploration Agency, Report No. 669, Sep 1997.

Fujita, K. and Abe, T., SPRADIAN, Structured Package for Radiation Analysis: Theory and Application," Report 669, The Institute of Space and Astronautical Science, September, 1997.

Gambosi, T. I., Gaskinetic Theory, Cambridge Atmospheric and Space Sciences Series, Cambridge University Press, 1994.

Gilmore, F. R., Laber, R. R., and Epsy, P. J., "Frank-Condon Factors, r-Centroids, Electronic Transition Moments, and Einstein Coefficients for Many Nitrogen and Oxygen Band Systems," Journal of Physical Chemistry Reference Data, Vol. 21, No. 5, 1992, pp. 1005-1107.

Gnoffo, P., Hartung L.C., and Greendyke, R. B., "Heating Analysis for a Lunar Transfer Vehicle at Near-Equilibrium Flow Conditions," AIAA-93-0270, 31st Aerospace Sciences Meeting and Exhibit, Reno, NV, January 1993.

Gnoffo, P. A., Roop N. G., and Shinn, J. L., "Conservation Equations and Physical Models for Hypersonic Air Flows in Thermal and Chemical Nonequilibrium," NASA TP 2867, February 1989.

Gnoffo, P.A., "An Upwind-Biased, Point Implicit Relaxation Algorithm for Viscous, Compressible Gas Flows," NASA TP 2953, February 1990.

Grad, H., On the kinetic theory of rarefied gases, Comm. Pure Appl. Math., Vol. 2, No. 331, 1949.

Greendyke, R.B. and Hartung, L.C., "A Convective and Radiative Heat Transfer Analysis for the FIRE II Forebody," Journal of Spacecraft and Rockets, Vol. 31, No. 6, November-December, 1994, pp.986-992.

Greendyke, R.B. and Hartung, L.C., "An Approximate Method for the Calculation of Nonequilibrium Radiative Heat Transfer," Journal of Spacecraft and Rockets, Vol. 28, No. 2, March, 1991, pp. 165-171.

Greendyke, R.B., Associate Professor, Air Force Institute of Technology, Wright-Patterson AFB, OH. Personal Interview. 16 August 2011.

Griem, H., Plasma Spectroscopy, McGraw-Hill, 1964.

Gupta, R., Yos, J., and Lee, K. P., —A Review of Reaction Rates and Thermodynamics Properties for an 11-Species Air Model for Chemical and Thermal Nonequilibrium Calculations up to 30,000 K, NASA TR-1232, August 1987.

Hallion, R. P., —The History of Hypersonics: or, —Back to the Future—Again and Again," AIAA-2005-329, 43rd Aerospace Sciences Meeting and Exhibit, January, 2005.

Hartung, L.C., Nonequilibrium Radiative Heating Prediction Method for Aeroassist Flowfields with Coupling to Flowfield Solvers, PhD Dissertation, North Carolina State University, 1991.

Heppenheimer, T. A., —Facing the Heat Barrier: a History of Hypersonics," NASA SP-2007-4232, September 2007.

Herzberg, G., Molecular Spectra and Molecular Structure, Volume 1, -Spectra of Diatomic Molecules, Van Nostrand Reinhold Company Inc., 1950.

Hirsch, C. H., —Convection Algorithms Based on a Diagonalized Procedure for the Multidimensional Euler Equations," AIAA-1987-1163, 8th Computational Fluid Dynamics Conference, Honolulu, HI, June, 1987.

Hirschel, E. H., Basics of Aerothermodynamics, Progress in Aeronautics and Astronautics, Vol. 204, AIAA, 2005.

Holt, E., and Haskell, R., Foundations of Plasma Dynamics, Macmillan, New York, 1965, pp. 151-182.

Jaffe, R. L., —The Calculation of High-Temperature Equilibrium and Nonequilibrium Specific Heat Data for N2, O2, and NO," AIAA 87-1633, 22nd Thermophysics Conference, Honolulu, Hawaii, June, 1987.

Johnston, C. O., —Nonequilibrium Shock-Layer Radiative Heating for Earth and Titan Entry," Ph.D. Dissertation, Virginia Polytechnic Institute and State University, 2006.

Johnston, C. O., Hollis, B. R., and Sutton, K., —Nonequilibrium Stagnation-Line Radiative Heating for Fire II," Journal of Spacecraft and Rockets, vol. 45, no. 6, November-December, 2008, pp. 1185 -1195.

Johnston, C. O., Gnoffo, P. A., and Sutton, K., "The Influence of Ablation on Radiative Heating for Earth Entry," 2008-4107, 40th AIAA Thermophysics Conference, June, 2008.

Josyula, E., and Shang, J. S., "Computation of Nonequilibrium Hypersonic Flowfields Around Hemisphere Cylinders," Journal of Thermophysics and Heat Transfer, AIAA, Vol. 7, No. 4, October-December, 1993, pp. 668-679.

Josyula, E., "Computational Study of Vibrationally Relaxing Gas Past Blunt Body in Hypersonic Flows," Journal of Thermophysics and Heat Transfer, Vol. 14, No. 1, 2000, pp. 18-26.

Josyula, E., and Bailey, W. F., "Governing Equations for Weekly Ionized Plasma Flowfields of Aerospace Vehicles," Journal of Spacecraft and Rockets, Vol. 40, No. 6, 2003, pp. 845-857.

Klein, O., Zeitschrift für Physik, Vol. 76, 1932, pp. 226 ff..

Kolobov, V., *et al.*, "Unified Flow Solver for Aerospace Application," AIAA 2006-988, 44th AIAA Aerospace Sciences Meeting and Exhibit, Reno, NV, Jan 2006.

Komives, J. and Greendyke, R. B., "Development of Coupled Flowfield - Radiation Solution Methods in Ablative Environments," AIAA-1031, 47th AIAA Aerospace Sciences Meeting including The New Horizons Forum and Aerospace Exposition, Orlando, FL, Jan , 2009.

Komives, J., "Development of Non-Uniform Radiation Solution Methods for Atmospheric Re-Entry Using Detailed Thermal Modeling," Masters Thesis, Air Force Institute of Technology, 2009.

Landau, L. D., and Lifshitz, E. M., "The Classical Theory of Fields," Gosterkhizdat, Moscow, 3rd edition, 1960. English transl. (revised 2nd edition), Addison-Wesley, Reading, MA, 1962.

Lee, J., "Electron-Impact Vibrational Excitation Rates in the Flowfield of Aeroassisted Orbital Transfer Vehicles," Thermophysical Aspects of Re-Entry Flows, Vol. 103, Progress in Aeronautics and Astronautics, AIAA, New York, 1986, pp. 197-224.

Lewis, J. H, Scallion, W. I., "Flight Parameters and Vehicle Performance for Project FIRE Flight II, Launched May 22, 1965," NASA TN D-3569, National Air and Space Administration, 1966.

Magin, T. E., Panesi, M., Bourdon, A., and Bultel, A., "Analysis of the FIRE II flight experiment by means of a collisional radiative model," Center for Turbulence Research Annual Research Briefs, Aeronautics and Aerospace Department, von

Karman Institute for Fluid Dynamics, Belgium, pp. 159-171, 2008.

Martin, C., Greendyke, R. B., –Comparative Analysis of Two-Temperature vs. Multi-Species, Multi-Temperature Modeling in Nonequilibrium Radiating Shock Layers," AIAA-235, 47th AIAA Aerospace Sciences Meeting, Orlando, FL, January, 2010.

McCall, G. H., *et al.*, –New World Vistas: Air and Space Power for the 21st Century," USAF, Scientific Advisory Board, December, 1995.

McLucas, *et al.*, –Hypersonic Technology for Military Applications," USAF, Studies Board, 1989.

Milikan, R., and White, D., –Systematics of Vibrational Relaxation," Journal of Chemical Physics, Vol. 39, No. 12, 1963, pp. 3209-3213.

Modest, M. F., –Radiative Heat Transfer," 2nd Edition, Academic Press, San Diego, CA, 2003.

Nicolet, W.E., –Advanced Methods for Calculating Radiation Transport in Ablation-Product Contaminated Boundary Layers," NASA CR 1656, Sept. 1970.

Nicolet, W.E., –User's Manual for the Generalized Radiation Transfer Code (RAD/EQUIL)," NASA CR 116353, October, 1969.

Norris, G., –U.S. Hypersonics Could Hinge on X-51 Tests," Aviation Week, 19 March, 2010.

Olivero, J. J., and Longbothum, R. L., –Empirical Fits to the Voigt Line Width: A Brief Review," Journal of Quantitative Spectroscopy and Radiative Transfer, Vol. 17, 1977, pp. 233-236.

Olstad, W.B., –Nongray Radiating Flow about Smooth Symmetric Bodies," AIAA Journal, Vol. 9, No. 1, January, 1971.

OSD, Budget Item Justification (R2 Exhibit), R-1 Budget, Line Item No. 103, 2008.

Pai, S. I., Radiation Gas Dynamics, Springer-Verlag, New York, 1966.

Park, C., –Nonequilibrium Air Radiation (NEQAIR) Program: User's Manual," NASA TM-86707, July, 1985.

Park, C., –Assessment of Two-Temperature Kinetic Model for Ionizing Air," AIAA Paper 87-1574, June, 1987.

Park, C., Nonequilibrium Hypersonic Aerothermodynamics, John Wiley & Sons, New York, 1992.

Peach, G., –Continuous Absorption Coefficients for Non-Hydrogenic Atoms," Memoirs of the Royal Astronomical Society, Vol. 73, Part 1, 1970, pp.1-123.

Penner, S. S., and Olfe, D. B., Radiation and Reentry, Academic Press, New York, 1968.

Rees, A. L. G., Proceedings of the Physical Society, A, Vol. 59, 1947, pp. 998 ff..

Richter, J., Plasma Diagnostics, Lochte-Holtgreven, W., North-Holland Publishing Co., Amsterdam, 1968, pp. 1-65.

Roe, P. L., –Characteristic Based Schemes for the Euler Equations," Annual Review of Fluid Mechanics, Vol. 18., 1986, pp. 337-365.

Roe, P. L., Approximate Riemann solvers, parameter vectors and difference schemes. J. Computational Physics. Vol. 43, 1981. pp. 537-78.

Rydberg, R., Zeitschrift für Physik, Vol. 73, 1931, pp. 376 ff..

Schadee, A., –The Formation of Molecular Lines in the Solar Spectrum," Bulletin of the Astronomical Institute of Netherlands, Vol. 17, No. 5, 1964, pp. 311-357.

Slinker, S., and Ali, A. W., "Electron Excitation and Ionization Rate Coefficient for N2 02, NO, N, and O," NRL Memorandum Report 47560, Naval Research Laboratory, 1982.

Stupochenko, Ye. V., Losev, S. A., and Osipov, A. I., –Relaxation in Shock Waves," Springer-Verlag, New York, 1967.

Sutton, K., –Characteristics of Coupled Nongray Radiating Gas Flows with Ablation Products Effects About Blunt Bodies During Planetary Entries," Ph.D. Dissertation, North Carolina State University, 1973.

Tichkoff, *et al.*, –Review and Evaluation of the Air Force Hypersonic Technology Program," USAF, Studies Board, 1998.

Traving, G., –Interpretation of Line Broadening and Line Shift," in Plasma Diagnostics, Lochte-Holtgreven, W., North-Holland Publishing Co., Amsterdam, 1968, pp. 66-134.

Van Leer, B., –Towards the Ultimate Conservation Difference Scheme V, a Second-Order Sequel to Godunov's Method," Journal of Computational Physics, Vol. 32, No. 1, 1979, pp. 101-136.

Vincenti, W. and Kruger Jr., C., Introduction to Physical Gas Dynamics, John Wiley & Sons, 1967.

Walters, R.W., Cinnella, P., Slack, D., and Halt, D., "Characteristics-Based Algorithms for Flows in Thermo-Chemical Nonequilibrium," AIAA-09-0393, 28th Aerospace Sciences Meeting, Reno, NV, January 1990.

Whiting, E.E., Arnold, J.O., and Lyle, G.C., "A Computer Program for the Line-By-Line Calculation of Spectra from diatomic Molecules and Atoms Using a Voigt-Line Profile," NASA TN D-5088, March, 1969.

Yee, H. C., "Upwind and Symmetric Shock-Capturing Schemes," NASA TM-89464, May, 1987.

Zel'dovich, Y. B. and Raizer, Yu. P., Physics of Shock Waves and High-Temperature Hydrodynamic Phenomena, Dover Publications, Mineola, NY, 1967.

REPORT DOCUMENTATION PAGE		Form Approved OMB No. 074-0188

1. REPORT DATE *(DD-MM-YYYY)*	2. REPORT TYPE	3. DATES COVERED *(From – To)*
15-12-2011	Dissertation	Aug 2008 –Dec 2011

TITLE AND SUBTITLE

Coupled Radiation-Gasdynamic Solution Method for Hypersonic Shock Layers in Thermochemical Nonequilibrium

5a. CONTRACT NUMBER N/A

5b. GRANT NUMBER N/A

5c. PROGRAM ELEMENT NUMBER N/A

6. AUTHOR(S)

Martin, Christopher, L., Jr., Captain, USAF

5d. PROJECT NUMBER N/A

5e. TASK NUMBER N/A

5f. WORK UNIT NUMBER N/A

7. PERFORMING ORGANIZATION NAMES(S) AND ADDRESS(S)
Air Force Institute of Technology
Graduate School of Engineering and Management (AFIT/ENY)
2950 Hobson Way, Building 640
WPAFB OH 45433-8865

8. PERFORMING ORGANIZATION REPORT NUMBER

AFIT/DS/ENY/11-16

9. SPONSORING/MONITORING AGENCY NAME(S) AND ADDRESS(ES)
Air Force Office of Scientific Research
875 N. Randolph Street Suite 325, Room 3112
Arlington, Virginia 22203
Dr. John D. Schmisseur
(703) 696-6962; John.Schmisseur@afosr.af.mil

10. SPONSOR/MONITOR'S AFOSR

11. SPONSOR/MONITOR'S REPORT NUMBER(S) N/A

12. DISTRIBUTION/AVAILABILITY STATEMENT
APPROVED FOR PUBLIC RELEASE; DISTRIBUTION UNLIMITED.

13. SUPPLEMENTARY NOTES None

14. ABSTRACT

The purpose of this research was to develop a highly accurate computational method for calculating the nonequilibrium radiative heat transfer within reentry shock layers. The nonequilibrium state of the flowfield was solved using the multispecies multitemperature nonequilibrium flow solver NH7AIR which is capable of separately tracking the vibrational energy of each diatomic species and the energy of the free electrons. The calculation of radiative heat transfer was performed by utilizing the detailed line-by-line spectral radiation solver SPRADIAN. Two radiative transport schemes were implemented in this coupled code. The first scheme was the standard tangent slab solution method. The second scheme was a finite volume method scheme for radiative heat transfer (FVMR). Data from the FIRE II flight experiment were used to validate the computer code. Coupled results obtained utilizing the tangent slab method exhibited a high degree of agreement with these experimental data. The utility of the FVMR scheme was also examined in an uncoupled implementation. Together, the enhancement of the nonequilibrium thermal modeling, the use of a highly accurate spectral radiation solver and the development of a conservative scheme for radiative transport constitute a significant improvement in current capabilities available for modeling the radiating shock layers which accompany reentry flight conditions.

15. SUBJECT TERMS

Hypersonics, Reentry, Radiative Transport, Nonequilibrium Aerodynamics

16. SECURITY CLASSIFICATION OF:			17. LIMITATION OF ABSTRACT	18. NUMBER OF PAGES	19a. NAME OF RESPONSIBLE PERSON
a. REPORT	b. ABSTRACT	c. THIS PAGE			Robert B. Greendyke, CIV, ADVISOR
U	U	U	UU	174	19b. TELEPHONE NUMBER *(Include area code)* (937) 255-6565, ext. 4567 (Robert.Greendyke@afit.edu)

Standard Form 298 (Rev. 8-98)
Prescribed by ANSI Std. Z39-18